Nonlinear and Ultrafast Optical Investigations of Correlated Materials

Thesis by
Hao Chu

In Partial Fulfillment of the Requirements for the
degree of
Doctor of Philosophy in Applied Physics

California Institute of Technology
Pasadena, California

2017
Defended May 11th 2017

Acknowledgements

Looking back at the journey I have taken during graduate school, there are many people whom I would like to thank for having shaped, inspired or accompanied me. First and foremost I would like to thank my advisor David Hsieh, a man of immense vision and ideas. Never stopping, David pushes the realm of our scientific inquiry to newer and newer frontiers. For this, and for all other guidance I have received from him, I owe him deep gratitude. I would also like to thank colleague Darius Torchinsky and Wes Erbsen, Daisy Raymondson, Mike Walls from KMLabs for teaching me ultrafast optics from scratch. Without their guidance, many of the experiments we did would be difficult if not impossible to start. Alberto de la Torre taught me generously on the scientific part. His knowledge of theory and experiment on correlated materials is impressive. I have never failed to deepen my understanding of correlated physics every time I discuss with him. I have also learnt a lot about 2D materials from Alon Ron, another colleague of mine. I would also like to thank colleagues Tejas Deshpande, Liuyan Zhao, John Harter, Junyi Shan, Honglie Ning, with whom I interacted everyday and collaborated on a few different projects. From all these people I learnt a great deal about condensed matter physics, and more broadly how to be a scientist.

On this subject of growing to be a scientist, I am also grateful to Prof. Brent Fultz, Prof. Sandra Troian and Prof. Nai-Chang Yeh for bringing me to Caltech and introducing me to the world of condensed matter physics. Frank Rice, for whom I was the teaching assistant for quite a few terms, showed me a great example of an experimental physicist and the kind of teacher I would like to be.

I would also like to thank the many precious friends I made at Caltech, who shared my passions and always supported me. I want to thank Ding Ding and Bilin Zhuang, whom I came to know in my first year and with whom I shared many late nights working on problem sets and discussing science and life. Many of my thanksgiving eves were spent with them and to me they are like my family. I would also like to thank Chan U Lei, who was my apartment-mate for a long time and who shared the same passions and encouraged me in times of frustration. Yiyang Liu, Daodi Lu, Lei Fu are the people with whom I had many intellectual discussions and learnt a lot about interesting things outside physics: history, politics, etc. I would also like to thank Yejun Feng and Yishu Wang from Rosenbaum's group for teaching me X-ray scattering and sharing scientific ideas with me. Much more than these people,

I would also like to thank Wei-Hsun Lin, Yingrui Chang, Xilin Lv, Junle Jiang, Xuan Zhang, Sijia Dong, Fan Liu, Jingbo Huang, Xiaoying Tan, Menghua Zhuang, and many others whom I cannot name all at once here. They made up the colorful spectrum of my life through graduate school and I always relish the memories I had with them. I would also like to thank my undergraduate friend Leizhi Sun, a physicist too, who is always in touch to share his latest aspirations. And also to my friends and teachers from Jin Ling Middle School, I owe them deep thanks for nurturing a free and independent soul in me and preparing me for all the adventures I would embark on in my life. These are the friendships, no matter how distant in time and space, I will always carry in my heart.

To those who brought me onto the journey of physics, I owe them deep thanks and appreciations. These include Fritjof Capra with his *the Tao of Physics*, which opened the mind-boggling door of physics to me. My high school friend Leiyu Xie inspired me to take interest in arts and humanities and offered great help to me when I was applying for college. My undergraduate advisor Lyman Page is a physicist whose devotion to research and students has deeply moved me and inspired me to become a physicist and a teacher like him from day one. I have also been tremendously inspired, at different stages of my life, by undergraduate friend Jingyuan Zhang and primary school classmate Mingming Yang, who are physicists themselves too, to pursue my passion to the fullest and to the best of my capability.

Last but not least, I would also like to thank Mengran Yang, who encouraged me and lightened me up when I was frustrated. Thanks to her, I am upbeat and always ready for new challenges in research and in life. To my parents, Jin Chu and Qian Gu, who cultivated a scientific curiosity and gift in me since my childhood, I owe them my deepest gratitude. I thank them for giving me a carefree environment to explore and pursue anything that interests me. I still remember that one evening during my 5th grade in elementary school, my dad mentioned that Nanjing University, a leading research university in my hometown, developed state-of-art laboratories for condensed matter physics research. Those magical words of condensed matter physics had since taken root in me and led me to where I am this day. For these and for the unyielding love and support they have given to me, I thank my parents with all my heart.

Abstract

This thesis comprises studies of 3d-5d transition metal oxides with various degrees of electronic correlation using nonlinear harmonic generation rotational anisotropy as well as time-resolved optical reflectivity methods. Specifically, we explored photo-induced phase transition in Ca_2RuO_4 and Sr_2IrO_4, discovered novel electronic phases in doped Sr_2IrO_4 and $Sr_3Ir_2O_7$, and investigated different types of antiferromagnetic orders in transition metal trichalcogenides MPX_3.

Ca_2RuO_4 is an antiferromagnetic insulator in which the delicate balance between microscopic competing interactions can be tipped over by a gentle external influence. In particular, heating Ca_2RuO_4 above 350 K induces a first-oder insulator-to-metal transition together with a structural phase transition. Using time-resolved pump probe optical reflectivity, we explored the possibility of photo-induced insulator-to-metal transition in Ca_2RuO_4. While transient optical reflectivity shows a metal-like response above a critical pump fluence, a metallic signature is absent in the transient terahertz reflectivity. Our results suggest a finite spectral weight being transferred to the Mott gap, although a metastable photo-induced metallic phase is absent. This is consistent with the lack of photo-induced structural phase transition which would otherwise stabilize the metallic phase.

The layered perovskite iridate $Sr_{n+1}Ir_nO_{3n+1}$ is iso-structural to the cuprate high temperature superconductors and realize an interesting analogue to the cuprate family. Electron-doped Sr_2IrO_4 has recently been shown to exhibit the pseudogap phase as well as possibly d-wave superconductivity. We first used time-resolved optical reflectivity to investigate the temperature evolution of the electronic structure in electron- and hole-doped Sr_2IrO_4. Then, using second harmonic generation rotational anisotropy, we refined the crystallographic structure of Sr_2IrO_4 and identified an inversion breaking hidden order phase in both the parent and hole-doped Sr_2IrO_4 at low temperatures. We find that the loop-current model, which was proposed to explain the pseudogap phase of cuprates, well explains this microscopic hidden order in Sr_2IrO_4.

The bilayer $Sr_3Ir_2O_7$ is a weak spin-orbit coupled antiferromagnetic insulator. Contrary to its single layer cousin, no interesting electronic phases have been reported in electron or hole-doped $Sr_3Ir_2O_7$. Using time-resolved optical reflectivity, we found evidence for a closing of the insulating gap in $Sr_3Ir_2O_7$ above T_N. In addition, in

electron-doped metallic $Sr_3Ir_2O_7$, we discovered a charge-density-wave-like instability that onsets at a previously reported structural phase transition temperature. However, this electronic instability is of a peculiar nature in that it might be short-ranged or fluctuating in time, which is similar to the fluctuating charge density wave recently observed in underdoped cuprate.

Transition metal trichalcogenides MPX_3, where M = {Mn, Fe, Ni}, X = {S, Se}, are layered van der Waals materials that undergo magnetic transitions at low temperatures. Different types of magnetic order, including the Néel order and the antiferromagnetic stripe order, realize depending on the ratios between J_1, J_2 and J_3. We demonstrate that second harmonic generation (SHG) is sensitive to the microscopic magnetic structures. In particular, the SHG process couples to Néel order parameter in $MnPS_3$ but not the antiferromagnetic stripe order parameter in $FePS_3$. Our experiment proves that SHG can be used as a sensitive and non-invasive tools for identifying the different magnetic structures in 2D materials.

Published Content

1. Chu, H. *et al.* A charge density wave-like instability in a doped spin orbit assisted weak Mott insulator. *Nature Materials* **16,** 200–203 (2017). DOI: 10.1038/nmat4836
   Contribution: Designed and conducted experiment. Analyzed data. Wrote paper.

2. Zhao, L., Torchinsky, D. H., Chu, H., *et al.* Evidence of an odd-parity hidden order in a spin- orbit coupled correlated iridate. *Nature Physics* **12,** 32 (2016). DOI: 10.1038/nphys3517

   Contribution: Conducted experiment.

3. Torchinsky, D. H., Chu, H., *et al.* Structural Distortion-Induced Magnetoelastic Locking in Sr_2IrO_4 Revealed through Nonlinear Optical Harmonic Generation. *Phys. Rev. Lett.* **114,** 096404 (2015). DOI: 10.1103/PhysRevLett.114.096404
   Contribution: Designed and conducted experiment. Analyzed data.

4. Torchinsky, D. H., Chu, H., *et al.* A low temperature nonlinear optical rotational anisotropy spectrometer for the determination of crystallographic and electronic symmetries. *Rev. Sci. Instrum.* **85,** 083102 (2014). DOI: 10.1063/1.4891417
   Contribution: Conducted experiment. Analyzed data.

Table of Contents

Acknowledgements . . . iii
Abstract . . . v
Table of Contents . . . vii
Chapter I: Introduction to correlated materials . . . 1
1.1 Hubbard model . . . 1
1.2 Crystal field . . . 3
1.3 Spin-orbit interaction . . . 5
1.4 Phases of cuprate high-T_c supercondutors . . . 6
Chapter II: Experimental techniques . . . 11
2.1 Second harmonic generation rotational anisotropy . . . 11
2.2 Time-resolved optical reflectivity . . . 13
Chapter III: Adsorbate effect in optical pump probe experiments . . . 16
3.1 Introduction . . . 16
3.2 Time-dependent reflectivity from adsorbate-affected Sr_2IrO_4 . . . 16
Chapter IV: Optical pump probe investigation of electronic and structural instabilities in Ca_2RuO_4 . . . 20
4.1 Introduction . . . 20
4.2 Experiment and results . . . 20
Chapter V: Optical pump probe investigations of the electronic structures of electron- and hole-doped Sr_2IrO_4 . . . 29
5.1 Introduction . . . 29
5.2 Experimental . . . 29
5.3 Results . . . 30
Chapter VI: Hidden order phase in Sr_2IrO_4 revealed by second harmonic generation rotational anisotropy . . . 37
6.1 Introduction . . . 37
6.2 Experiment and results . . . 38
Chapter VII: Charge-density-wave-like instability in $(Sr_{1-x}La_x)_3Ir_2O_7$ revealed by time-resolved optical reflectivity . . . 48
7.1 Introduction . . . 48
7.2 Experiment and results . . . 48
Chapter VIII: Second harmonic generation investigations of antiferromagnetic orders in MPX_3 . . . 56
8.1 Introduction . . . 56
8.2 Experiment and results . . . 58
Bibliography . . . 63

Chapter 1

Introduction to correlated materials

The band theory of solids laid down the theoretical foundation for quantitative investigations of the electronic properties of solids. It was highly successful in understanding the transport properties of elemental metals and semiconductors, with verdict that a crystal with an odd number of electrons per unit cell is a metal. However, the discovery of a few insulating transition metal oxides posed serious challenge to the band theory. CoO, MnO and NiO all have an odd number of electrons per unit cell but they turned out to be electrically insulating. Nevill Mott realized that it is the strong Coulomb interaction between the electrons that is responsible for the insulating nature of these transition metal oxides. Charge correlation splits the otherwise half-filled conduction band into a fully filled valence band and an empty conduction band with a gap in between. The importance of these so-called Mott insulators was not realized until the discovery of high temperature superconductors half a century later. The high temperature superconductors are doped Mott insulators and exhibit a plethora of interesing electronic phases. Since then, it was realized from extensive researches on high temperature superconductivity that in addition to charge, the lattice, spin and orbital degrees of freedom could all play important roles in interaction and lead to the rich phase diagrams of correlated materials.

1.1 Hubbard model

Hubbard introduced a model Hamiltonian to account for the competition between kinetic hopping (t) and Coulomb correlation (U), which favors banding and localization respectively:

$$H = \sum_{\langle ij\rangle\sigma} -t_{ij} c^{\dagger}_{i\sigma} c_{j\sigma} + U \sum_{i} n_{i\uparrow} n_{i\downarrow} \tag{1.1}$$

where $n_{i\sigma} = c^{\dagger}_{i\sigma} c_{i\sigma}$ is the number operator, $c^{\dagger}_{i\sigma}$ and $c_{i\sigma}$ are the creation and annihilation operators for an electron with spin σ at site i. $t's$ are intra- and inter-site (nearest neighbour) hopping energies: t_{ii} describes the mean energy of the band while t_{ij} describes the bandwidth.

In the $U = 0$ limit, $c^{\dagger}_{i\sigma}$ and $c_{i\sigma}$ can be expanded in terms of the creation and annihi-

lation operators of the Bloch states:

$$c_{i\sigma}^{\dagger} = \frac{1}{\sqrt{N}} \sum_{\mathbf{k}} \mathrm{e}^{i\mathbf{k}\cdot\mathbf{R}_i} c_{\mathbf{k}\sigma}^{\dagger}, \quad c_{i\sigma} = \frac{1}{\sqrt{N}} \sum_{\mathbf{k}} \mathrm{e}^{-i\mathbf{k}\cdot\mathbf{R}_i} c_{\mathbf{k}\sigma}. \tag{1.2}$$

The first term in (1.1) becomes

$$\sum_{\mathbf{k}\sigma} E_{\mathbf{k}\sigma} c_{\mathbf{k}\sigma}^{\dagger} c_{\mathbf{k}\sigma}, \quad E_{\mathbf{k}\sigma} = \sum_{\langle ij \rangle} t_{ij} \mathrm{e}^{i\mathbf{k}\cdot(\mathbf{R}_i - \mathbf{R}_j)} \tag{1.3}$$

Since t_{ij} has the same periodicity as the lattice, we see that the eigenstates of the non-interacting Hamiltonian become the free traveling Bloch states. On the other hand if $t_{ij} = 0$, the Hamiltonian becomes diagonal and

$$E = \sum_{\mathbf{1}} t_{ii}(n_{i\uparrow} + n_{i\downarrow}) + U n_{i\uparrow} n_{i\downarrow} \tag{1.4}$$

At half filling, E is minimized if there is exactly one electron on each site i, i.e. $n_{i\uparrow} n_{i\downarrow} = 0$. The kinetic energy gain t_{ij} for hopping is 0 while the penalty U for double occupancy as a result of hopping is heavy, hence electrons are localized to their sites and an insulating ground state results. We see that the two limits of the Hubbard model correspond to a band metal and a Mott insulator.

For half filling and the limit of large U, it can be shown that the effective Hamiltonian for (1.1) becomes the antiferromagnetic Heisenberg model:

$$H = -J \sum_{\langle ij \rangle} \mathbf{S}_i \cdot \mathbf{S}_j \tag{1.5}$$

where $J = -4t_{ij}^2/U$. This can be understood from the virtual exchange process envisioned below. If the electronic spins on neighbouring sites are parallel, hopping is forbidden by the Pauli principle. However, if they are antiparallel, then one electron can hop onto its neighbouring site, creating double occupancy and hence an energy cost U. The electron can then hop back to its original site, removing the energy cost U. This process is dubbed virtual hopping or virtual exchange and acts as a perturbation to the antiferromagnetic ground state. By second order perturbation theory, the energy of the perturbed state is lowered from the original state by an amount proportional to $-t_{ij}^2/U$. This explains why Mott insulators are usually antiferromagnetic. According to this effective Hamiltonian, the low energy excitations of this half-filled large-U Hubbard model are spin excitations, corresponding to the configuration where neighbouring spins are flipped during the virtual exchange process.

Although antiferromagnetic order is usually associated with Mott insulators, it is not *a priori*. In fact, one needs to distinguish between a Mott insulator and a Slater insulator. In the latter, antiferromagnetic order doubles the size of the unit cell and opens up a gap at the folded Brillouin zone boundary in the momentum space. In a Mott insulator, the fundamental reason for opening up a gap at the Fermi energy is electron correlation. Whether $T_N = T_{IMT}$ defines a practical way for distinguishing between a Mott insulator and a Slater insulator. In Chapter 7, we will discuss this issue again for the $5d$ spin-orbit assisted Mott insulator $Sr_3Ir_2O_7$.

1.2 Crystal field

In addition to Coulomb repulsion, lattice, or crystal field, also has important effects on the electronic ground state of correlated materials. A free atom in a spherical potential has orbital eigenstates described by spherical harmonics:

$$\psi_{nlm}(\mathbf{r}) = R_{nl}(r)Y_l^m(\theta,\phi) \tag{1.6}$$

The orbital angular momentum of such a state is given by the azimuthal quantum number l, with projection m along the z-axis. For a partially filled shell, Hund's rule states that the lowest energy configuration is the state with (1) maximum total spin angular momentum ($S = |m_s| = |\sum s_i|$), (2) maximum total orbital angular momentum ($L = |m_l| = |\sum m_i|$), (3) minimum J for less than half-filled shell ($J = L - S$) and maximum J for more than half-filled shell ($J = L + S$). Both spin angular momentum and orbital angular momentum of the electrons contribute to the magnetic moment of the ion, which is then given by

$$\mu = g\sqrt{J(J+1)}\mu_B \tag{1.7}$$

where g is the Landé g-factor defined as

$$g = 1 + \frac{J(J+1) + S(S+1) - L(L+1)}{2J(J+1)} \tag{1.8}$$

For transition metals with d electrons on the outmost shell, the orbital angular momentum component is often found missing from the measured magnetic moment. This happens because in a crystalline environment, the ionic potential is no longer spherical, instead it is reduced to discrete rotational symmetries in addition to other symmetries. In a q-fold rotational symmetric crystalline environment, the ionic potential can be expanded in terms of the spherical harmonics and the only non-vanishing terms are Y_l^m with m as an integer multiple of q. As a result, this potential

only couples orbital momentum states with quantum numbers m_1 and m_2 such that $m_1 - m_2 = Nq$ where N is an integer. In an octahedral environment, Y_2^{+2} and Y_2^{-2} are coupled together to give rise to the new d_{xy} and $d_{x^2-y^2}$ eigenstates:

$$d_{xy} = \frac{1}{\sqrt{2}\mathrm{i}}\left(Y_2^{+2} - Y_2^{-2}\right)$$

$$d_{x^2-y^2} = \frac{1}{\sqrt{2}}\left(Y_2^{+2} + Y_2^{-2}\right)$$

A similar transformation gives the d_{xz}, d_{yz}, d_{z^2} states:

$$d_{xz} = \frac{1}{\sqrt{2}}\left(Y_2^{-1} - Y_2^{+1}\right)$$

$$d_{yz} = \frac{\mathrm{i}}{\sqrt{2}}\left(Y_2^{-1} + Y_2^{+1}\right)$$

$$d_{z^2} = Y_2^0$$

Since Y_2^{+m} and Y_2^{-m} contribute equally to these states, $L_z = \sum m_i = 0$, i.e. these new eigenstates do not possess orbital angular momentum. Moreover, they split the degeneracy of the spherical harmonic states of the spherical potential. In an octahedral environment, the energy of $\{d_{xy}, d_{xz}, d_{yz}\}$ is lowered while the energy of $\{d_{x^2-y^2}, d_{z^2}\}$ is raised. They are designated as the t_{2g} and e_g states respectively and their energy difference is often referred to as 10Dq or simply crystal field splitting.

It is instructive to look at the expectation value of L_z in the basis of $|\psi_i\rangle = \{d_{xz}, d_{yz}, d_{xy}, d_{x^2-y^2}, d_{z^2}\}$,

$$\left\langle \psi_i \middle| L_z \middle| \psi_j \right\rangle = \left(\begin{array}{ccc|cc} 0 & i & 0 & 0 & 0 \\ -i & 0 & 0 & 0 & 0 \\ 0 & 0 & 0 & 2i & 0 \\ \hline 0 & 0 & -2i & 0 & 0 \\ 0 & 0 & 0 & 0 & 0 \end{array}\right) \tag{1.9}$$

This means that while an eigenstate of a crystal field by itself does not possess orbital angular momentum, transition among different eigenstates may generate an orbital angular momentum. Even so, the orbital angular momentum among the e_g states is completely quenched (bottom right 2×2 matrix). Transition among the t_{2g} states, on the other hand, can generate a finite orbital angular momentum, which is isomorphic to that of the p-orbitals up to a minus sign:

$$\left\langle \psi_i \middle| L_z \middle| \psi_j \right\rangle = \begin{pmatrix} 0 & -i & 0 \\ i & 0 & 0 \\ 0 & 0 & 0 \end{pmatrix}, \quad \text{with} \quad |\psi_i\rangle = \{p_x, p_y, p_z\} \tag{1.10}$$

Transition between the t_{2g} and e_g states is thwarted by their energy difference. Similar arguments can be given to the other components of the orbital angular momentum operator $\mathbf{L}$. Therefore, under crystal field splitting, the orbital angular momentum becomes $L = 1$ for the t_{2g} states and vanishes for the e_g states.

1.3 Spin-orbit interaction

While crystal field quenches orbital angular momentum, spin-orbit interaction, on the other hand, prefers a different linear combination of the spherical harmonics and 'unquenches' the orbital angular momentum. In $3d$ transition metal spin-orbit effect is weak, but in $5d$ transition metal spin-orbit interaction may have energy comparable to Coulomb interaction and crystal field splitting. In such systems, the crystal field orbital states are no longer the eigenstates of the spin-orbit coupled Hamiltonian. Instead, we need to consider the eigenstates of the total angular momentum operator $\mathbf{J} = \mathbf{L} + \mathbf{S}$.

For $L = 1$ and $S = 1/2$, i.e. t_{2g} states, the J_{eff} states can be found as linear combinations of the crystal field orbital states using the Clebsch-Gordan table:

$$|J_{\text{eff}}, m_{J_{\text{eff}}}\rangle = \sum_{m_l, m_s} \alpha_{m_l m_s} |l, m_l\rangle |s, m_s\rangle$$

which gives

$$\left|\frac{3}{2}, \pm\frac{3}{2}\right\rangle = |1, \pm 1\rangle \left|\frac{1}{2}, \pm\frac{1}{2}\right\rangle$$

$$\left|\frac{3}{2}, \pm\frac{1}{2}\right\rangle = \sqrt{\frac{1}{3}} |1, \pm 1\rangle \left|\frac{1}{2}, \mp\frac{1}{2}\right\rangle + \sqrt{\frac{2}{3}} |1, 0\rangle \left|\frac{1}{2}, \pm\frac{1}{2}\right\rangle$$

$$\left|\frac{1}{2}, \pm\frac{1}{2}\right\rangle = \pm\sqrt{\frac{2}{3}} |1, \pm 1\rangle \left|\frac{1}{2}, \mp\frac{1}{2}\right\rangle \mp \sqrt{\frac{1}{3}} |1, 0\rangle \left|\frac{1}{2}, \pm\frac{1}{2}\right\rangle$$

where on the right hand side $|1, \pm 1\rangle = (\mp d_{xz} - i d_{yz})/\sqrt{2}$ and $|1, 0\rangle = d_{xy}$. Plugging them in, we find

$$\begin{pmatrix} |1/2, 1/2\rangle \\ |3/2, 1/2\rangle \\ |3/2, -3/2\rangle \end{pmatrix} = \begin{pmatrix} -1/\sqrt{3} & 1/\sqrt{3} & -i/\sqrt{3} \\ -2/\sqrt{6} & -1/\sqrt{6} & i/\sqrt{6} \\ 0 & 1/\sqrt{2} & i/\sqrt{2} \end{pmatrix} \begin{pmatrix} d_{xy\uparrow} \\ d_{yz\downarrow} \\ d_{xz\downarrow} \end{pmatrix} \tag{1.11}$$

etc. These J_{eff} states are the eigenstates of the spin-orbit coupled Hamiltonian. They describe the $5d$ electron states in $Sr_{n+1}Ir_nO_{3n+1}$ as we will see in Chapter 5 through Chapter 7.

1.4 Phases of cuprate high-T_c superconductors

As discussed in previous sections, correlated materials exhibit lattice, charge, spin, and orbital degrees of freedom. Under appropriate experimental conditions, they exhibit macroscopic orders known as phases. Furthermore, these microscopic degrees of freedom often compete with one another and result in a kaleidoscope of phases in close proximity of one another. In such cases, small changes in temperature, pressure, electromagnetic field, or carrier doping, can tip the balance between the competing interactions and drive the system from one phase to another. A good example of this is Ca_2RuO_4, in which either a moderate amount of heat ($\sim$ 360 K), or pressure ($\sim$ 0.5 GPa), or electric field ($\sim$ 40 V/cm) is enough to drive the system from an insulator into a metal. In Chapter 4, we exploit such instability and investigate the possibility of inducing an insulator-to-metal transition in Ca_2RuO_4 using light. On the other hand, the multitude of macroscopic phases that can be realized in correlated materials is best exemplified by the cuprate high-T_c superconductor, which exhibits the Mott insulating phase, high temperature superconductivity (HTSC), pseudogap, charge-density-wave (CDW), nematic order at different temperature and doping levels [Fig. 1.1]. Apart from the unsolved mystery of HTSC, the pseudogap and the charge-density-wave phase have attracted a lot of attention recently regarding their roles in the formation of HTSC. Below we introduce the basic phenomenology of these two phases based on studies on cuprate high-T_c superconductors. In Chapter 6, using second harmonic generation rotational anisotropy we show that Sr_2IrO_4 also manifests a hiddren phase consistent with theoretical models of the pseudogap phase. In Chapter 7, we provide evidence for a charge-density-wave-like instability in electron-doped $Sr_3Ir_2O_7$ using time-resolved optical reflectivity.

Superconductivity is characterized by the formation of an energy gap at the Fermi level below which Cooper pairs form. The Cooper pairs form a superfluid that flows with zero electrical resistance. Breaking of the Cooper pairs by thermal excitation or phonon scattering is thwarted by the presence of the energy gap. As with an ordinary electronic wavefunction, the superconducting wavefunction is composed of the orbital part and the spin part. The orbital wavefunction takes angular momentum values of $L = 0$, 1, 2, etc, and inherits the same symmetries prescribed for the corresponding atomic wavefunctions. The spin component takes on corresponding values $S = 0$, 1, such that the total wavefunction is antisymmetric under the exchange of two electrons. Conventional superconductors are characterized by $L = 0$ and $S = 0$, which gives rise to a uniform superconducting gap in the Brillouin

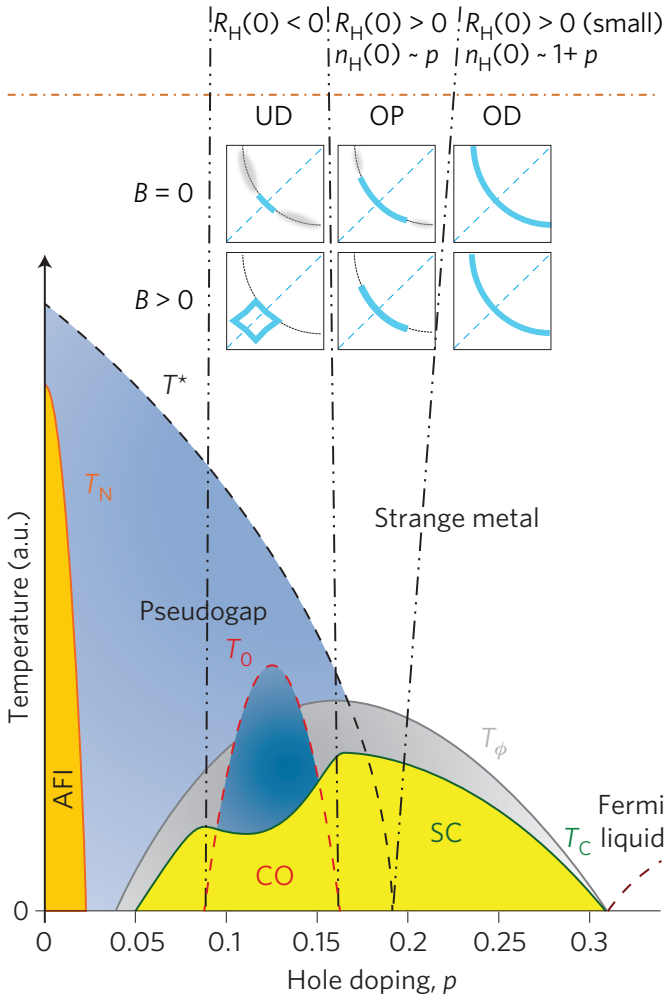

Figure 1.1: **Phase diagram of $La_{2-x}Sr_xCuO_4$ [1].** The pseudogap temperature T^* extrapolates to 0 at near p $\sim$ 0.2 doped holes per CuO_2 plaquette. In the underdoped regime, a short-ranged charge order (CO) onsets below T_0 and competes with superconductivity, causing a dip in T_c. T_ϕ denotes the temperature below which superconducting phase fluctuations are observed.

zone. High-T_c superconductors, in most cases, are characterized by $L = 2$ and $S = 0$, and are called d-wave superconductors. A d-wave superconducting gap exhibits nodes along the (π, π) and equivalent directions in the Brillouin zone, where the phase $\phi(\mathbf{k})$ of superconducting gap function $\Delta(\mathbf{k})e^{i\phi(\mathbf{k})}$ switches sign [Fig. 1.2]. However, even at temperatures above T_c and below a characteristic T^* (pseudogap tempreature), part of the Fermi surface is already gapped with a finite density of states residing along the 'Fermi arcs' around the position of the nodes. As temperature cools towards T_c, these Fermi arcs shrink towards the position of the nodes,

the process of which is depicted in Fig. 1.2. Such Fermiology is unique to HTSC and the phase between T_c and T^* is termed the pseudogap phase. One interpretation of the microscopic origin of the pseudogap phase is that Cooper pairs form in the pseudogap phase without phase coherence. This is based on the observation of Bogoliubov quasiparticle interference, a signature of delocalized Cooper pairs, at energy $< T^*$ in the pseudogap phase. However, excitation at energy $\sim T^*$ in the pseudogap phase breaks local C4 symmetry of the underlying cuprate lattice and is distinct from the homogeneous low energy excitations. Understanding the holistic picture of the pseudogap phase is still underway and is crucial for understanding the mechanism of HTSC.

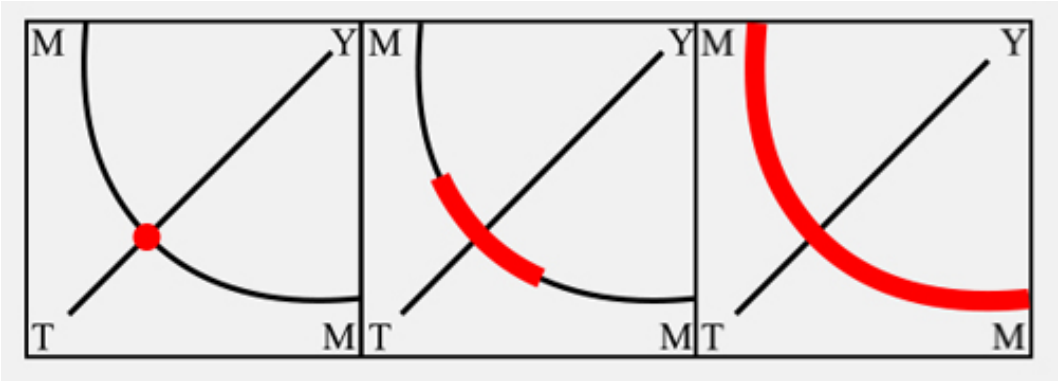

Figure 1.2: **Illustration of the temperature evolution of Fermi surface in underdoped cuprate.** From left to right: (one quadrant of) Fermi surface of an underdoped cuprate at $T < T_c$, $T_c < T < T^*$ and $T > T^*$. The pseudogap phase ($T_c < T < T^*$) is characterized by the Fermi arcs extending from the position of the *d*-wave gap nodes with other parts of the Fermi surface gapped out.

Another prominent feature of the cuprate phase diagram is the charge order in underdoped samples [Fig. 1.1], which is also referred to as the charge density wave. Neutron diffraction provided the first evidence of charge order in hole-doped cuprates. In underdoped $La_{1.6-x}Nd_{0.4}Sr_xCuO_4$, the static charge order manifests as a set of satellite peaks around Bragg peaks at wave vectors $\mathbf{Q}_{charge}$ = (H $\pm$ q_{charge}, K $\pm$ q_{charge}, L) [Fig. 1.3(b)(c)]. In addition, neutron diffraction also found modulation of the antiferromagnetic order at twice the wavelength of the charge modulation. It manifests as a set of magnetic peaks around the AF wave vector (1/2, 1/2, L) at $\mathbf{Q}_{AF}$ = (1/2 $\pm$ q_{AF}, 1/2 $\pm$ q_{AF}, L) with $q_{AF} = 1/2 \cdot q_{charge}$ [Fig. 1.3(b)-(d)]. For x = 0.125, q_{charge} and q_{AF} are determined to be 0.25 and 0.125 respectively. Therefore, the real space charge and spin order can be visualized as Fig. 1.3(a), where the doped holes arrange themselves into one dimensional 'charge rivers' separating two

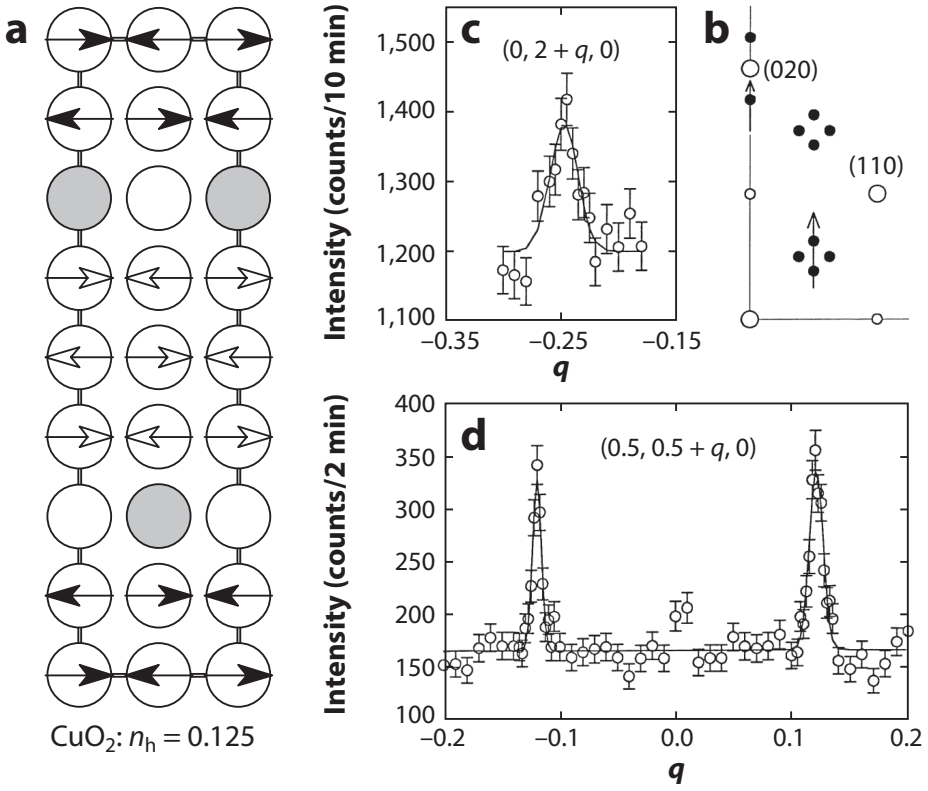

Figure 1.3: **Charge order in $La_{1.6-x}Nd_{0.4}Sr_xCuO_4$ revealed by neutron diffraction [2].** a. Schematic of the charge and spin order in 12.5% hole-doped LNSCO. Circle denote Cu sites in the CuO_2 plane. Arrows denote Cu spins, with black and white colors denoting anti-phase relation. Gray circles denote the location of doped holes. b. (HK0) projection of the reciprocal space showing the location of charge and magnetic peaks (black) and Bragg peaks (white). c. Charge order at (0, 1.75, 0) revealed by elastic neutron scattering. d. Magnetic order at (0.5, 0.375, 0) and (0.5, 0.625, 0).

opposite antiferromagnetic domains. Direct visualizations of the charge order are provided by scanning tunneling microscopy (STM). In Bi2212, STM reveals periodic modulations in tunneling conductance inside vortices where superconductivity is suppressed by externally applied magnetic field [Fig 1.4]. This argues for the competition scenario between HSTC and charge density wave. Additional evidence for this interpretation comes from the temperature-doping phase diagram, where T_c is suppressed or even fully eliminated (in the case of LBCO) by the presence of charge density wave [Fig. 1.1]. In addition to the static charge order observed by diffraction and STM, charge density wave may also exist dynamically. This has been demonstrated in ref [3] where signatures of the amplitude and phase modes

of a fluctuating charge density wave in underdoped LSCO are captured by time-resolved optical techniques. Understanding the mechanism that gives rise to the prevalent charge order phenomenon in high-T_c superconductors is also important for understanding HTSC and is being intensely pursued.

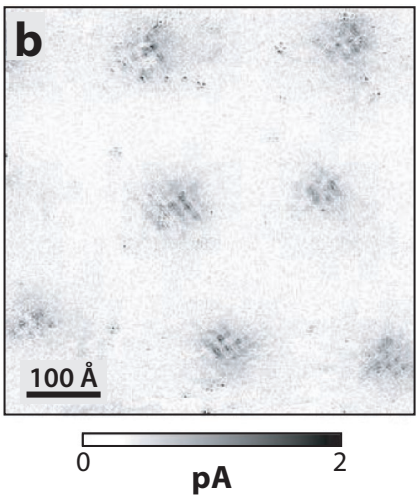

Figure 1.4: **Periodic modulation of tunneling conductance in the vortices of superconducting $Bi_2Sr_2CaCu_2O_{8+\delta}$ [2].** The vortices are formed with an externally applied magnetic field. Inside the vortices where superconductivity is suppressed, the tunneling conductance shows modulation with a periodicity of 4 lattice sites.

Chapter 2

Experimental techniques

The development of ultrafast femtosecond laser over the past decades made possible nonlinear optics as well as time-resolved measurements of electronic and structural dynamics of solids. We developed and employed second harmonic generation rotational anisotropy as well as time-resolved optical reflectivity techniques for investigating correlated materials.

The experiments described below are enabled by a KMLabs Wyvern 1000 ultrafast amplified laser system. This system outputs 1 mJ pulses at 10 kHz repetition rate. We use leakage beams through dielectric mirrors, which have less than 1 μJ pulse energy, for our experiments. These pulses typically have a temporal width of 70 fs and a wavelength around 795 nm ($\sim$ 1.5 eV) with a FWHM of 50 nm.

2.1 Second harmonic generation rotational anisotropy

Electromagnetic waves travelling through a medium induces an oscillating electric dipole **P**, magnetic dipole **M**, and electric quadrupole $\hat{\mathrm{Q}}$ in the medium at frequencies ω_i of the incident waves as well as linear combinations of these frequencies: **P**(ω_1+ω_2+...), etc. Mathematically, this is expressed as the expansion of multipole moments in terms of the electric and magnetic fields of the incident light [4]:

$$\mathbf{P} \propto \chi^{ee} : \mathbf{E} + \chi^{em} : \mathbf{H} + \chi^{eee} : \mathbf{EE} + \chi^{eem} : \mathbf{EH} + \chi^{emm} : \mathbf{HH} + O(\mathbf{E},\mathbf{H})^3$$

$$\mathbf{M} \propto \chi^{me} : \mathbf{E} + \chi^{mm} : \mathbf{H} + \chi^{mee} : \mathbf{EE} + \chi^{mem} : \mathbf{EH} + \chi^{mmm} : \mathbf{HH} + O(\mathbf{E},\mathbf{H})^3$$

$$\hat{\mathrm{Q}} \propto \chi^{qe} : \mathbf{E} + \chi^{qm} : \mathbf{H} + \chi^{qee} : \mathbf{EE} + \chi^{qem} : \mathbf{EH} + \chi^{qmm} : \mathbf{HH} + O(\mathbf{E},\mathbf{H})^3$$

They radiate according to

$$\mathbf{S} = \mu_0 \frac{\partial^2 \mathbf{P}}{\partial t^2} + \mu_0 \Big(\nabla \times \frac{\partial \mathbf{M}}{\partial t} \Big) - \mu_0 \Big(\nabla \frac{\partial^2 \hat{\mathrm{Q}}}{\partial t^2} \Big),$$

where the electric dipole contribution ($\propto$ **P**) is usually the strongest contribution. In the case of a monochromatic incident light, as is the case for a narrow-band laser, the radiated field consists of harmonics at ω, 2ω, 3ω, etc. Second harmonic generation refers to the $O(\mathbf{E},\mathbf{H})^2$ processes such as $\mathbf{P}(2\omega) = \chi^{eee}\mathbf{E}(\omega)\mathbf{E}(\omega)$, $\mathbf{M}(2\omega) = \chi^{mee}\mathbf{E}(\omega)\mathbf{E}(\omega)$ or $\hat{\mathrm{Q}}(2\omega) = \chi^{qee}\mathbf{E}(\omega)\mathbf{E}(\omega)$. Since the process involves two copies

of the incident light field, the intensity of SHG scales as the square of the intensity of the input light. It is particularly enhanced by ultrafast pulsed laser with large peak electric field.

The specific form (i.e. non-zero independent elements) of the multipole tensor χ is constrained by the symmetry of the media as well as the nature of the tensor itself. For example, if C is a symmetry operation of a crystal, then the second order electric susceptibility tensor χ^{eee} for the crystal has to obey $\chi^{eee}_{ijk} = \chi^{eee}_{i'j'k'} \equiv C_{i'i}C_{j'j}C_{k'k}\chi^{eee}_{ijk}$. Additionally, if χ is an axial tensor, then the right hand side of the equation has to be multiplied by the determinant of the symmetry operation; under time reversal operation, a polar tensor is invariant while an axial tensor changes sign. Applying these rules to a centrosymmetric medium, we find that χ^{eee} vanishes but χ^{mee} and χ^{qee} are allowed. If a phase transition breaks inversion, then χ^{eee} becomes allowed. Therefore, SHG can be used as a sensitive probe for inversion breaking, and more generally symmetry breaking, during phase transitions. In such experiments, symmetry breaking would either manifest as a discontinuous increase in SHG intensity, or a reduction in discrete symmetry. In fact, second harmonic generation rotational anisotropy (SHG-RA) has been demonstrated in NiO [5], Bi-YIG/GGG [6] with normally incident beam, and in GaFeO3 [7] with obliquely incident beam where the polarizations of the beams are rotated while the scattering plane remains fixed. The limitation of a normally incident experiment is that tensor elements involving the z component are not probed. On the other hand, in the latter oblique incident experiment where the scattering plane remains fixed, the SHG signal at each angle is a different linear combination of tensor elements. Extracting individual tensor elements from such data could be challenging. Therefore, it is desirable to conduct SHG-RA experiment with oblique incidence on a rotating sample. The challenge is that it is difficult to rotate a sample inside an optical cryostat and keep the incident beam from walking on the sample.

This difficulty is overcome by an ingenious design where the sample is fixed and the rotation of the scattering plane is accomplished by the use of a rotating transmissive phase grating [8]. A drawing of the rotating phase grating scheme is shown in Fig. 2.1. A normally incident laser beam (red) is diffracted by the phase grating into two constructive first orders with opposite wavevectors in the xy plane (normal to the optical axis). The phase grating is placed at the focal point of a convex lens which brings the two diverging beams to parallel to each other. Both beams then get focused onto the sample by a reflective objective. We make sure that the sample

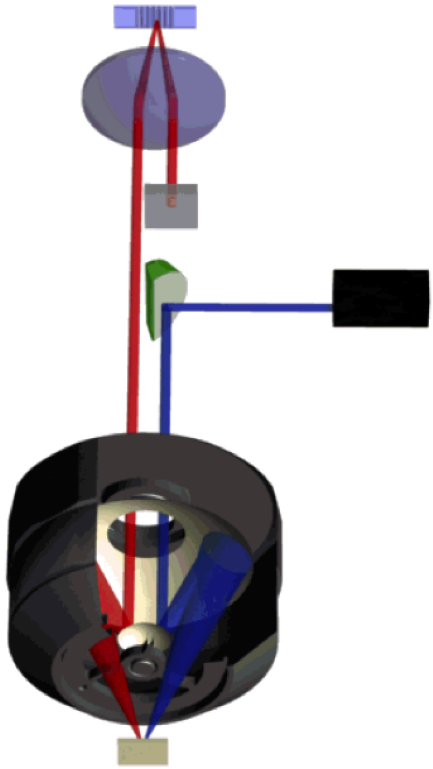

Figure 2.1: **Drawing of a rotating scattering plane defined by a rotating phase grating.**

is placed at the focal point of the reflective objective by checking that both beams are overlapped on the sample for all orientations of the phase grating. After this, we block one of the diffracted beam and reflect the other beam into a photomultiplier tube (PMT). A linear polarizer and a set of color filters are placed in front of the PMT to select the desired polarization and wavelength of the SHG. The phase grating, the PMT, as well as a 1/2-waveplate (not shown in Fig. 2.1) in front of the phase grating are rotated simultaneously to simulate the rotation of the lab frame. The layout of the entire SHG-RA experiment is shown in Fig. 2.2.

2.2 Time-resolved optical reflectivity

Another way ultrafast laser can be useful for material research is the time resolution it enables. After shining a pulse of light (pump) onto a sample and perturbing its ground state, we can monitor the subsequent change in the optical properties of the sample using another weak pulse of light (probe). A straightforward property to measure is the optical reflectivity, but other properties like optical transmissiv-

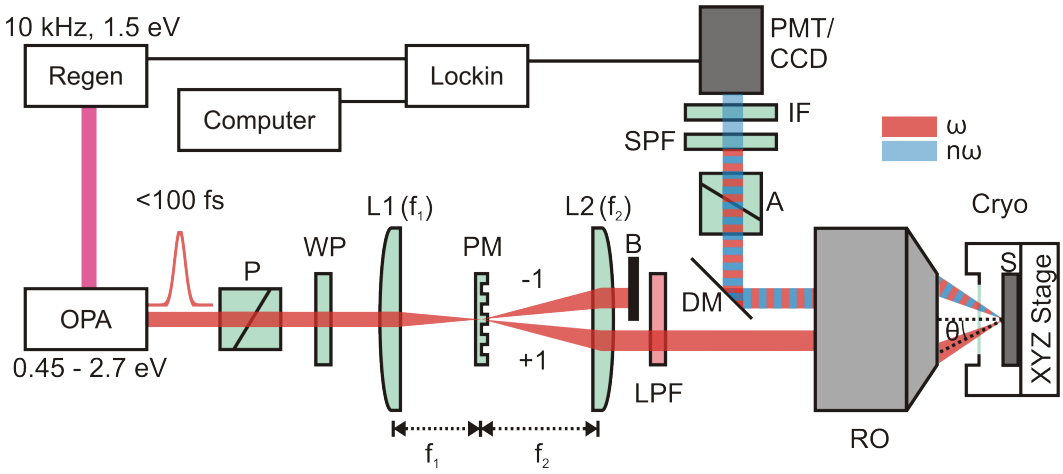

Figure 2.2: **Layout of the SHG-RA experiment. Regen**: regeneratively amplified ultrafast laser. **OPA**: optical parametric amplifier. **P**: polarizer. **WP**: waveplate. **L1(2)**: convex lens 1(2). **PM**: phase mask (phase grating). **LPF**: long pass filter. **DM**: dichroic mirror. **RO**: reflective objective. **Cryo**: cryostat. **A**: analyzer. **SPF**: short pass filter. **IF**: interference (band pass) filter. **PMT**: photomultiplier tube.

ity, terahertz reflectivity, Kerr-rotation angle, second harmonic generation rotational anisotropy, etc. can also be measured transiently. Figure 2.3 shows the layout of a time-resolved optical transmissivity experiment. Here, optical parametric amplifier (OPA) allows one to selectively generate light of different wavelength that can be used to pump and probe specific transitions in a material. The pump beam is usually mechanically chopped or optically modulated in time (not shown) so that the change in transient optical properties is also periodically modulated. This enables detection by lock-in amplifier. The delay between the pump and the probe is set by a mechanical delay stage. For transient optical reflectivity, we employ a balanced detection scheme which compensates for variations in laser pulse-to-pulse energy by subtracting a reference beam from the signal. Additionally, for degenerate pump probe reflectivity experiment, we set the pump and probe polarizations to perpendicular to each other so that pump scatter noise is minimized. By employing all these schemes, we are able to achieve a signal-to-noise ratio on the order of 10^{-5} for degenerate pump probe reflectivity experiments.

In addition to the ability to resolve electronic and structural dynamics on ultrafast timescales, pump probe experiment also realizes the possibility of driving ultrafast phase transition. To name a few examples: photo-induced insulator-to-metal transition has been demonstrated in VO_2 [9], photo-induced structural phase transition has been demonstrated also in VO_2 and $La_0.42Ca_0.58MnO_3$ [10]. More remark-

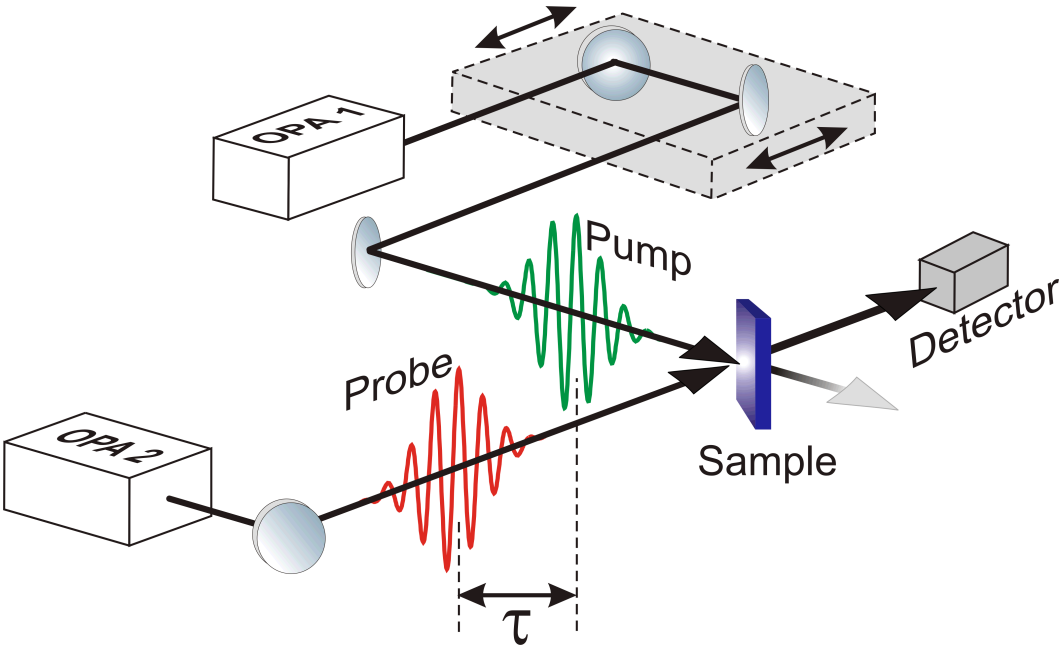

Figure 2.3: **Schematic of a pump probe reflectivity experiment.**

ably, evidences for photo-induced and photo-enhanced superconductivity have been reported in K_3C_{60} [11] and $YBa_2Cu_3O_{6.48}$ [12] respectively. These examples comprise only a small fraction of all the photo-induced phase transitions that have been demonstrated. In some of these experiments, optical excitation in the visible range is enough to induce phase transitions while in others, specific phonon modes need to be activated by mid-IR pulses before phase transitions can take place.

Chapter 3

Adsorbate effect in optical pump probe experiments

3.1 Introduction

Optical measurements are sensitive to the surface properties of the investigated samples. This is particularly true for measurements in cryogenic environment. In our optical pump probe reflectivity experiments on Rh-doped Sr_2IrO_4, we find that residual gases in the cryostat condenses onto the sample surface at low temperature and leads to oscillations in reflectivity. To ensure an adsorbate-free environment for these experiments, the use of a cover slip above the sample is necessary, in addition to a vacuum better than 5×10^{-7} mbar. Detailed descriptions of the phenomenology of surface adsorption in optical pump probe reflectivity studies are presented below.

3.2 Time-dependent reflectivity from adsorbate-affected Sr_2IrO_4

Single crystal $Sr_2Ir_{1-x}Rh_xO_4$ (x = 0.05 & x = 0.11) samples are cleaved in air and quickly transferred to an optical cryostat (Janis ST-500), which is pumped to a vacuum of $\sim 1 \times 10^{-6}$ mbar at room temperature by a turbo pump station (Pfeiffer HiCube). Liquid nitrogen is then used to cool the sample down. At 180 K, the vacuum inside the cryostat reaches 2×10^{-7} mbar. Under such vacuum condition, optical pump probe reflectivity data are taken during the cooling process with degenerate 800 nm beams. Figure 3.1 shows the reflectivity transients from the x = 0.11 sample as a function of temperature. At or above 180 K, the reflectivity transients show small changes as a function of temperature. Below 180 K, the reflectivity transient starts to change wildly: it first flips sign and reaches maximum negative magnitude at 140 K, then it decreases in magnitude while developing a positive component (120 K - 80 K). Such temperature dependence below 180 K is not reproducible upon additional measurements. Moreover, even at a fixed temperature below 180 K, the reflectivity transient evolves on a timescale of tens of minutes. Figure 3.2 shows the time dependence of the reflectivity transient from the same sample at 140 K. The change in the reflectivity transient on an hourly timescale is obvious, and the pump-induced reflectivity change at t = 0 oscillates between positive and negative on a timescale of $\sim$ 20 hrs. This is similar to the trend manifested in Fig. 3.1, where $\Delta R/R(t = 0)$ shows oscillating behavior in time too. Similar oscillation in reflectivity transients below 180 K is also observed on the x

= 0.05 sample in similar vacuum condition.

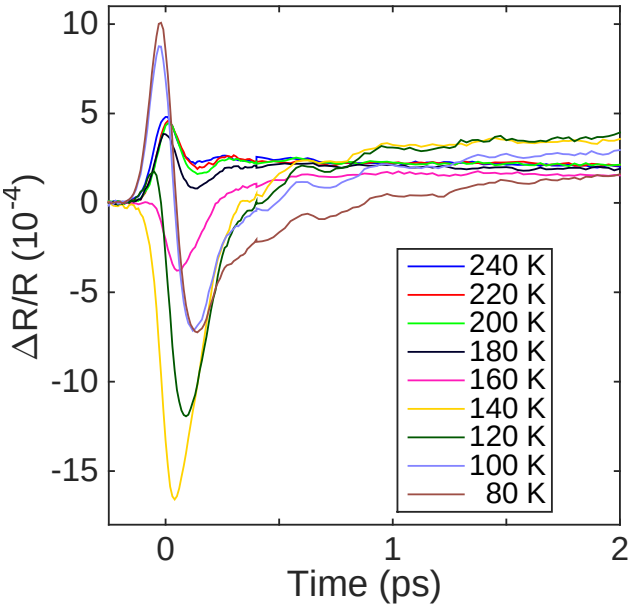

Figure 3.1: **Temperature dependent pump probe reflectivity transients from $Sr_2Ir_{1-x}Rh_xO_4$ (x = 0.11).** At or above 180 K, reflectivity transient shows small change as a function of temperature. Below 180 K, reflectivity transient shows non-monotonic change as a function of temperature. Moreover, the temperature dependent reflectivity transients below 180 K shown here are not reproducible upon additional measurements.

To gain further insight on the time dependence of the reflectivity transient below 180 K, we monitor the bare reflectivity of the x = 0.05 sample below 180 K as a function of time. Figure 3.3 shows the time dependence of reflectivity at 80 K and 140 K respectively. Reflectivity oscillates with a period of ~ 40 hr and ~ 20 hr respectively at the two temperatures. Moreover, the minimum of the pump probe transient at t = 0 also varies periodically with reflectivity, consistent with our observations in Fig. 3.1 and Fig. 3.2. Such periodicity disappears when temperature is increased to above 170 K. From these observations, we deduce that the oscillation in reflectivity is caused by interference of the reflected beams from the sample surface and the surface of gaseous molecules condensed onto the sample surface when temperature is below their freezing point. Because these gaseous molecules are continuously condensed onto the sample surface, the interference between the two reflections continuously evolves between constructive and destructive, leading to oscillations in reflected intensity. The period of oscillation at 80 K is understandably longer than that at 140 K because the gaseous molecules have less kinetic energy at lower

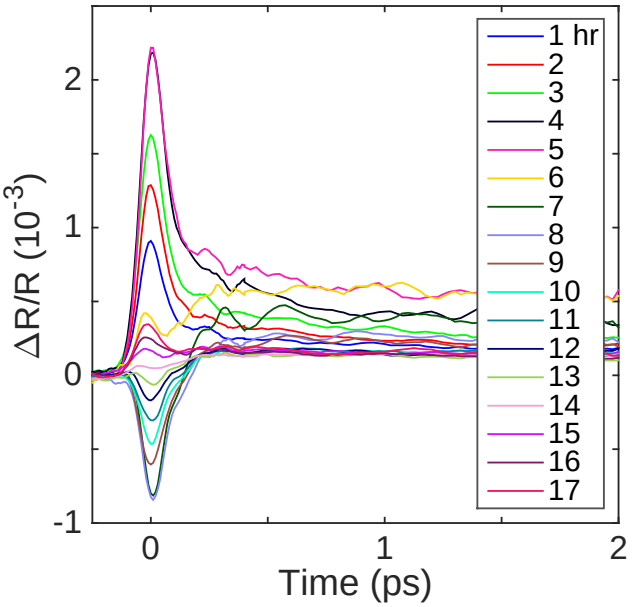

Figure 3.2: **Time dependent pump probe reflectivity transients from $Sr_2Ir_{1-x}Rh_xO_4$ (x = 0.11) at 140 K.** Reflectivity transients are taken at 1 hr intervals and show periodic variation between positive and negative pump-induced reflectivity change. The period of oscillation inferred from the data plotted here is about 20 hr.

temperature, thereby slowing down the adsorption process.

Since a vacuum of 2×10^{-7} mbar is approaching the operational limit of a turbo pump in combination with an optical cryostat, we search for ways for preventing the absorption process from happening other than improving vacuum condition. One solution is to employ a cover slip onto the sample holder rim above the sample using vacuum grease. At low temperatures, the cover slip acts as a cold surface to condense the gaseous molecules and prevents them from reaching the sample surface. After the installation of a cover slip, we found that the reflectivity of the sample measured on tens of hours timescale becomes stable and dominated by laser noise [Fig. 3.4]. Subsequent pump probe reflectivity measurements on other samples using a cover slip in combination with a vacuum of $\sim 10^{-7}$ mbar has always shown a stable reflectivity at cryogenic temperature. Therefore, the gaseous adsorption problem can be completely prevented by the cover slip method.

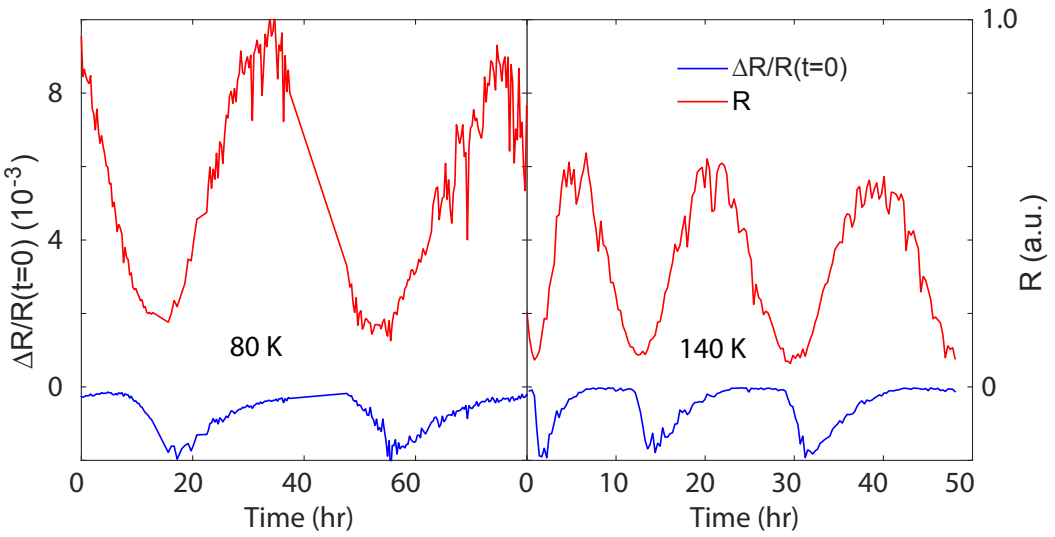

Figure 3.3: **Time dependence of reflectivity and ΔR/R(t = 0) on $Sr_2Ir_{1-x}Rh_xO_4$ (x = 0.05).** Reflectivity and the minimum of the reflectivity transient at t = 0 is shown as a function of time at 80 K and 140 K. Reflectivity oscillates with a period of 15 - 40 hr, while the reflectivity transient minimum also varies with the same periodicity. The oscillatory behavior is due to continuous condensation of gaseous molecules onto the sample surface over time.

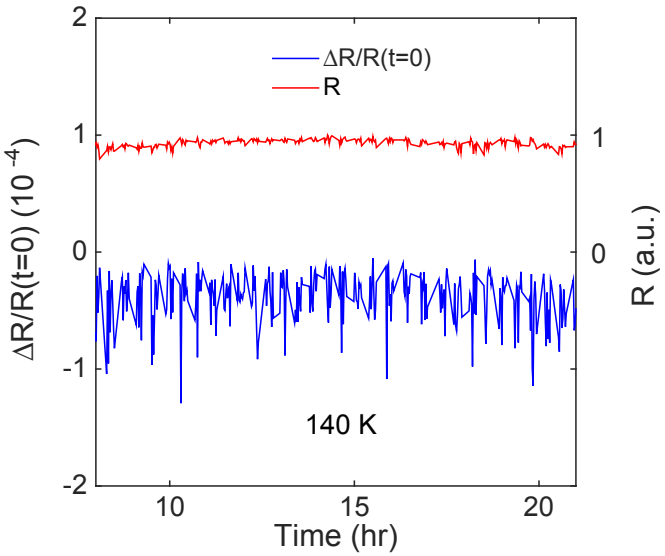

Figure 3.4: **Time dependence of reflectivity and ΔR/R(t = 0) on $Sr_2Ir_{1-x}Rh_xO_4$ (x = 0.11) with cover slip.** With a cover slip in thermal contact with the sample holder above the sample, oscillations in the sample reflectivity and the reflectivity transient both disappear.

Chapter 4

Optical pump probe investigation of electronic and structural instabilities in Ca_2RuO_4

4.1 Introduction

The layered perovskite Ca_2RuO_4 realizes an orbital-ordered antiferromagnetic insulator under ambient conditions [13–19]. This phase is stabilized by a delicate balance between competing microscopic interactions which makes it extremely fragile against external perturbations [20–24]. Heating Ca_2RuO_4 above 360 K induces a first-order insulator-to-metal transition (IMT) concomitant with a structural phase transition where the c-axis of the lattice is elongated [13, 25]. The insulator-to-metal transition can also be induced by isovalent substitution [13, 26] or carrier doping [26–29], a small electric field of $\sim$ 40 V/cm [30, 31], or a modest pressure of $\sim$ 0.5 GPa [32–34]. The multitude of IMT pathways in Ca_2RuO_4 testifies the delicate balance between the microscope degrees of freedom in it. Since photo-excitation is capable of inducing phase transitions in $3d$ transition metal oxides [9, 35–40], it would be interesting to explore how it affects the electronic instability in Ca_2RuO_4.

4.2 Experiment and results

Pristine Ca_2RuO_4 crystals are known to undergo irreversible structural damage when heated above T_{IMT} [29]. In our study, we use 8% Fe-doped Ca_2RuO_4 crystals that are structurally robust through thermal cycles across T_{IMT} [41]. The insulator-to-metal transition is well captured in optical reflectivity where an 8% drop is observed at 800 nm across $T_{IMT} = 369$ K, a temperature slightly higher than the undoped parent compound. This is consistent with our ellipsometry measurement shown in Fig. 4.1, where reflectivity at 800nm (1.55 eV) in the metallic phase is slightly lower than the insulating phase due to spectral weight transfer to low energies across the IMT. In our time-resolved optical reflectivity experiment, we focus cross-polarized 800 nm pump and probe light onto sample at near normal incidence. A sensitivity of 10^{-5} in $\Delta R/R$ is achieved by using a balanced detection scheme.

Figure 4.2 shows the transient response of $Ca_2Ru_{0.92}Fe_{0.08}O_4$ to optical excitation across T_{IMT}. In the metallic phase ($T > T_{IMT}$), impulsive optical excitation induces a sharp resolution-limited rise in reflectivity at time $t = 0$ followed by a fast decay

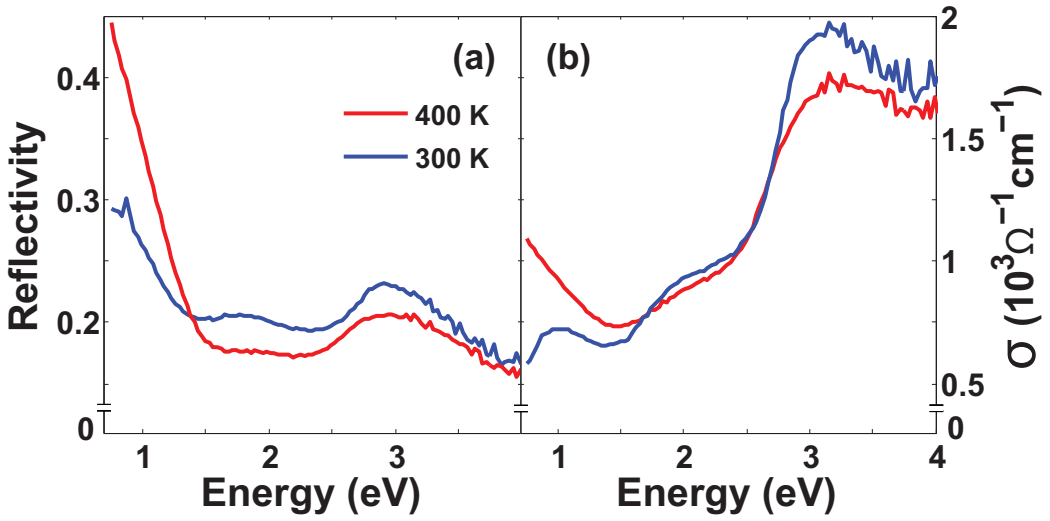

Figure 4.1: (a) Reflectivity and (b) the real part of optical conductivity of $Ca_2Ru_{0.92}Fe_{0.08}O_4$ in the insulating (T= 300 K) and metallic (T = 400 K) phase as a function of energy.

within the first 100 fs [Fig. 4.2(a)]. A more gradual equilibration process ensues, which is modulated by a coherent A_g optical phonon [42] on shorter time scales and a coherent acoustic phonon known as Brillouin scattering [43] on longer time scales [Fig. 4.2(a) inset]. As the sample is cooled into the Mott insulating phase, the sign of $\Delta R/R$ reverses [Fig. 4.2(b)]. The A_g optical phonon mode softens near T_{IMT} and undergoes an abrupt blue-shift as the lattice structure changes from L-Pbca to S-Pbca across T_{IMT}.

In order to better characterize the metallic phase under impulsive optical excitation, we perform fluence dependent pump probe studies on $Ca_2Ru_{0.92}Fe_{0.08}O_4$ above T_{IMT}. Figure 4.3(a) shows the reflectivity transients at a few different pump fluences at T = 385 K. Up to the highest fluence (40 mJ/cm^2) sampled, the pump induced reflectivity change at t = 0 increases linearly with pump fluence [Fig. 4.3(a) inset]. However, the relaxation dynamics of photo-excited carriers at short time scales (< 100 fs) changes in a nonlinear way with pump fluence, which is visualized by a comparison of the reflectivity transients normalized to their maxima for different pump fluences [Fig. 4.3(b)]. The carrier relaxation rate becomes slower as pump fluence increases. Optical pump probe reflectivity studies on gold and silver nano structures have established that carrier relaxation time in metals increases with fluence [44, 45]. This can be understood from the two temperature model describing the heat exchange between the electronic subsystem and the lattice subsystem,

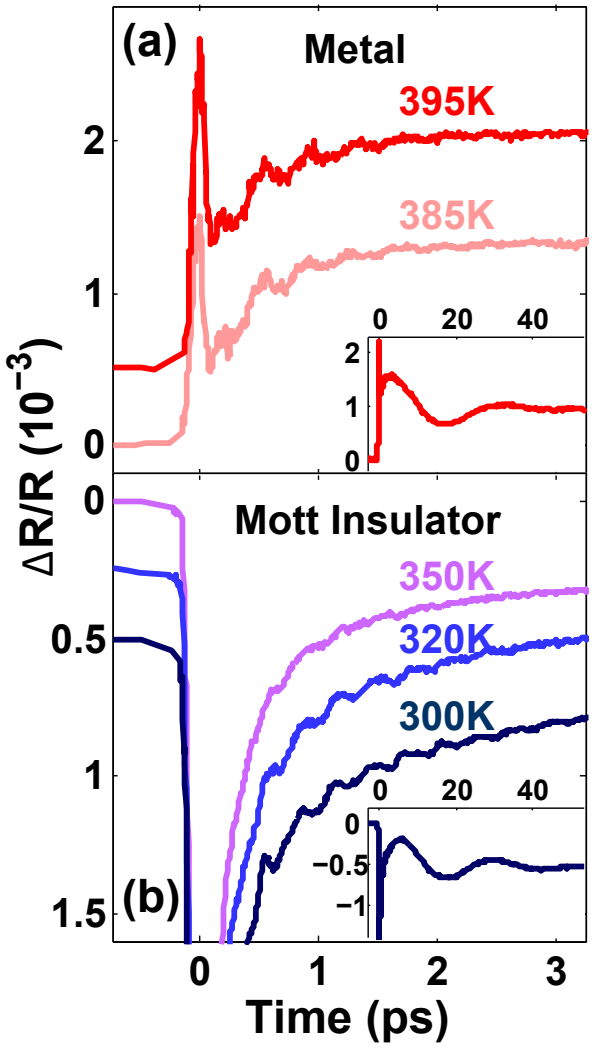

Figure 4.2: **Temperature dependent time-resolved optical reflectivity traces.** Data are taken **(a)** above and **(b)** below T_{IMT} with a pump fluence of 3.8 mJ/cm^2. Traces are vertically offset for clarity. Insets show traces on a longer timescale for T = 395 K and 300 K.

and the assumption that $\Delta R/R$ measures n, the photo-excited carrier density [46], through which the electronic temperature is defined after electron thermalization. The two temperature model is given by

$$C_e(T_e)dT_e/dt = -g(T_e - T_p),$$

$$C_p(T_p)dT_p/dt = g(T_e - T_p),$$

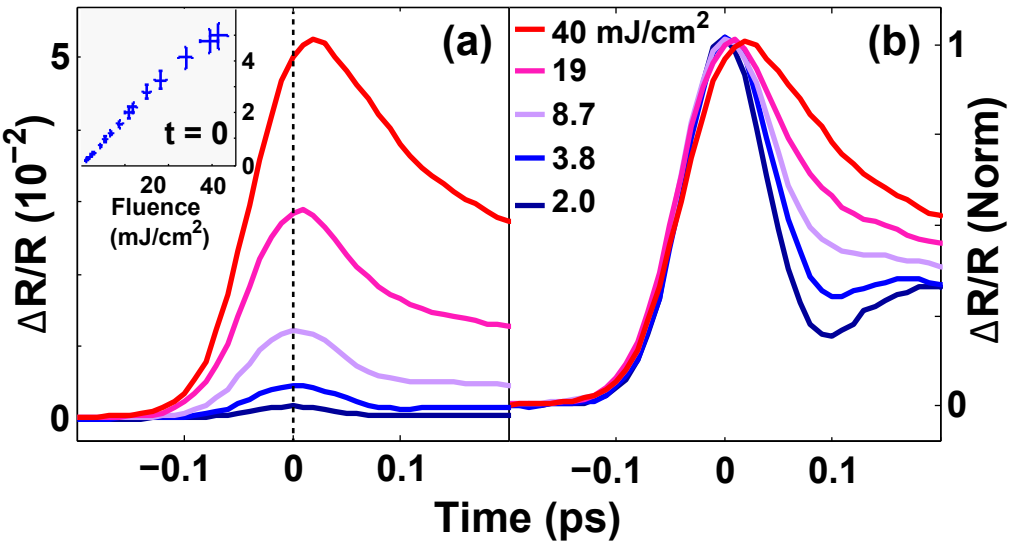

Figure 4.3: **Fluence dependence of transient reflectivity at T = 385 K (a)** Pump induced reflectivity change at t = 0. Inset shows the linear dependence of ΔR/R(t=0) on fluence. **(b)** The same set of reflectivity transients normalized to ΔR/R(t=0) to emphasize the change in relaxation dynamics at different pump fluences.

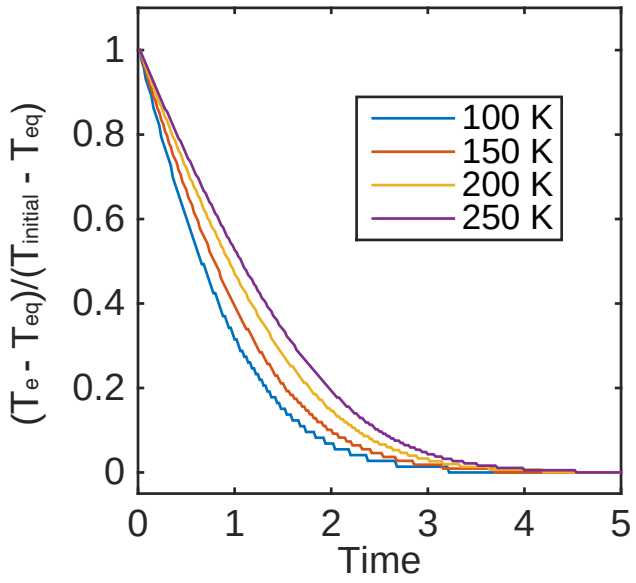

Figure 4.4: **Simulation of the variation of electronic temperature via heat exchange with lattice**. T_e: electronic temperature, $T_{initial}$: initial electronic temperature, T_{eq}: equilibrium temperature reached after the electron-lattice thermalization. Legend shows the different values of $T_{initial}$.

where g is the electron-phonon coupling constant, T_e and T_p (C_e and C_p) are the electron and lattice temperature (specific heat) respectively. For metals, $C_e(T_e) = \gamma T_e$, where $\gamma = \pi^2 k_B^2 g(\epsilon)/3$, k_B is the Boltzmann constant and $g(\epsilon)$ is the density of states at the Fermi energy. Figure 4.4 shows the time evolution of T_e computed from the two temperature model using realistic values of C_e and C_p for different pump fluences. Indeed, a slower carrier relaxation time is expected for a higher pump fluence, which qualitatively agrees with both our results and ref[44, 45]. Therefore, a fluence dependent carrier relaxation can be regarded as a generic feature of metallic system in optical pump probe reflectivity studies.

To examine the possibility of a photo-induced insulator-to-metal transition in the low temperature insulating phase, we perform fluence dependent pump probe studies on $Ca_2Ru_{0.92}Fe_{0.08}O_4$ at ambient temperature. Figure 4.5 shows that the reflectivity transient scales linearly with pump fluence up to $F_{th} \sim 13$ mJ/cm^2. Beyond that, ΔR/R(t = 0) saturates and starts to decrease just before the damage threshold around 40 mJ/cm^2 [Fig. 4.5(b)]. In addition, carrier relaxation rate does not change below F_{th} but slows down above F_{th} [Fig. 4.5(c)(d)], which consistent with the response of a metallic system. We can eliminate photo-heating as the origin of the relaxation rate slowing-down because for the same pump fluence the relaxation dynamics remains unchanged from 295 K to 350 K [Fig. 4.6], and a pump fluence at F_{th} is not able to significantly heat the sample from 295 K.

Since 1.55 eV is close to the isosbestic point in the optical conductivity spectrum of $Ca_2Ru_{0.92}Fe_{0.08}O_4$, reflectivity change at this wavelength is expected to be small between the insulating phase and the metallic phase. A more dramatic change is expected in the terahertz (THz) spectrum. Figure 4.7 shows the THz reflectivity transient at a few difference pump fluences across F_{th}, where only a small change (ΔE/E $< 1\%$) is observed after optical excitation. In addition, the THz reflectivity transient shows a long-lived plateau from 1 ps onwards, which persists to hundreds of picoseconds. Although the peak of THz reflectivity transient also saturates above F_{th}, the magnitude of the plateau does not show any critical behavior with pump fluence. Instead, it scales linearly with pump fluence [Fig. 4.7(b)]. The lack of dramatic increase in ΔE/E above F_{th} is inconsistent with a photo-induced metastable metallic phase. Instead, the observed change in ΔE/E is consistent with heating. The linear fluence dependence of the plateau suggests that the material continues to absorb photon even beyond the apparent saturation in ΔR/R and ΔE/E. Therefore, although a metastable metallic phase is unlikely to be present above F_{th}, a funda-

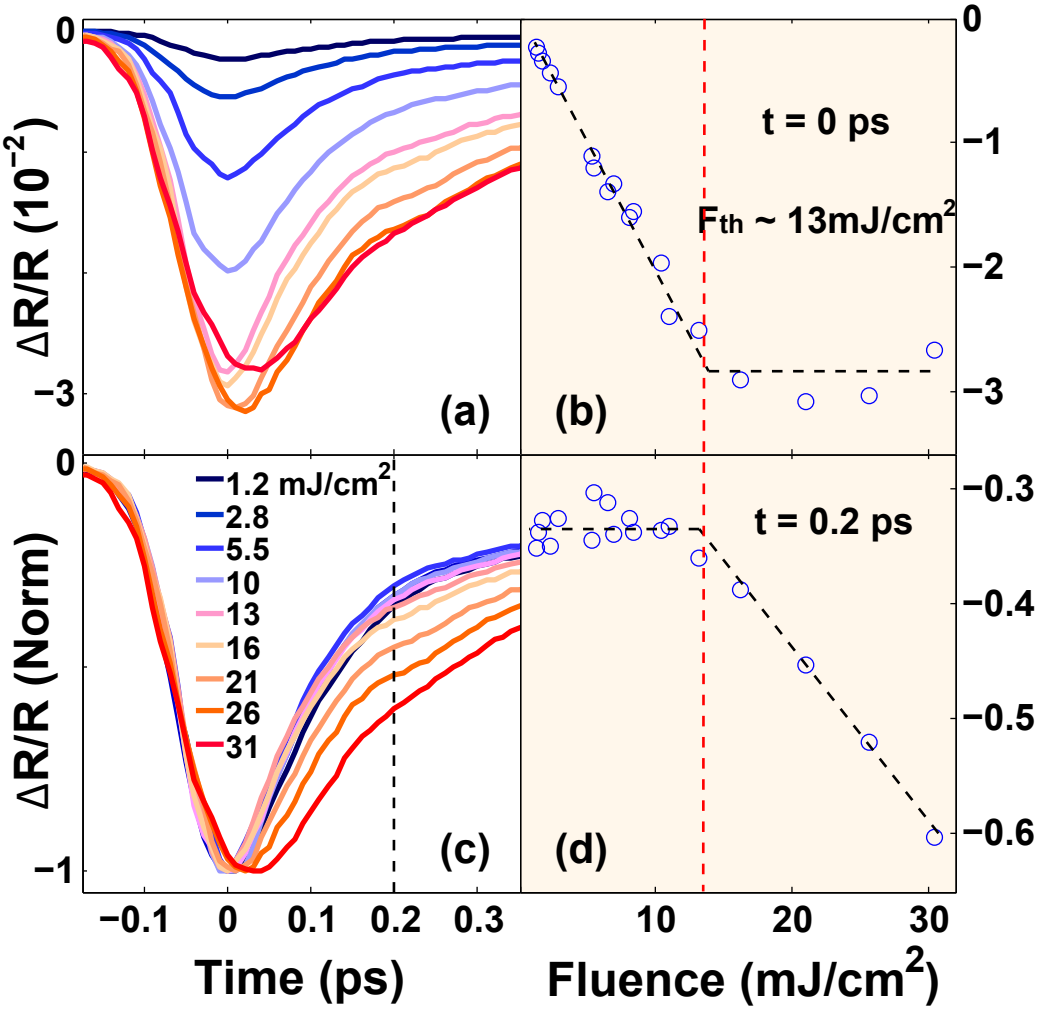

Figure 4.5: **Fluence dependence of transient reflectivity at T = 295 K.(a)** Fluence dependent reflectivity transients show **(b)** a linear increase in ΔR/R(t=0) with fluence up to 13 mJ/cm^2, which is marked as F_{th} and the red dotted line. **(c)** The same set of reflectivity transients normalized to ΔR/R(t=0) to contrast their relaxation dynamics. **(d)** To directly visualize the change in relaxation rate, the value of ΔR/R(t=0.2 ps) is extracted from each reflectivity transient and plotted as a function of fluence. A discontinuity is also observed near F_{th} ~ 13 mJ/cm^2.

mental change in the electronic structure must have taken place to account for the saturation as well as the change in the carrier relaxation.

A most likely scenario is a partial spectral weight transfer into the Mott gap by photo-excitation above F_{th}, either due to photo-doping effect or reduced electron correlation. A finite spectral weight at the Fermi energy would give rise to a slower carrier relaxation with increasing pump fluence, as predicted by the two tempera-

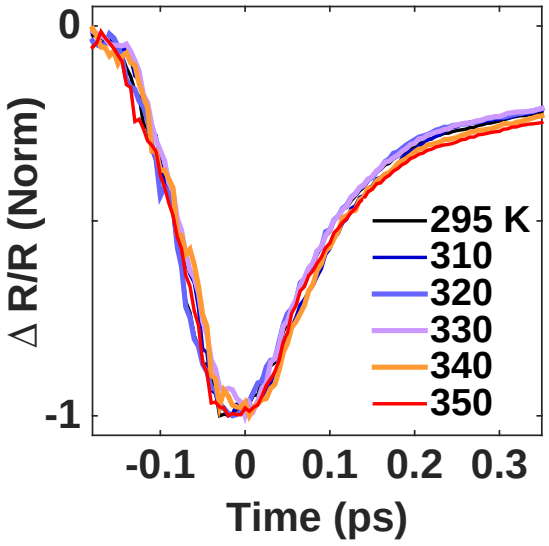

Figure 4.6: **Temperature dependence of transient reflectivity**. The fluence used is 3.8 mJ/cm^2. The reflectivity transient shows little dependence on temperature.

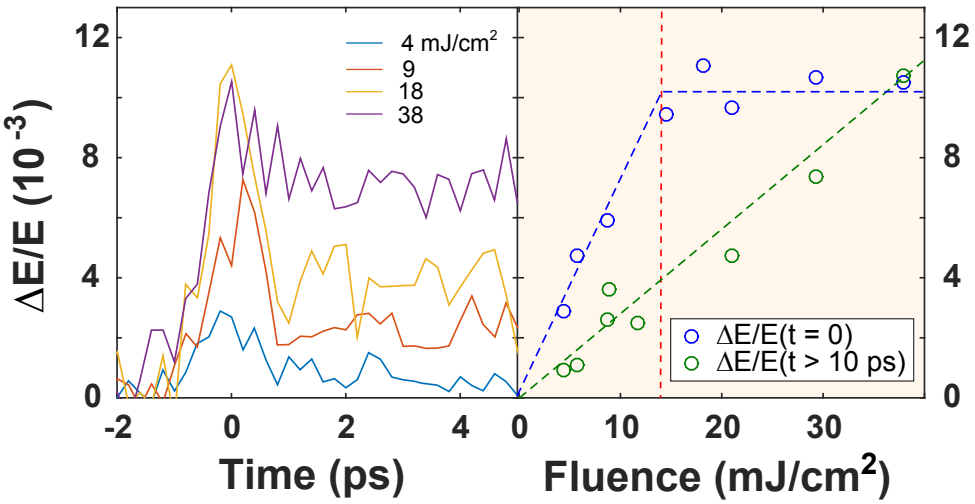

Figure 4.7: **Fluence dependence of transient terahertz reflectivity at T = 295 K**. **(a)** THz reflectivity transient for a few different pump fluences across $F_{th} \sim$ 13 mJ/cm^2. A long-lived plateau in ΔE/E is observed from 1 ps onwards, which persists out of the window to hundreds of picoseconds. **(b)** Fluence dependence of the ΔE/E peak (blue) and plateau (green).

ture model. However, this state is distinct from a truly metallic state characterized by the collapse of the Mott gap and a high THz reflectivity. In fact, lattice dynamics reveals that $Ca_2Ru_{0.92}Fe_{0.08}O_4$ retains the low temperature insulating structure

even above F_{th}, which does not support a metallic electronic state [23]. Figure 4.8(a) shows the coherent optical phonon oscillations extracted from the optical reflectivity transient at different fluences. At low fluences, the coherent oscillation is centered at 3.3 THz and can be attributed to an A_g optical phonon mode [42]. As fluence increases towards F_{th}, damping becomes stronger. This is most likely due to better screening by more photoexcited electrons. Simultaneously, a second mode becomes visible near F_{th}. This mode is heavily damped and is only resolvable within the first 1 ps. Fourier transform shows that the A_g mode does not show any softening across F_{th} [Fig. 4.8(b)] while in thermally induced IMT it completely softens at T_{IMT} [Fig. 4.8(c)]. Since the A_g mode is robust through F_{th}, we conclude that $Ca_2Ru_{0.92}Fe_{0.08}O_4$ retains the insulating S-Pbca lattice structure above F_{th}.

The electronic properties of Ca_2RuO_4 have been shown to be highly sensitive to the occupancy of the d_{xy} and $d_{xz/yz}$ orbitals within the 2/3 - filled t_{2g} manifold. Above T_{IMT} where the L-Pbca structure is realized, the d_{xy} and $d_{xz/yz}$ orbitals are approximately equally occupied and the system realizes an electronically isotropic metal. Below T_{IMT}, on the other hand, cluster dynamical mean-field theory calculations [23] show that the L-Pbca to S-Pbca structural distortion shifts the orbital occupancies by altering their crystal-field splitting and relative bandwidths, creating a completely filled d_{xy} band and half-filled $d_{xz/yz}$ bands. This, in turn, generates a Mott instability in the d_{xz} and d_{yz} bands that drives the system into a d_{xy} ferro-orbital ordered insulating phase. Our results suggest that optical excitation within the t_{2g} complex using 1.55 eV photons induces spectral weight transfer into the Mott gap without collapsing the Mott gap. As a result, the material gains some metallicity but is far from being a real metal. Moreover, the lattice structure does not undergo a first-order transition as in the thermally-induced IMT case, therefore any transient metallicity would not be supported by the low temperature S-Pbca structure. As a result of all these, optical excitation at 1.55 eV energy does not induce a metastable metallic phase in Ca_2RuO_4.

This is in stark contrast with VO_2 which has a similar thermally induced IMT concomitant with a monoclinic-to-rutile structural phase transition, and strong photoexcitation in VO_2 induces an IMT together with the structural phase transition [9, 37]. The metallic phase in VO_2 is metastable and persists for over 100 ps. Such contrasting lifetimes may be due to the fact that the there exist metastable structural phases in VO_2 close in energy to the high temperature rutile phase [47, 48], which can be accessed via optical excitation and which are commensurate with an itinerant or-

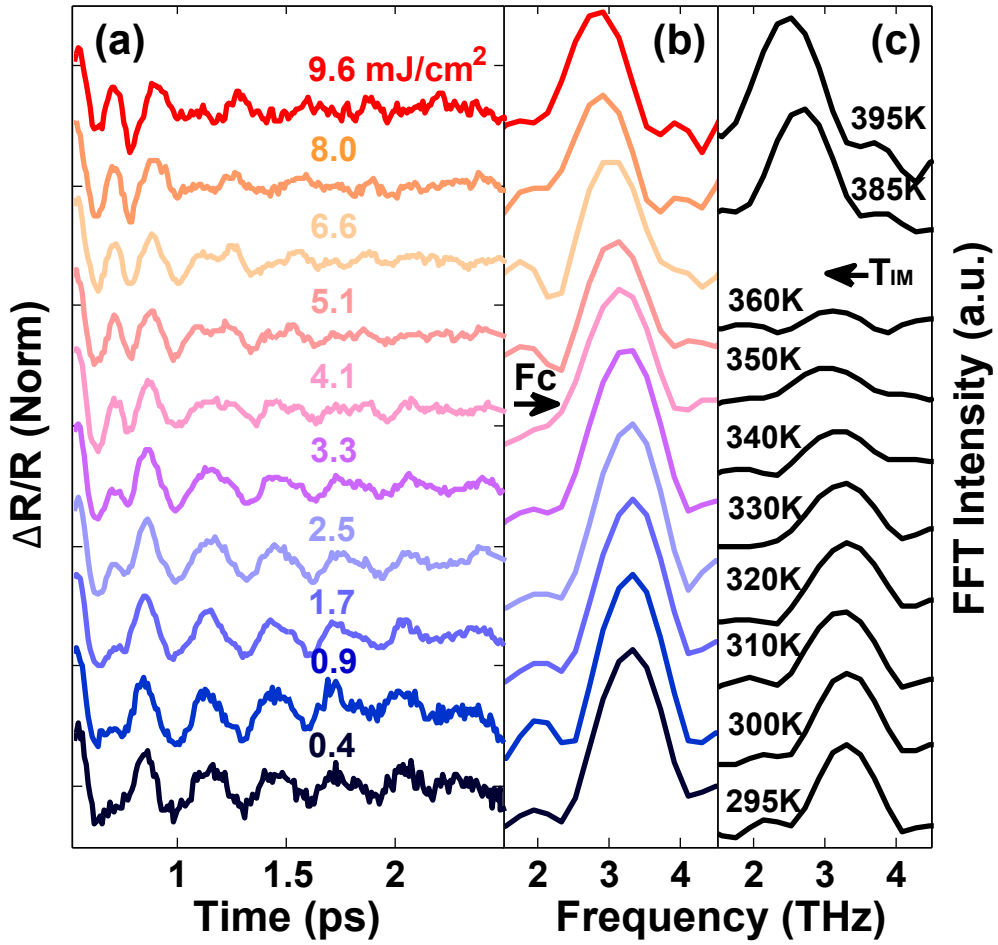

Figure 4.8: **Fluence dependence of phonon dynamics in Ca2RuO$_4$ at T = 295 K**. **(a)** Background-subtracted and normalized (by fluence) reflectivity transients showing coherent phonon oscillations. At low fluence, the coherent phonon is attributed to an A$_g$ mode. Above the threshold fluence, F_{th}, an additional mode, which is quickly damped within one or two periods, becomes noticeable. **(b)(c)** Fourier spectrum of the A$_g$ mode at **(b)** different fluences and **(c)** different temperatures.

bital occupancy. On the other hand, no competing metastable structural phases have been observed in Ca_2RuO_4, making photo-induced IMT difficult to realize. It will also be interesting to search for photo-induced phase transitions in wider classes of ruthenates such as $PbRuO_3$ [49] and even $5d$ transition metal oxides where the effects of strong spin-orbit coupling give rise to additional competing microscopic interactions.

Chapter 5

Optical pump probe investigations of the electronic structures of electron- and hole-doped Sr_2IrO_4

5.1 Introduction

The Ruddlesden-Popper series of iridium oxides, $Sr_{n+1}Ir_nO_{3n+1}$, realize a unique correlated electronic system somewhat analogous to the cuprate high temperature superconductor family. Both materials crystalize in tetragonal lattice structure, exhibit antiferromagnetic insulating ground state [50], develop similar fermiology upon doping [51–54]. In particular, the single layer Sr_2IrO_4 has been shown to host pseudogap [51] and possibly *d*-wave superconductivity [52] upon electron doping. Interestingly, unlike the undoped cuprate which is a Mott insulator, Sr_2IrO_4 shows characteristics of a Slater insulator [55, 56]. Both experiment and theory have suggested that magnetic order is indispensable for the insulating ground state of Sr_2IrO_4 [55–57]. On the other hand, La- and Rh-substitution which dopes electron and hole respectively into Sr_2IrO_4 are shown to modify the electronic ground state and magnetic order of Sr_2IrO_4. In particular, in $Sr_2Ir_{1-x}Rh_xO_4$, T_N decreases continuously with x up to x = 0.17, where magnetic ordering is completely suppressed and $Sr_2Ir_{1-x}Rh_xO_4$ becomes a metal [54, 58, 59]. A similar suppression of magnetic ordering and an insulator-to-metal transition is induced in $(Sr_{1-x}La_x)_2IrO_4$ near x = 0.05 [53, 54, 58]. While the electronic ground state of the doped Sr_2IrO_4 have been measured at cryogenic temperature [51, 53], a detailed study of their temperature evolution across T_N has not been done to our knowledge. This is in part due to issues with energy resolution at elevated temperatures for probes like angle-resolved photoemission spectroscopy (ARPES). In this study, we use time-resolved optical reflectivity, which is suitable for probing electronic structure at elevated temperatures, to study their evolution across T_N. In addition, we show that by photo-heating or photo-doping these samples, we close the insulating gap in Sr_2IrO_4.

5.2 Experimental

For our time-resolved optical reflectivity study, we employ a regeneratively amplified Ti:Sapphire laser that outputs 80 fs pulses centered around 795 nm (1.5 eV) at 10 kHz repetition rate. The pump beam passes through a delay stage and a mechanic chopper chopping at half of the laser repetition rate. The pump and probe

beams are cross-polarized and focused at near normal incidence onto the sample with a spotsize of 60 μm FWHM. The reflected probe beam from the sample is detected by a photodiode connected to a lock-in amplifier. All time-resolved reflectivity measurements are carried out in vacuum better than 2×10^{-7} mbar. A balanced detection geometry involving a second reference probe beam, together with polarization filtering, allows a signal-to-noise ratio better than 10^{-5} in ΔR/R.

Our samples include electron-doped $(Sr_{1-x}La_x)_2IrO_4$ with x = 0.045, hole-doped $Sr_2Ir_{1-x}Rh_xO_4$ with x = 0.03, 0.11, 0.15, as well as the insulating parent. These single crystals were grown using the self flux technique. The La and Rh concentration was determined by energy-dispersive X-ray spectroscopy (EDX). Details of the growth procedure can be found in ref [60].

5.3 Results

The insulating ground state of Sr_2IrO_4 is due to strong spin-orbit coupling of the $5d$ electrons which splits the d^5 electron configuration of Ir^{4+} into a fully filled J_{eff} = 3/2 band and a narrow half-filled J_{eff} = 1/2 band. Moderate Coulomb interaction is then able to split the J_{eff} = 1/2 band into an empty upper Hubbard band (UHB) and a fully-occupied lower Hubbard band (LHB). Optical conductivity measurements have shown that the J_{eff} = 3/2 valence band and the J_{eff} = 1/2 LHB are separated from the J_{eff} = 1/2 UHB approximately by 1 eV and 0.5 eV respectively [61]. Therefore, the 1.5 eV excitation pulse promotes electrons from the bottom of the J_{eff} = 3/2 valence band to the J_{eff} = 1/2 UHB and the degenerate probe beam monitors the subsequent relaxation of the photo-excited electrons.

Earlier time-resolved optical reflectivity experiment on Sr_2IrO_4 has established a bi-exponential relaxation dynamics for the photo-excited electrons for excitation fluence less than 20 μJ/cm^2 [56]. In this model $\Delta R/R = Ae^{-t/\tau_1} + Be^{-t/\tau_2} + C$, τ_1 was interpreted as the time constant for electron thermalization via electron-phonon scattering, τ_2 was understood as the time constant for bimolecular recombination of electron-hole pairs across the Mott gap. By a few picosecond delay, these dynamical processes are completed and the probed region of the sample reaches a quasi-thermal equilibrium. This part of the reflectivity transient is described by the constant C representing the change in reflectivity due to the increased temperature of the sample after photo-excitation. C decays to zero on a much longer timescale limited by phonon-phonon scattering time. Figure 5.1 shows the reflectivity transients from Sr_2IrO_4 at a few different temperatures across $T_N \sim 240$ K. To visualize

the slow component of the bi-exponential relaxation, we plot the normalized reflectivity transients on log scale in Fig. 5.1(b). By comparing these reflectivity transients to an exponential function $e^{-t/\tau}$ with τ = 1 ps, it can be seen that the τ_2 is on the order of 1 ps. Similar exponent is also observed in the relaxation of ΔR/R in La- and Rh-doped samples and is the main focus of this study.

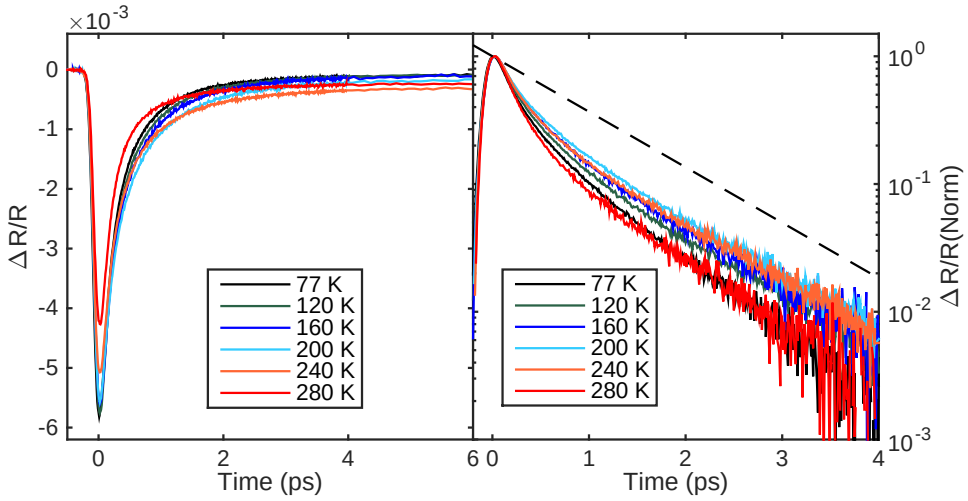

Figure 5.1: . (a) Reflectivity transients from Sr_2IrO_4 across $T_N \sim 240$ K using 20 μ/cm^2 excitation fluence. (b) The same reflectivity transients in (a) with their constant offset C subtracted and then normalized to the peak, plotted on log scale to emphasize the slow component of the bi-exponential relaxation. The dotted line is $e^{-t/\tau}$ with τ = 1 ps.

Figure 5.2 shows the normalized reflectivity transients from Sr_2IrO_4 as well as the La- and Rh-doped Sr_2IrO_4 from 77 K to 280 K. The Néel temperature for these three samples are 240 K, 210K and negative respectively. In Sr_2IrO_4, the relaxation rate first slows down on heating up towards T_N. Once above T_N, it increases again. This is corroborated by the fit results shown in Fig. 5.2(d), where τ_2 peaks near T_N. In comparison, the La- and Rh- doped samples show monotonic increase in relaxation rate in the same temperature range. Previous time-resolved optical reflectivity experiment has found evidence for Mott gap closing above T_N in Sr_2IrO_4 [56]. This is corroborated by the peaking of τ_2 near T_N in our data. The divergence of electron relaxation time near gap-closing is both predicted by theory and experimentally observed in a number of systems [56, 62, 63]. In the presence of a gap Δ at the Fermi energy, non-radiative recombination of an electron-hole pair creates a boson, typically in the form of a phonon, of energy Δ. This boson can un-

dergo the reverse process to self-annihilate and create a new pair of electron-hole, or decay anharmonically into bosons of smaller energy. The rate of the two processes are determined by the number density of the electron-hole pairs and the low energy bosons, which is dominated by thermal population. Near the gap-closing temperature, Δ is small and thermally occupied bosons with energy greater than Δ are abundant. Therefore, electron-hole pair recombination is thwarted, leading a divergence in their relaxation time. Detailed mathematical formulation of this model can be found in ref [63]. Here, it suffices to note that τ_2 diverges near T_N in Sr_2IrO_4 but monotonically decreases in La- and Rh-doped Sr_2IrO_4. Together with the lack of bimolecular recombination signature in the latter two samples, this indicates that the gaps in the two systems are already at least partially filled with a finite density of states down to 77 K.

Further understanding of metallic response in time-resolved optical reflectivity can be obtained from the fluence dependence of relaxation rate. When a gap is present at the Fermi energy, as discussed in [56] the rate of electron-hole recombination increases with excitation fluence due to the greater probability for an electron to find a hole. However, when there is a finite density of states (DOS) at the Fermi energy, the number of excited electrons, n, after electrons thermalize among themselves is directly related to the electronic temperature by an approximate linear relation: $dn \propto dT_e$. Since ΔR/R measures n, it is also a measure of the electronic temperature. Under this interpretation, τ_2, the slow component of reflectivity relaxation, describes the heat exchange between the electron and phonon subsystems that brings the entire system to quasi-thermal equilibrium via electron-phonon scattering.

Using a two temperature model, we can describe the heat exchange between the electrons and the lattice by the coupled equations

$$C_e(T_e)dT_e/dt = -g(T_e - T_p) \tag{5.1}$$

$$C_p(T_p)dT_p/dt = g(T_e - T_p) \tag{5.2}$$

where g is the electron-phonon coupling constant, T_e and T_p are the electron and phonon temperatures respectively. For metals, the electronic specific heat $C_p(T_e) = \gamma T_e$, where $\gamma = \pi^2 k_B^2 g(\epsilon)/3$, k_B is the Boltzmann constant and $g(\epsilon)$ the DOS at the Fermi energy. Using experimentally determined values of γ for Rh-doped Sr_2IrO_4 and $C_p(T)$, we simulate the heat exchange process and find that photo carrier relaxation becomes slower with higher excitation fluence, as shown in Fig. 5.3(d). Indeed, fluence dependent reflectivity transients on La- and Rh-doped Sr_2IrO_4 at

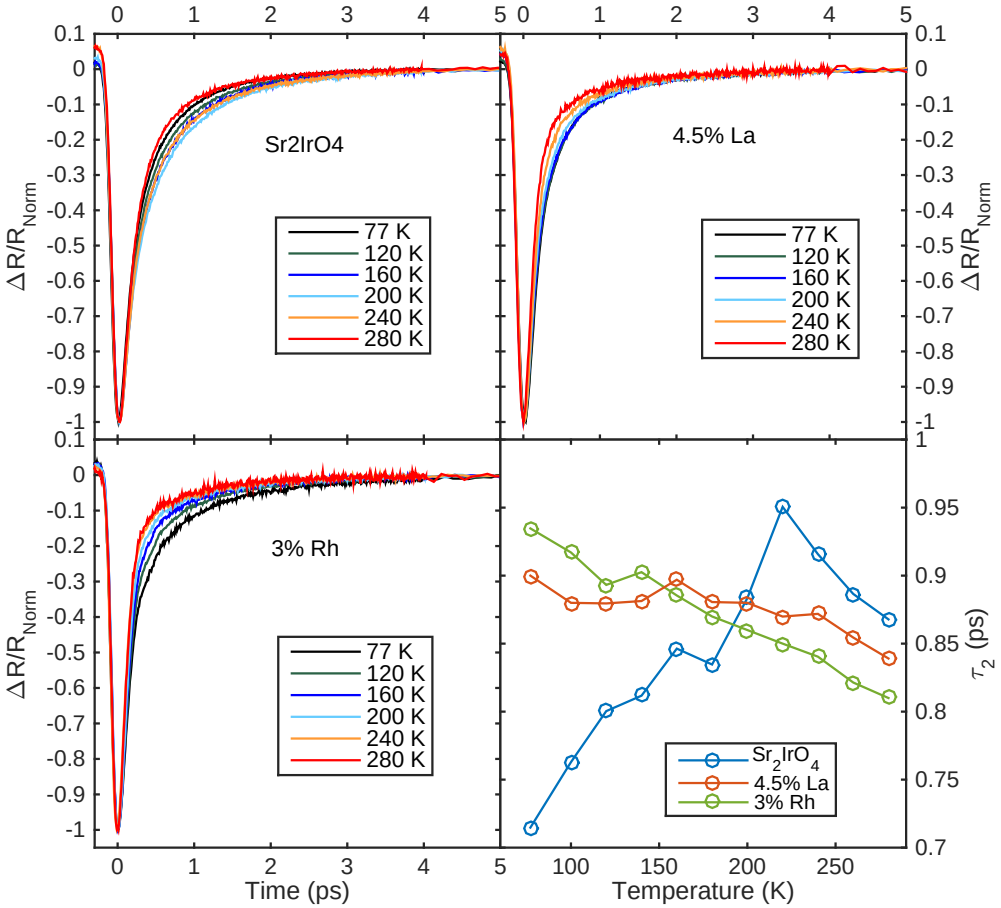

Figure 5.2: Reflectivity transients from (a) Sr_2IrO_4, (b) $(Sr_{1-x}La_x)_2IrO_4$ with x = 0.045, (c) $Sr_2Ir_{1-x}Rh_xO_4$ with x = 0.03, for a range of different temperature using 200 μ/cm^2 excitation fluence. The reflectivity transients have their offset C subtracted and then normalized to the peak in order to better visualize the relaxation rate. (d) The time constant of the slow exponential, τ_2, from fit is plotted against temperature for the three samples.

77 K exhibit a relaxation rate that slows down with increasing pump fluence: Fig. 5.3(b)(c). On the other hand, Fig. 5.3(a) shows that at 77 K, the relaxation rate in Sr_2IrO_4 increases with fluence initially (< 1 mJ/cm^2), consistent with the bi-molecular recombination of electron-hole pairs, but then it slows down with higher excitation fluence (> 1 mJ/cm^2), signifying a filling of DOS at the Fermi energy.

One plausible explanation for this photo-induced gap filling is that the electron temperature is heated above T_N by photo-excitation, reproducing the Mott gap closing above T_N in equilibrium measurements. The electron temperature could be esti-

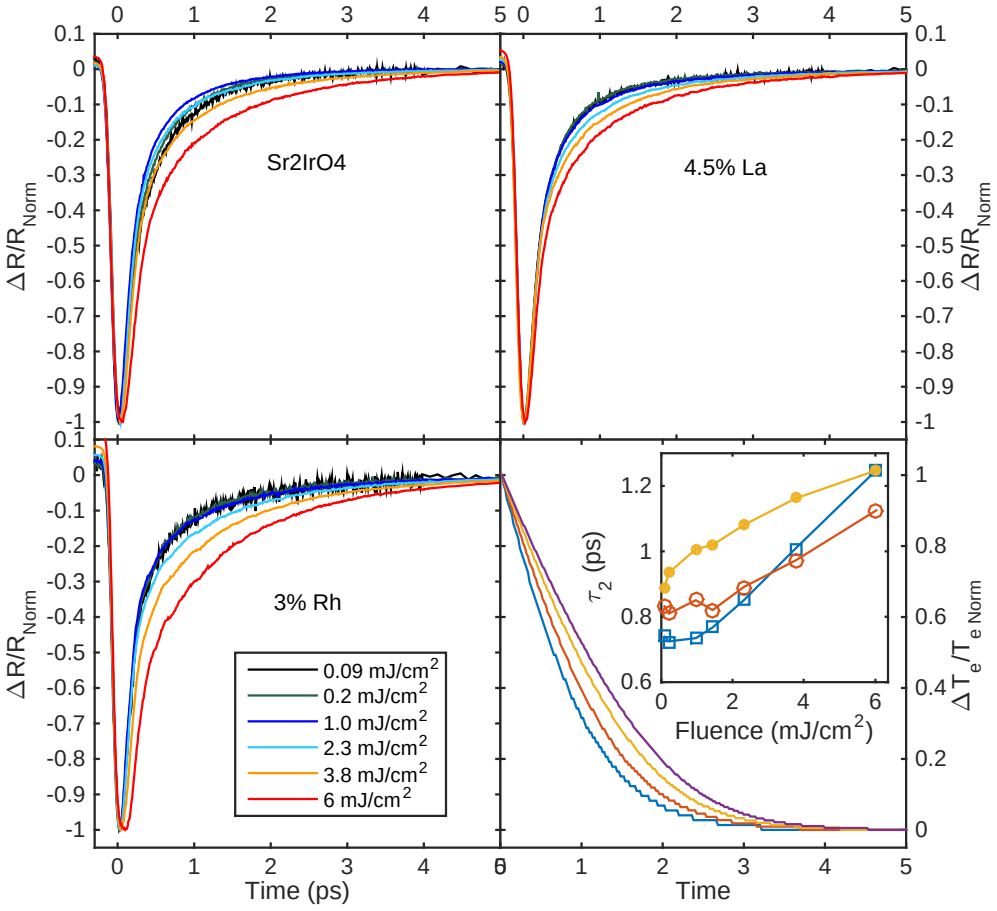

Figure 5.3: Reflectivity transients from (a) Sr_2IrO_4, (b) $(Sr_{1-x}La_x)_2IrO_4$ with x = 0.045, (c) $Sr_2Ir_{1-x}Rh_xO_4$ with x = 0.03 at 77 K for a range of different excitation fluences. The reflectivity transients are normalized in the same way as in Fig. 5.2. (d) Simulation of the decay of electron temperature over time for different initial temperatures. Each decay is normalized to the initial temperature change. Inset shows the time constant of the slow exponential, τ_2, extracted from fit against fluence for the three samples.

mated using $Q_e = 1/2\gamma T_e^2$, and the amount of pulse energy absorbed is ΔQ_e = (1 - e^{-1})FV_m/ξ, where F is the pump fluence, V_m is the molar volume, and ξ is the optical penetration depth of Sr_2IrO_4 at 795 nm. ξ is estimated similarly to [56]. Using this, a fluence of 14 μJ/cm^2 is found to be necessary to heat the electrons instantaneously to T_N = 240 K, way much smaller than the threshold fluence of 1 mJ/cm^2. However, if we stipulate that the entire electron-lattice system be heated above T_N after thermal equilibration, then the two temperature model above gives

a critical fluence of about 3 mJ/cm^2, which is close to our experimentally observed threshold fluence.

Another explanation for the photo-induced gap filling is photo-doping. Since each absorbed photon creates an electron-hole pair, photo-excitation can be thought as producing similar effects as chemical doping. The density of electron-hole pairs created by the pump pulse can be estimated by $n = (1 - e^{-1})N \cdot N_A/(A \cdot \xi)$, where N is the number of photons per pump pulse, N_A Avogadro's number, A the area of the pump beam, ξ the optical penetration depth. Since La- and Rh-doping on the order of a few percent is enough to create a finite DOS at the Fermi energy, an electron-hole pair density on the order of $n \sim 0.01$ is sufficient for inducing an insulator-to-metal transition. This translates into a fluence on the order of a few 100 μJ/cm^2.

The inset of Fig. 5.3(d) shows that τ_2 increases with fluence more steeply for Sr_2IrO_4 (> 1 mJ/cm^2) than for La- and Rh-doped samples. This is expected because γ is proportional to the DOS at the Fermi energy. Experimentally γ has been measured to be $\sim$ 1.8 mJ/mol·K^2 for Sr_2IrO_4 and increases to $\sim$ 7 mJ/mol·K^2 for 11% Rh-doped Sr_2IrO_4. A larger γ reduces the initial electron temperature, which according to the two temperature model [Fig. 5.3(d)], causes τ_2 to be smaller.

Fig. 5.4(a)(b) shows the reflectivity transients from 11% Rh-doped Sr_2IrO_4 as a function of temperature and fluence. Interestingly, a negative component reminiscent of the lower Rh-doped samples is present in reflectivity transient at low temperature and low fluence. It disappears with both temperature and fluence, leaving behind a purely positive response similar to the 15% Rh-doped sample [Fig. 5.4(d)]. For the 15% Rh-doped sample, however, $\Delta R/R$ is entirely positive and is linear with fluence. The insensitivity of the relaxation rate to fluence in 15% Rh-doped Sr_2IrO_4 might be due to a much larger value of γ in the sample. Overall, our data suggest that the high temperature or the high fluence limit of the 11% Rh-doped Sr_2IrO_4 approaches that of 15% Rh-doped Sr_2IrO_4 in the optical pump probe reflectivity study, suggesting similar effects between temperature increase and photo-excitation in Rh-doped Sr_2IrO_4.

In conclusion, our pump probe reflectivity study of differently doped Sr_2IrO_4 shows that a finite density of states is present in the Mott gap above T_N in parent Sr_2IrO_4 and above 77 K in Rh- and La-doped Sr_2IrO_4. Moreover, photoexcitation induces a similar filling of the Mott gap in parent Sr_2IrO_4. All these observations point to a similar role between heating and thermal excitation in Sr_2IrO_4.

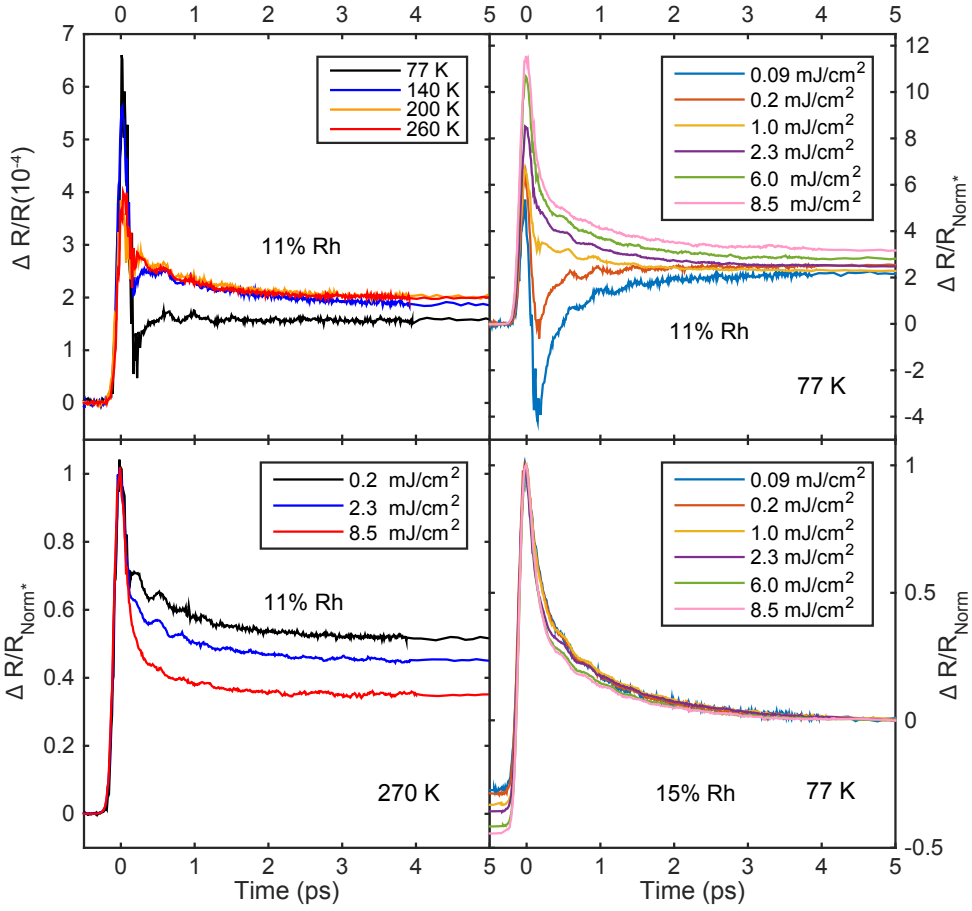

Figure 5.4: (a) Reflectivity transients from $Sr_2Ir_{1-x}Rh_xO_4$ with x = 0.11 for different temperatures with an excitation fluence of 200 μJ/cm^2. (b) Reflectivity transients from x = 0.11 sample at 77 K with different excitation fluences, normalized by the fluence. (c) Reflectivity transients from x = 0.11 sample at 270 K with different excitation fluences, normalized by the peak. (d) Reflectivity transients from x = 0.15 sample at 77 K with different fluences, normalized in the same way as in Fig. 5.2.

Chapter 6

Hidden order phase in Sr_2IrO_4 revealed by second harmonic generation rotational anisotropy

6.1 Introduction

In an archetypical Mott insulator, strong Coulomb repulsion (U) forbids intersite hopping and splits an otherwise half-filled conduction band into a fully filled lower Hubbard band (LHB) and an empty upper Hubbard band (UHB) below and above the Fermi energy. This is exemplified by $3d$ transition metal oxides (TMOs), the first discovered Mott insulators. In $4d$ and $5d$ TMOs, the delocalization of $4d$ and $5d$ electrons reduces U and places many TMOs near the border of insulator-to-metal transition. The fragility of the insulating ground states in these compounds is illustrated in Ca_2RuO_4, which is a $4d$ TMO. $5d$ TMOs, with even weaker U, are therefore expected to be metallic.

Despite having an odd number of electrons per formula unit and a very small U, $5d$ TMO Sr_2IrO_4 has an insulating gap of about 0.4 eV as determined from optical conductivity measurement [61]. The insulating nature of Sr_2IrO_4 in the presence of delocalized $5d$ electrons arises from strong spin-orbit coupling (SOC) interaction of the $5d$ electrons. Strong SOC splits the five t_{2g} orbital states in Ir^{4+} into lower-lying spin-orbit coupled J_{eff} = 3/2 states and higher-lying J_{eff} = 1/2 states. The J_{eff} = 3/2 states are fully filled by four electrons while the J_{eff} = 1/2 states are partially occupied by one electron. With the reduced bandwidth of the J_{eff} = 1/2 states, small Coulomb interaction is now able to open up an insulating gap in Sr_2IrO_4 [50].

As shown in Fig. 6.1(a), Sr_2IrO_4 crystalizes in the tetragonal K_2NiF_4 structure as La_2CuO_4 [50]. Despite strong SOC, the magnetic interaction in Sr_2IrO_4 is Heisenberg-type with three-dimensional long range order below $T_N \sim 230$ K. The J_{eff} = 1/2 moments arrange in a canted antiferromagnetic order which produces a weak in-plane moment [Fig. 6.1(b)]. Due to the similarity in the lattice, electronic and magnetic structure between Sr_2IrO_4 and cuprate high-T_c superconductor (HTSC) parent compound, it is anticipated that electronic phases similar to those in cuprate HTSC might also realize in doped Sr_2IrO_4. Almost concurrent with our experiments, pseudogap and possibly d-wave superconductivity are reported in electron-doped Sr_2IrO_4 [51, 52]. In this study we use SHG-RA to search for

symmetry-broken phases in Sr_2IrO_4 that might be similar to those in cuprate HTSC.

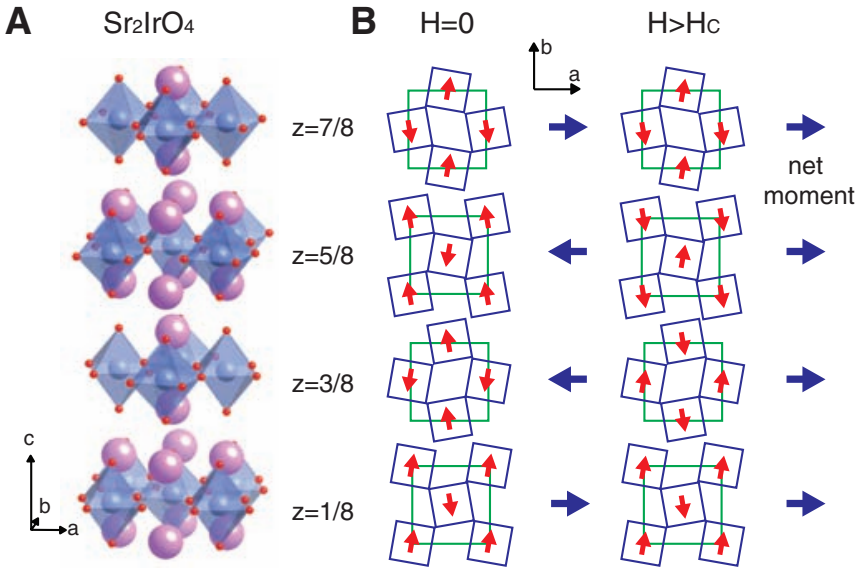

Figure 6.1: **Lattice and magnetic structure of Sr_2IrO_4.** **A**. Each unit cell of Sr_2IrO_4 consists of four layers of IrO_6 octahedra, which undergo a staggered correlated rotation of $\sim 12^\circ$ about the c-axis. **B**. The $J_{eff} = 1/2$ moments order in a canted antiferromagnetic fashion below T_N, which gives rise to a weak in-plane moment. Figure taken from [64].

6.2 Experiment and results

The SHG-RA experiments are performed using 800 nm (1.5 eV) beams focused onto ~ 50 μm-diameter spot on the sample. The pulse energy for the 800 nm beam is $\sim$100 nJ and the pulse duration is $\sim$ 100 fs. The Sr_2IrO_4 samples are cleaved in air and then quickly transferred to the optical cryostat and pumped down to vacuum.

The reported crystalline point group of Sr_2IrO_4 is the centrosymmetric 4/mmm (space group $I4_1/acd$) [64–66]. Figure 6.2 shows the SHG-RA patterns collected from Sr_2IrO_4 at room temperature. A centrosymmetric lattice forbids bulk electric dipole radiation $\chi^{ED}_{ijk} E_j(\omega) E_k(\omega)$, instead SHG has to come from bulk electric quadrupole radiation $\chi^{QD}_{ijkl} E_j(\omega) \nabla_k E_l(\omega)$ or surface electric dipole radiation (where inversion symmetry is broken and χ^{ED} does not vanish). Assuming the bulk electric quadrupole radiation, the SHG-RA data can be nicely fit assuming a centrosymmetric 4/m point group. The reported 4/mmm point group requires mirror planes in the ac and bc planes, which are broken due to the rotation of the SHG-RA peaks from the a, b axes. Moreover, the form of $\chi^{QD}_{4/mmm}$ constrains the P_{in}-S_{out} (PS) and S_{in}-S_{out} (SS) polarization combinations to be eightfold rotational

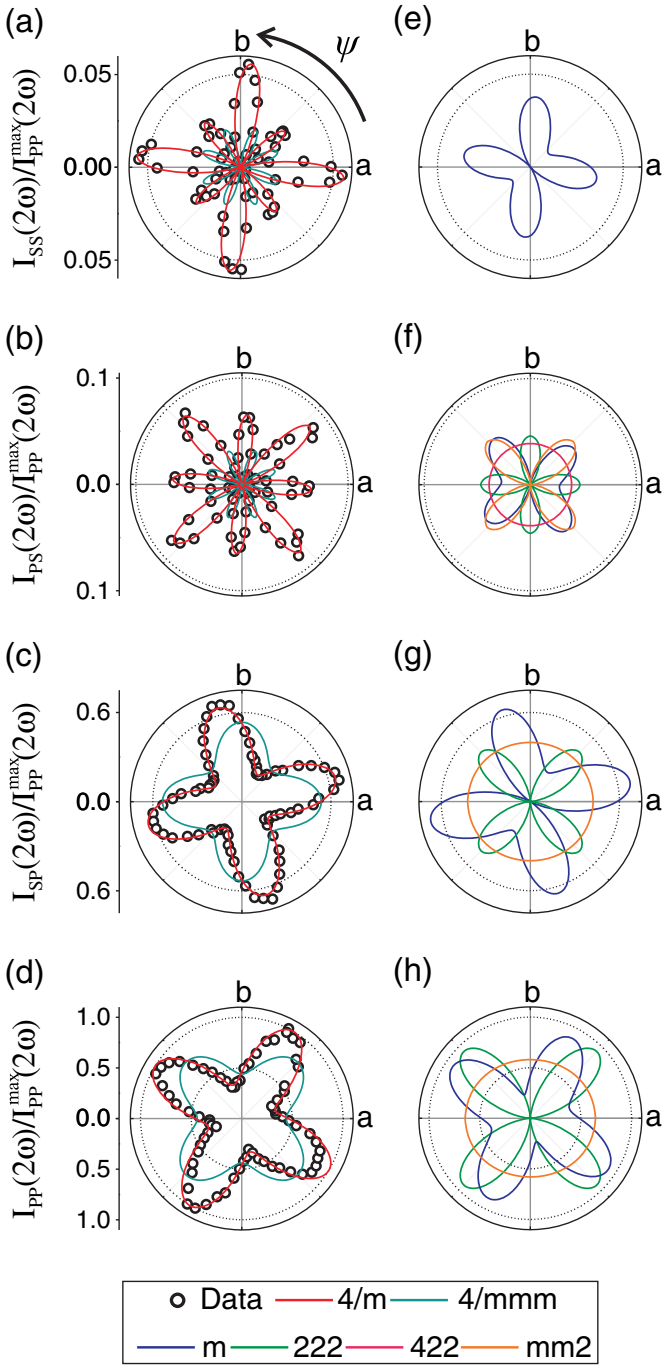

Figure 6.2: **SHG-RA patterns collected from Sr_2IrO_4 at room temperature**. **(a)(b)(c)(d)** SHG-RA patterns in four different polarization combinations. The intensities of all patterns are normalized to the peak in the P_{in}-P_{out} (PP) pattern. Red (green) solid line is fit to the 4/m (4/mmm) point group assuming bulk electric quadrupole radiation. **(e)(f)(g)(h)** Fits to other point groups assuming bulk electric quadrupole radiation.

symmetric in intensity. This clearly contradicts the PS and SS data. Together, under the assumption of bulk electric quadrupole radiation, these evidences suggest that the correct crystalline point group of Sr_2IrO_4 is 4/m instead of 4/mmm.

In order to rule out the possibility that a non-negligible surface electric dipole radiation is present and interferes with the bulk electric quadrupole radiation to give rise to the observed SHG-RA patterns, we carry out third harmonic generation rotational anisotropy (THG-RA) experiment. THG is bulk-sensitive because the χ^{ED}_{ijkl} is allowed in centrosymmetric media. Therefore, compared to the bulk electric dipole contribution to THG, surface electric dipole contribution to THG is negligible. The experiment is performed using 1.2 μm incoming beam produced from an optical parametric amplifier. Figure 6.3 shows the THG-RA patterns collected from Sr_2IrO_4 at room temperature. Similar to SHG-RA patterns, the peaks and valleys in THG-RA patterns are also rotated from the a, b axes. Additionally, for THG-RA, $\chi^{ED}_{4/mmm}$ also constrains PS and SP patterns to be eightfold rotational symmetric in intensity, which is again contradicted by the data. Instead, the bulk electric dipole contribution from the 4/m point group describes the THG-RA data remarkably well. Therefore, we conclude that the crystalline symmetry of Sr_2IrO_4 is indeed described by the point group 4/m (space group $I4_1/a$).

The reduction of crystalline symmetry from 4/mmm to 4/m necessitates the removal of the c- and d-glide planes in the $I4_1/acd$ description. This can only occur if the tetragonal distortions of the iridium-oxygen octahedra on the two sublattices are inequivalent [Fig. 6.4(b)]. This has an important consequence on the relationship between the $J_{eff} = 1/2$ moment canting and the IrO_6 octahedra rotation in Sr_2IrO_4. A widely studied model for understanding the relationship between the moment canting angle ϕ and the octahedral rotation angle α [Fig. 6.4(a)] is developed by Jacklie and Khaliullin [67] for a $I4_1/acd$ space group with uniform octahedral distortion. It was found that ϕ/α depends only on one parameter θ defined through $\tan(2\theta) = 2\sqrt{2}\lambda/(\lambda\text{-}2\Delta)$, where λ and Δ are the strength of spin-orbit coupling and tetragonal crystal field splitting. A perfect magnetoelastic locking ($\phi/\alpha = 1$) is predicted in the cubic limit ($\Delta = 0$) [Fig. 6.4(c)]. Using commonly accepted values [50, 67–70] of λ ($\sim$ 400 meV) and Δ ($\sim$ 140 meV), the JK model predicts $\phi/\alpha \sim 0.7$, which contradicts recent neutron and resonant x-ray diffraction studies that report values of $\phi = 13(1)^\circ$ [71] and $12.2(8)^\circ$ [72] and $\alpha = 11.8(1)^\circ$ [71], which indicate a nearly perfect magnetoelastic locking.

If the model is modified to allow a staggered tetragonal distortion between the two

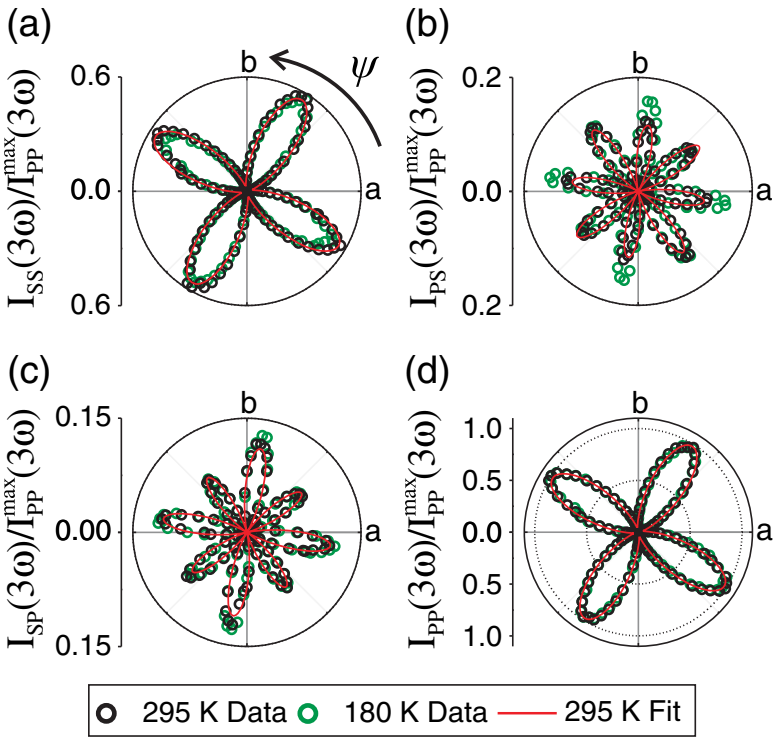

Figure 6.3: **THG-RA patterns collected from Sr_2IrO_4.** **(a)(b)(c)(d)** THG-RA patterns in four different polarization combinations normalized to the peak in the P_{in}-P_{out} (PP) pattern. The red solid line is fit to the 4/m point group assuming bulk electric dipole radiation.

sublattices ($\Delta_1 = -\Delta_2 \equiv \Delta$) [68, 73], which is consistent with the $I4_1/a$ space group, we found that ϕ/α becomes very insensitive to both λ and Δ [Fig. 6.4(d)]. Therefore, we conclude that a staggered tetragonal distortion explains the reduction of crystalline symmetry from 4/mmm (space group $I4_1/acd$) to 4/m (space group $I4_1/a$) as well as almost perfect magnetoelastic locking in Sr_2IrO_4.

With the correct crystalline symmetry of Sr_2IrO_4, we are ready to search for possible symmetry-broken phases in it at low temperature. In Fig. 6.5, we plot the SHG-RA patterns in the PP and PS polarization channels at 295 K and 170 K respectively. The rotational symmetry of the SHG-RA patterns is clearly reduced from C_4 to C_1 at 170K. We can rule out structural and antiferromagnetic order as the origin of this symmetry breaking: extensive neutron and resonant X-ray diffraction studies have found no evidence for any structural change in Sr_2IrO_4 below room temperature [64, 71, 72, 74] while the antiferromagnetic order below $T_N \sim 230$ K is described by the centrosymmetric orthorhombic magnetic point group $2/m1'$ which retains

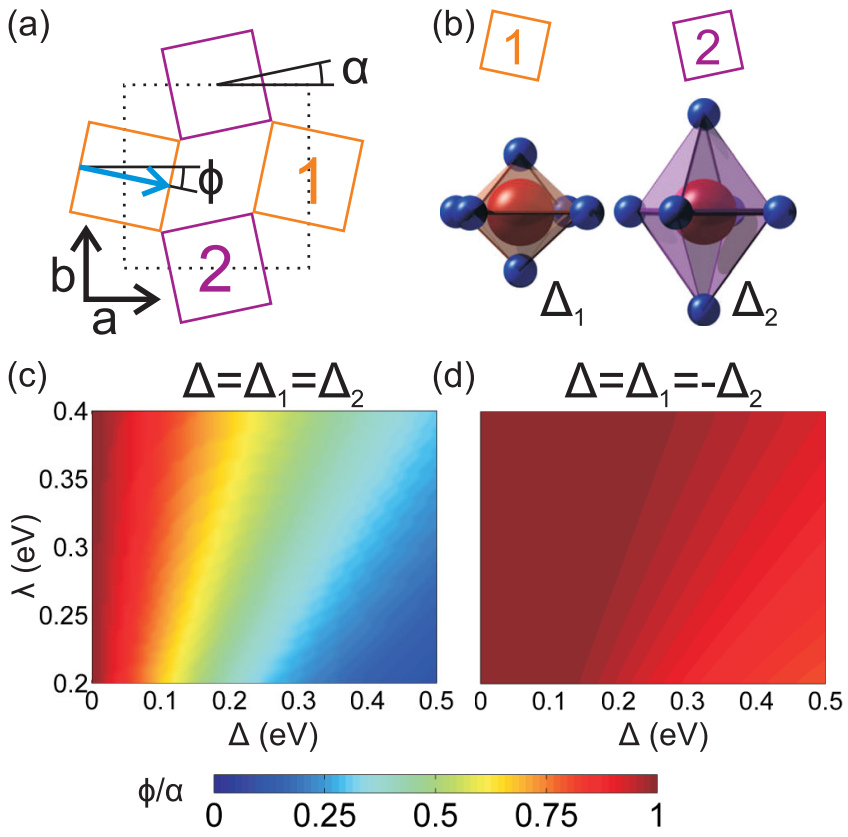

Figure 6.4: **Inequivalent tetragonal distortions of IrO_6 octahedra and spin-octahedron locking**. **(a)** Illustration of an IrO_2 plane in Sr_2IrO_4. The oxygen octahedra rotate about the c-axis by $\pm\alpha$ creating a two sublattice structure. The magnetic moments couple to the lattice and exhibit canting angles $\pm\phi$. **(b)** An unequal tetragonal distortion (Δ_1 and Δ_2) on the two sublattices as required by the $I4_1/a$ space group. **(c)** The ratio ϕ/α as a function of both λ and Δ calculated for the case of uniform and **(d)** staggered (Δ_1 = -Δ_2) tetragonal distortion

C_2 symmetry. Ferro- or antiferroelectric order can also be ruled out owing to the absence of any anomaly in the temperature dependence of the dielectric constant of Sr_2IrO_4 above 170 K [75]. The most plausible explanation for this symmetry-broken phase is the ordering of a higher multipolar degree of freedom that coexists with the J_{eff} = 1/2 moments in the IrO_6 octahedra.

To investigate the symmetry of this multipolar order, we note that 2′/m and m1′ are the only two magnetic subgroups of the crystallographic point group 4/m that do not include 2 (two-fold rotation along c) as a symmetry operation. Both 2′/m and m1′ break global inversion symmetry and allow a bulk electric dipole contribution to SHG on top of the existing bulk electric quadrupole contribution. A coherent sum

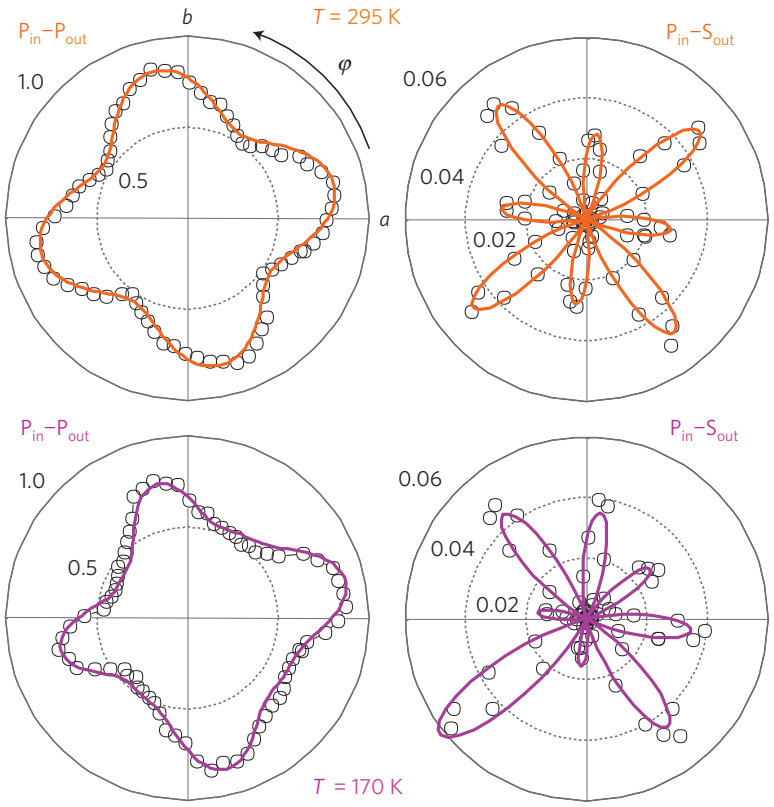

Figure 6.5: **SHG-RA patterns collected from Sr_2IrO_4 at 295 K and 170 K**. All patterns are normalized to the peak in the P_{in}-P_{out} pattern at 295 K. Orange solid line is fit to the 4/m point group assuming bulk electric quadrupole radiation. Purple solid line is fit to the coherent sum of bulk electric quadrupole radiation from a 4/m point group and bulk electric dipole radiation from a 2′/m magnetic point group.

of the crystallographic electric quadrupole radiation from the 4/m point group and the hidden-order-induced electric dipole radiation based on either the 2′/m or m1′ magnetic point group fits the data extremely well [Fig. 6.5]. This indicates that the multipolar hidden order breaks parity and hence cannot arise from the parity-even magnetic multipolar orders recently proposed for Sr_2IrO_4 below T_N [76, 77].

A microscopic model that satisfies the 2′/m or m1′ magnetic point group symmetry is the magneto-electric loop-current order, which is predicted to exist in the pseudogap region of the cuprates [78–80] but can in principle persist even at half-filling [81]. In this model, a pair of counter-circulating current loops forms in each CuO_2 square plaquette and can be described by a toroidal pseudovector order parameter [82, 83] defined as $\Omega = \sum \mathbf{r_i} \times \mathbf{m_i}$, where $\mathbf{r_i}$ is the location of the orbital magnetic moment $\mathbf{m_i}$ inside the plaquette. Four degenerate configurations are possible because

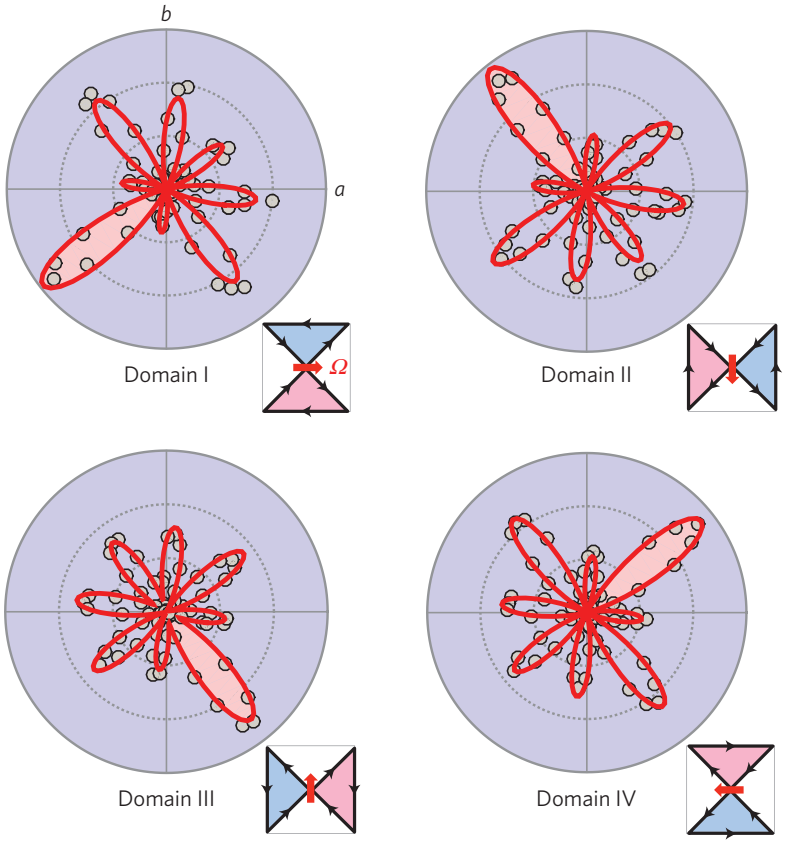

Figure 6.6: **Degenerate ground states of the loop-current model** The loop-current order Ω can exhibit four distinct configurations, which are all captured by SHG-RA on different regions of the Sr_2IrO_4 sample.

the two intra-unit-cell current loops can lie along either of the two diagonals in the square plaquette and can have either of the two time-reversed configurations, which correspond to four 90°-rotated directions of the pseudovector [Fig. 6.6]. Therefore, four types of domains are expected to manifest in the loop current phase.

To search for these domains in the hidden-order phase of Sr_2IrO_4, we perform wide-field SHG imaging in the P_{in}-S_{out} polarization channel which sees the largest change among all polarization channels. SHG images are collected from a $\sim 500\ \mu m \times 500\ \mu m$ region of the *ab* surface at room temperature and at 175 K [Fig. 6.7]. At room temperature, SHG image has a uniform intensity that is consistent with a single crystallographic domain. On cooling to T = 175 K, regions of higher and lower intensities with lateral dimension on the order of $\sim 100\ \mu m$ become visible. Upon thermal cycling, the distribution and shapes of these domains are rearranged, suggesting that they are not pinned to structural defects in the crystal. Figure 6.6 shows

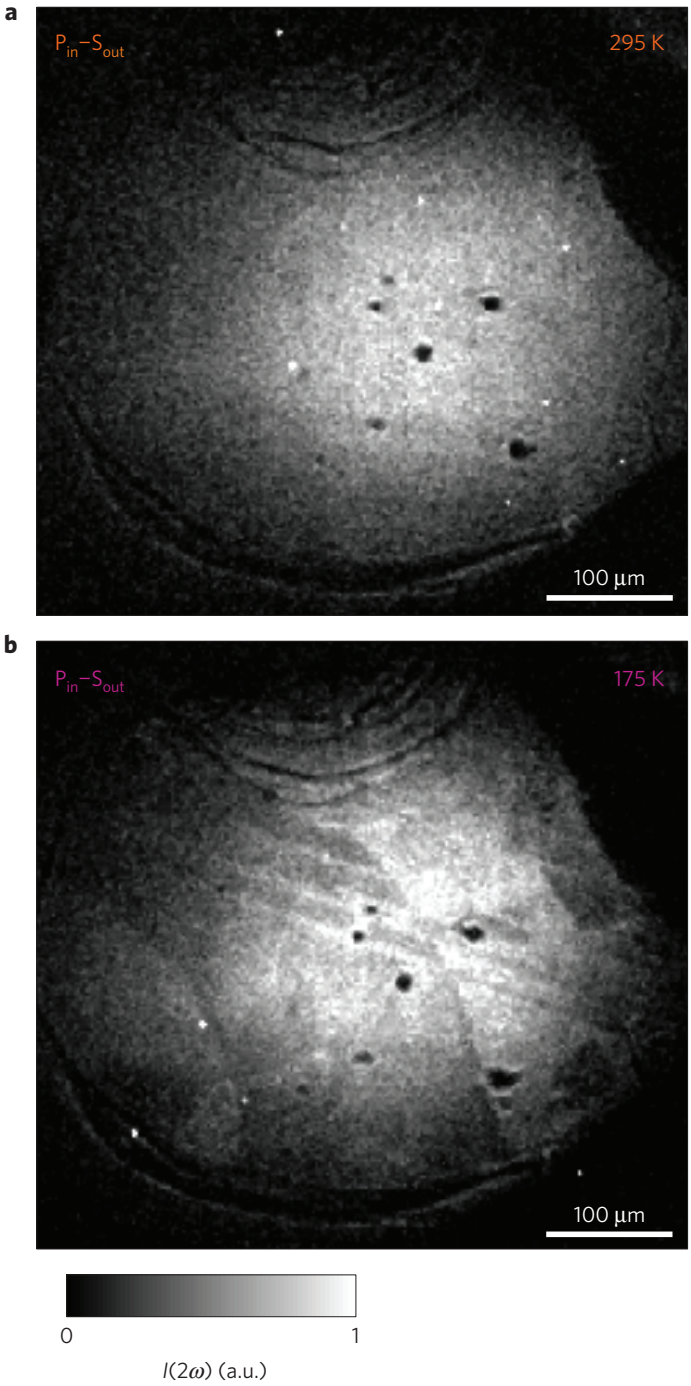

Figure 6.7: **Domains of the hidden order phase revealed by SHG images**. **(a)** SHG image at 295 K shows uniform intensity across the sample surface consistent with a single crystalline domain. **(b)** SHG image at 175 K reveals domains of higher and lower intensities corresponding to different configurations of the loop current pseudovector.

four types of domains from an extensive survey of SHG-RA patterns in different regions of the sample surface. These SHG-RA patterns are 0°, 90°, 180° and 270°-rotated copies of those in Fig. 6.5, and represent the four 90°-rotated directions of the loop current pseudovector. Although other microscopic models that obey the same set of symmetries cannot be ruled out, our observation of the four types of symmetry-broken domains is consistent with the hidden order being the magneto-electric loop-current order.

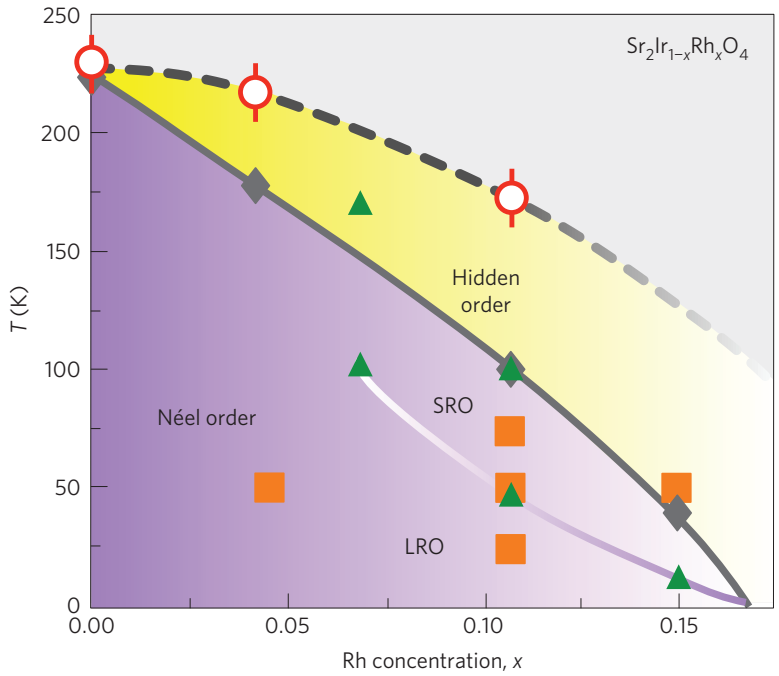

Figure 6.8: **Temperature and hole-doping phase diagram of the hidden order**. Red open circle denotes the hidden order onset temperature, T_Ω, determined from SHG experiment with error bar indicated. Black filled diamond denotes T_N from d.c. magnetic susceptibility measurement. Green filled triangle denotes T_N from resonant X-ray diffraction [59]. Orange filled square denotes pseudogap region from ARPES [60].

Additional insight for the nature of this hidden order comes from a temperature-doping phase diagram of the hidden order phase. To do so, we determine the ordering temperature T_Ω of the hidden phase for a series of hole-doped $Sr_2Ir_{1-x}Rh_xO_4$ crystals, in which the long-range antiferromagnetic order is increasingly suppressed with doping. T_Ω is determined by the onset of the increase in SHG intensity in the symmetry-broken direction of P_{in}-S_{out} polarization channel. In parent Sr_2IrO_4, T_Ω is found to be 232 K, close to but slightly higher than $T_N \sim 230$ K as determined by d.c. magnetic susceptibility measurements. In $Sr_2Ir_{1-x}Rh_xO_4$, T_Ω and T_N be-

come increasingly separated as x increases [Fig. 6.8]. This indicates that the Néel order and the hidden order are not trivially tied, but are independent and distinct electronic phases. In fact, in a Landau free energy expansion, a bilinear coupling between the antiferromagnetic Néel and hidden order parameters is forbidden by symmetry, so there is no *apriori* reason that the two orders should couple or coincide. The close proximity of T_Ω and T_N observed in parent Sr_2IrO_4 suggests some microscopic mechanism by which one order can induce the other through a biquadratic coupling: for example, an enhancement of the superexchange coupling between $J_{eff} = 1/2$ moments due to the presence of hidden order. As long range antiferromagnetism is suppressed by hole doping, fluctuations in the hidden order is less likely to affect the ordering of the $J_{eff} = 1/2$ moments, hence the increasing separation between T_Ω and T_N at higher hole dopings.

Our finding of a hidden symmetry-broken phase in proximity to an antiferromagnetic Mott insulator reveals a striking parallel between the cuprate and Sr_2IrO_4 phase diagrams, which is further strengthened by recent observations of a pseudogap region in $Sr_2Ir_{1-x}Rh_xO_4$ using angle-resolved photoemission spectroscopy [60]. Driving the hidden phase to a quantum critical point [84] through higher doping may be a route to achieving high-T_c [85] or parity-odd [86, 87] superconductivity in the iridates. Although further theoretical studies are required to establish the microscopic origin of the hidden phase, the fact that it bears the symmetries of a magneto-electric loop-current order already suggests several interesting macroscopic responses, including a linear magneto-electric effect [79] and non-reciprocal optical rotation [79, 88] .

Chapter 7

Charge-density-wave-like instability in $(Sr_{1-x}La_x)_3Ir_2O_7$ revealed by time-resolved optical reflectivity

7.1 Introduction

Similar to the single-layer Sr_2IrO_4, $Sr_3Ir_2O_7$ is also a spin-orbit-assisted Mott insulator. Its ground state is an antiferromagnetic insulator with a charge gap Δ of order 100 meV, as determined by optical conductivity [89], scanning tunnelling microscopy (STM) [90] and angle-resolved photoemission spectroscopy (ARPES) [91] measurements. However, $Sr_3Ir_2O_7$ does not adhere to the strict description of a Mott insulator, where the insulating gap is opened by Coulomb interaction, a case distinct from a Slater insulator where the insulating gap is opened by the antiferromagnetic order. There is evidence from transport [92], optical conductivity [89] and ARPES [93] studies that the electronic density of states (DOS) near the Fermi level changes in the vicinity of the antiferromagnetic transition ($T_N \sim 280$ K) in $Sr_3Ir_2O_7$. Moreover, resonant inelastic X-ray scattering experiments [94] [95] show that the energy scale of magnetic exchange is comparable to Δ, raising questions about the insulating nature of $Sr_3Ir_2O_7$.

In addition, unlike the rich electronic phases that have been observed for electron and hole-doped Sr_2IrO_4, no electronic instability similar to those in cuprate high-T_c superconductors has been observed in doped $Sr_3Ir_2O_7$. Electron-doped $(Sr_{1-x}La_x)_3Ir_2O_7$ induces an insulator-to-metal transition with simultaneous suppression of long-range antiferromagnetism [96]. In addition, a structural phase transition at low temperature with both La- and Ca-substitutions is also observed. Other than these, there has been no report of collective electronic phenomena in electron-doped $Sr_3Ir_2O_7$. In order to better understand the insulating nature of $Sr_3Ir_2O_7$ and scrutinize electron-doped $Sr_3Ir_2O_7$ for electronic instabilities, we put it to the test of time-resolved optical reflectivity, which is sensitive to small change of electronic structure near Fermi energy even at elevated temperatures.

7.2 Experiment and results

In time-resolved optical reflectivity experiment, a pump pulse promotes electrons from the valence band to the conduction band, and a probe pulse monitors the subsequent recombination of the electron-hole pairs. In the case of an insulator,

small changes of the electronic structure across the gap can dramatically affect the electron-hole (e-h) recombination, which in turn manifests in time-resolved optical reflectivity. We apply this technique to $Sr_3Ir_2O_7$ first to identify the relationship between the insulating gap and the antiferromagnetic order.

Figure 7.1(a) shows the reflectivity transients of $Sr_3Ir_2O_7$ measured with a pump and probe photon energy of 1.55 eV across the Néel temperature (T_N). At all temperatures, pump excitation causes an abrupt drop in reflectivity followed by a slower recovery on the picosecond timescale. Around T_N, both the magnitude of the drop and the recovery time become strongly temperature dependent. To understand the temperature dependence in greater detail, the individual reflectivity transients are fitted to an exponential decay function $\Delta R/R = Ae^{t/\tau} + C$, where A is the amplitude of the reflectivity drop at t = 0, τ is the characteristic photo-carrier relaxation time and C describes much slower equilibration processes such as heat diffusion. Figure 7.1(b) shows that upon heating towards T_N, A declines sharply in magnitude while τ exhibits a divergent behaviour, both of which are consistent with the insulating gap closing at T_N. Microscopically, this can be understood using the phenomenological Rothwarf-Taylor model [63], where A is treated as being representative of the fractional change in the number of e-h pairs introduced by the pump pulse and τ is the characteristic time for the population of such pairs to decay. Recombination of an e-h pair across the gap is accompanied by the emission of a phonon with energy greater than or equal to Δ. Since these phonons can in turn excite additional e-h pairs, τ is ultimately determined by the time required for these phonons to anharmonically decay into phonons of energy less than Δ or to escape from the probed region. As the gap closes upon approaching T_N, more thermally populated low-energy phonons become available for e-h pair production, impeding the recombination of photo-excited e-h pairs and reducing their ratio to thermally excited e-h pairs, which respectively cause τ to diverge and A to drop precipitously. In the limit where the ratio of photo-excited to thermally excited e-h pairs is small, analytical expressions can be derived [62] for the temperature dependence of both A and τ, assuming a Bardeen-Cooper-Schrieffer (BCS)-like temperature dependence of the gap below T_N, which fit the data remarkably well, as shown in Fig. 7.1(b). These results confirm that the insulating state of $Sr_3Ir_2O_7$ is only marginally stable and that the insulating gap closes concurrently with the loss of antiferromagnetic long-range order, which differs from the strongly correlated Mott state realized in cuprates [97]. The fact that no drastic changes in band structure are observed across T_N by ARPES [93] and optical conductivity [89] measurements suggests that the

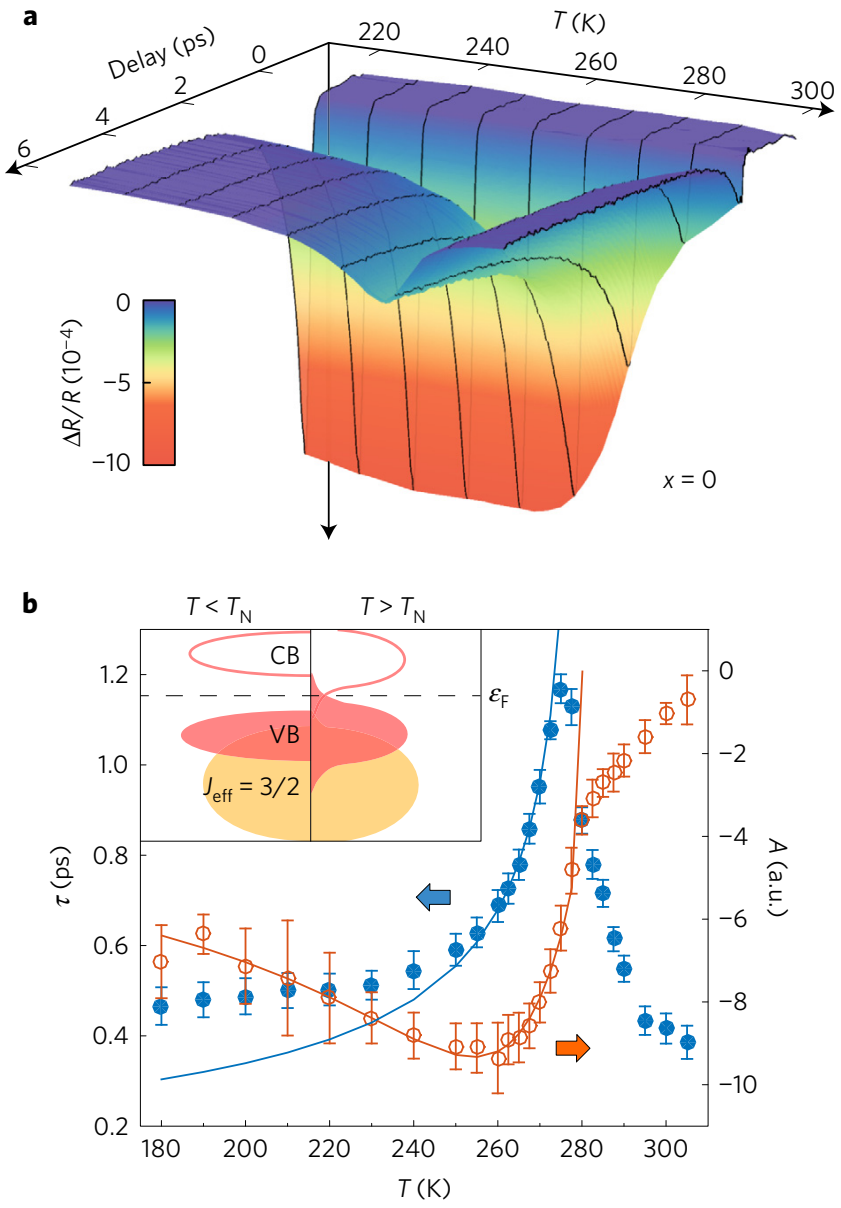

Figure 7.1: **Temperature-dependent reflectivity transients of $Sr_3Ir_2O_7$ (x = 0).** **a**, Three-dimensional surface plot of the transient reflectivity as a function of temperature and delay measured using a pump fluence of 80 μJcm^{-2}. Black lines are raw traces at select temperatures. Pronounced changes are observed around $T_N \sim$ 280 K. **b**, Temperature dependence of the amplitude A (open orange circles) and decay time τ (filled blue circles) of the reflectivity transients extracted from fits to the single exponential decay function. The superposed orange and blue curves are best fits to the Rothwarf-Taylor model described in the main text. The inset depicts the transfer of spectral weight into the insulating gap above T_N while the J_{eff} = 1/2 valence band (VB) and conduction band (CB) remain intact.

gap closure in $Sr_3Ir_2O_7$ occurs primarily through the transfer of high-energy spectral weight into the gap (Fig. 7.1(b) inset) and is concentrated at momentum values near the X points of the Brillouin zone, as shown by ARPES [93].

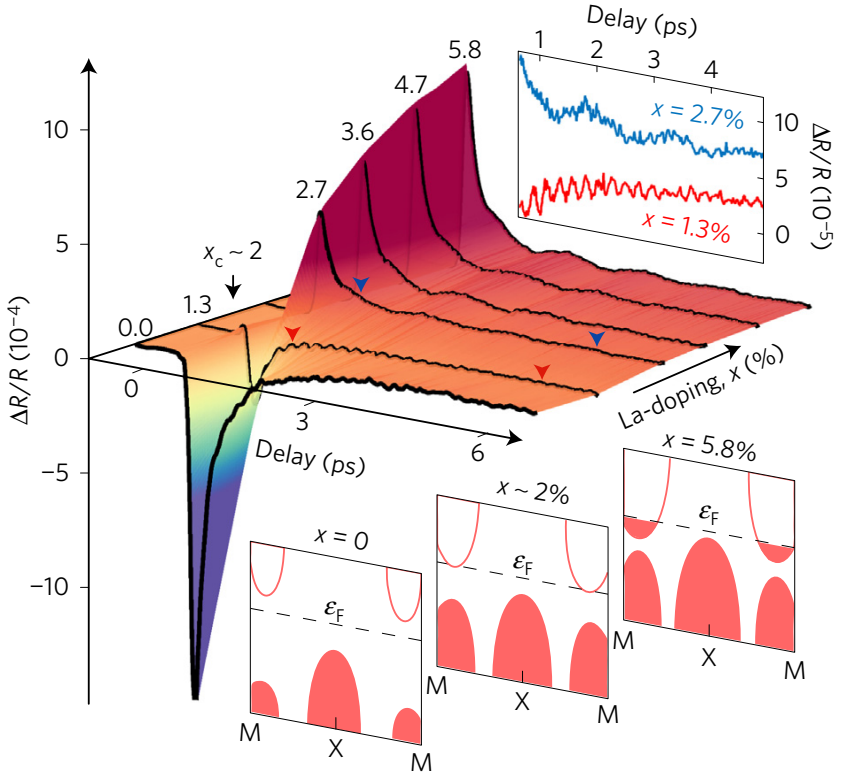

Figure 7.2: **Doping-dependent reflectivity transients of $(Sr_{1-x}La_x)_3Ir_2O_7$.** Three-dimensional surface plot of the transient reflectivity as a function of La doping (x) and delay. Black lines are the raw traces of the x = 0, 1.3, 2.7, 3.6, 4.7 and 5.8% doped samples. All traces were measured at 120 K using a pump fluence of 140 μJcm^{-2} . The top inset shows a magnified view of the delay range bounded by the coloured triangles in the main figure, showing the high-frequency coherent A_{1g} phonon mode and the low-frequency electronic mode observed in the x = 1.3% and x = 2.7% samples, respectively. The evolution of the band structure across the insulator-to-metal transition ($x_c \sim 2\%$) along the M-X-M momentum space cut as determined by ARPES [98, 99] is illustrated schematically below the data.

It has recently been shown that electron doping $Sr_3Ir_2O_7$ by substituting Sr with La can also suppress antiferromagnetism and force the insulating gap to close [96, 98–100]. However, unlike in the thermally driven case (Fig. 7.1), ARPES studies have shown that doping across the critical value of x in $(Sr_{1-x}La_x)_3Ir_2O_7$, which is on the level of a few percent, causes a discontinuous shift of the band edges and the formation of electron pockets around the M points of the Brillouin zone [98,

99]. The contrast between these two mechanisms of gap closing is highly apparent from ultrafast optical reflectivity data. As shown in Fig. 7.2, the doping-induced gap closing across $x_c \sim 0.02$ (2%) is manifested as a change in sign of ΔR/R, which is consistent with an insulator-to-metal transition that is realized by a collective electronic rearrangement [101]. Interestingly, across $x_c \sim 2\%$, an abrupt change is also observed in the collective excitations of the system. For $x < 2\%$, we observe a high-frequency modulation superposed on top of the exponential decay (Fig. 7.2 inset), which arises from coherent oscillations of a 4.4 THz A_{1g} phonon mode that has also been observed by Raman scattering in $Sr_3Ir_2O_7$ [102]. For all $x > 2\%$ on the other hand, an additional low-frequency ($\sim$ 1 THz) modulation is present (Fig. 7.2 inset) that does not correspond to any reported Raman active phonon mode. Unlike the A_{1g} phonon mode, which diminishes in amplitude upon entering the metallic regime (probably due to screening by free carriers), this mode appears only in the metallic regime, suggesting an electronic origin.

To understand the origin of this low-frequency mode, we studied its detailed temperature dependence. Figure 7.3(a) shows the temperature evolution of the reflectivity transients obtained from the most metallic sample ($x \sim 5.8\%$) available. At low temperatures, both the low-frequency mode and the A_{1g} phonon mode are clearly resolved in both the raw data and its Fourier transform (Fig. 7.3(a) inset). As the temperature increases, the frequency and the amplitude of the low-frequency mode continuously decrease until the mode is no longer resolvable near 200 K. To extract quantitative information from this data, we fit the oscillatory component of the reflectivity transients to a damped sinusoid of the form $A_{DW}e^{-\Gamma t}\sin(2\pi t/\tau_{DW} + \phi)$, where A_{DW}, Γ and τ_{DW} are the amplitude, damping rate and period of the low-frequency mode, respectively, and ϕ is a phase offset. Figure 7.3(b) shows that A_{DW} exhibits an order-parameter-like onset below a critical temperature $T_{DW} \sim$ 210 K and Fig. 7.3(c) shows that both Γ and τ_{DW} diverge upon approaching T_{DW}, indicating a softening of the mode to zero energy. These behaviours are consistent with coherent amplitude oscillations of an electronic order parameter that develops via a continuous phase transition below T_{DW}. In particular, they are highly reminiscent of the coherent charge density wave amplitudons that have previously been observed by time-resolved optical reflectivity in systems such as $K_{0.3}MoO_3$ [103] or the underdoped cuprates [3, 104].

A recent neutron diffraction experiment found evidence of a weak intra-unit-cell structural distortion in metallic $(Sr_{1-x}La_x)_3Ir_2O_7$ crystals below a critical tempera-

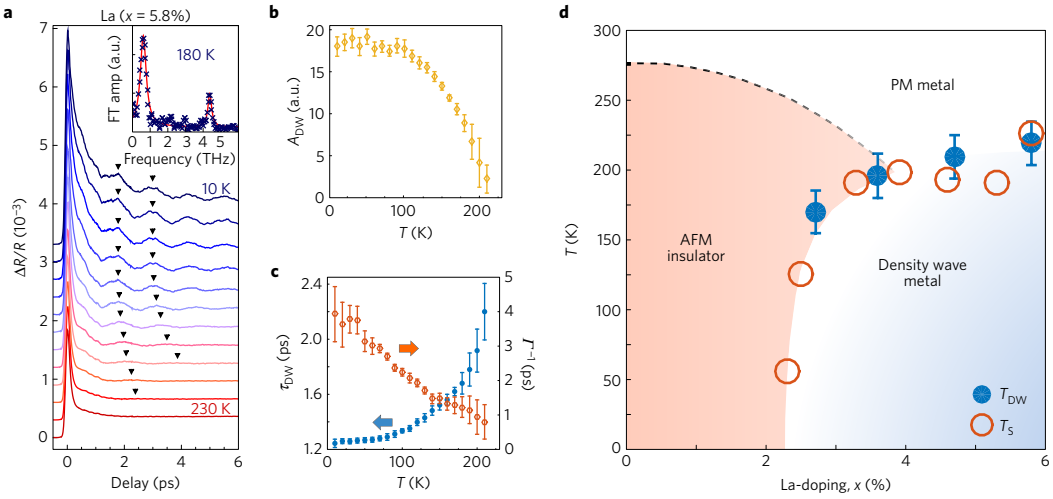

Figure 7.3: **Coherent oscillations of an electronic order parameter. a**, Reflectivity transients of 5.8% La doped $Sr_3Ir_2O_7$ plotted for a series of temperatures separated by 20 K. The traces are vertically offset for clarity. A higher pump fluence of 400 μJcm^{-2} was used to better visualize the weak temporal modulations but they are present even at lower fluences (see Fig. 7.2). Two of the modulation peaks are marked with triangles to guide the eye. The Fourier transform of the background-subtracted reflectivity transient measured at 180 K is shown in the inset. The red line is a best fit to the sum of two Lorentzian functions and a constant background. **b**,**c**, Temperature dependence of the oscillation amplitude (A_{DW}), and period (τ_{DW}) and damping time (Γ^{-1}), respectively, extracted from fits to a damped sinusoidal function described in the main text. Error bars represent the 95% confidence intervals of the fitted values. **d**, Temperature versus doping phase diagram of $(Sr_{1-x}La_x)_3Ir_2O_7$. The paramagnetic (PM) to antiferromagnetic (AFM) phase boundary and the line of structural phase transitions (T_S) are based on data from ref [96], whereas the line of density wave phase transitions (T_{DW}) is based on time-resolved optical reflectivity data. Error bars denote the uncertainty in T_{DW} estimated by extrapolating to the temperature at which A_{DW} goes to zero.

ture T_S that is also of order 200 K [96]. No new spatial periodicity was reported below T_S, which is consistent with the absence of additional superlattice modulations and band folding in low-temperature STM [96] and ARPES [98, 99] data on $(Sr_{1-x}La_x)_3Ir_2O_7$, respectively. On the basis of the observations that the structural distortion emerges upon very light La doping, appears to compete with antiferromagnetic ordering and is suppressed in temperature by isovalent substitution of Sr^{2+} by Ca^{2+}, it was suggested that there is a strong electronic contribution to the lattice distortion that enhances T_S [96]. By carrying out transient reflectivity measurements analogous to Fig. 7.3(a)-(c) for a series of different La doping levels, we identified the region of the temperature versus doping phase diagram over which

our observed electronic order exists [Fig. 7.3(d)]. Remarkably, its phase boundary coincides well with that of the structural transition, reaffirming a cooperative interaction between the structural and electronic order parameters.

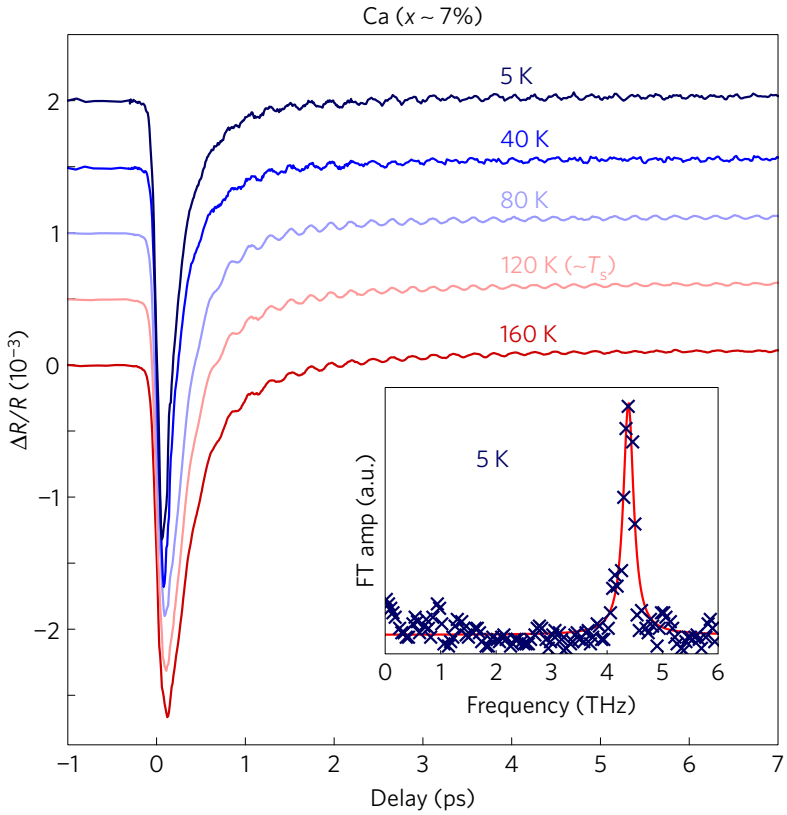

Figure 7.4: **Reflectivity transients of insulating $(Sr_{1-x}La_x)_3Ir_2O_7$.** Transient reflectivity of ~ 7% Ca substituted $Sr_3Ir_2O_7$ plotted over a range of temperatures spanning its structural transition temperature T_S ~ 120 K. The traces are vertically offset for clarity. The A_{1g} phonon oscillations are clearly resolved in both the raw data and Fourier transform (inset), but the electronic mode is absent. The red line in the inset is a best fit to the sum of a Lorentzian function and a constant background.

To confirm that the low-frequency oscillations observed in $(Sr_{1-x}La_x)_3Ir_2O_7$ originate from a Fermi surface instability and not simply from the structural distortion below T_S, we performed time-resolved optical reflectivity measurements on isovalent substituted $(Sr_{1-x}Ca_x)_3Ir_2O_7$, which remains insulating like $Sr_3Ir_2O_7$ but undergoes the same structural distortion as that observed in metallic $(Sr_{1-x}La_x)_3Ir_2O_7$, albeit at considerably lower temperature. Figure 7.4 shows the reflectivity transients of $(Sr_{0.93}Ca_{0.07})_3Ir_2O_7$ taken both above and below its structural transition temperature (T_S ~ 120 K). The A_{1g} phonon mode at 4.4 THz is again observed and does not undergo any measurable shift across T_S. However, the low-frequency mode that

was observed in metallic $(Sr_{1-x}La_x)_3Ir_2O_7$ is clearly absent both in the raw data and its Fourier transform (Fig. 7.4 inset), thus precluding a purely structural origin of the mode.

No static long-range magnetic order has been observed by neutron or resonant X-ray diffraction, or magnetic susceptibility measurements in metallic $(Sr_{1-x}La_x)_3Ir_2O_7$ crystals [96]. In addition, we have performed resonant inelastic X-ray scattering measurements [105] that show both quasi two-dimensional magnon modes and exciton-like spin-orbital entangled modes in $(Sr_{1-x}La_x)_3Ir_2O_7$ to exist only at frequencies far above 1 THz. These observations rule out any spin-related instabilities at the 1 THz energy scale and instead point towards a charge density wave-like instability as being responsible for the low-energy mode. However, this interpretation must be reconciled with the absence of any signatures of a new spatial periodicity below T_{DW} in other experiments. One possibility is that the charge density wave order is very short-ranged like in the case of under-doped cuprates [3, 104], or even temporally fluctuating, which would naturally explain the strong damping of its collective modes [Fig. 7.3(c)] in comparison to those in static long-range ordered charge density wave systems such as $K_{0.3}MoO_3$ [103]. Although a detailed microscopic understanding of this density wave instability in $(Sr_{1-x}La_x)_3Ir_2O_7$ will require more extensive theory and experiments, our work shows generally that iridates in the weak Mott limit can also support interesting electronic instabilities, possibly realizing strongly spin-orbit coupled analogues of those found in their lighter transition metal oxide counterparts.

Chapter 8

Second harmonic generation investigations of antiferromagnetic orders in MPX_3

8.1 Introduction

Since the first successful exfoliation of graphene [106, 107], which is a semimetal, the family of 2D van der Waals (vdW) materials has quickly expanded to include spin-valley coupled semiconductors [108, 109], Ising superconductor [110, 111], and charge-density-wave material [112]. Adding to the list is the quest for materials that exhibit long range magnetic order in the 2D limit, which is thought to be highly suppressed by thermal fluctuations [113]. MPX_3, with transition metal M and chalcogen X = {S, Se, Te}, are honeycomb-structured layered vdW materials that exhibit magnetism. They are exfoliable materials to test the Mermin-Wagner theorem for magnetism in the 2D limit. Recently, long ranger ferromagnetism was verified by magneto-optical Kerr microscopy in monolayer CrI_3 [114] and bilayer $CrGeTe_3$ [115]. Similarly, long range antiferromagnetic stripe order has also been verified by scanning Raman spectroscopy in monolayer $FePS_3$ [116], where the stripe order doubles the unit cell and leads to the appearance of additional Raman peaks below T_N.

Unlike the antiferromagnetic stripe order in $NiPS_3$ and $FePS_3$, Néel-type antiferromagnetic order exists in $MnPS_3$ [117–120]. Magnetic susceptibility measurements and spin wave model calculations found that the exchange interaction in $MnPS_3$ is Heisenberg-like [120, 121], whereas $NiPS_3$ is better described by the XY model [120] and $FePS_3$ by the Ising model [120, 122]. Whether the Heisenberg antiferromagnet survives to the monolayer limit is a question to be answered by experiments. This also has implication for a recent proposal of spin-valley coupling in monolayer antiferromagnetic $MnPS_3$ which can lead to circular dichroic hall effect and topological edge states at the antiferromagnetic domain walls [123]. However, magneto-optical Kerr effect is not sensitive to collinear antiferromagnetism. Moreover, Néel order preserves the unit cell of $MnPS_3$, therefore it does not fold the Brillouin zone and introduce new Ramon mode to a Raman scattering experiment. A microscopic probe that is sensitive to the Néel transition on a honeycomb lattice therefore has to be found. Fortunately, due to the inequivalence of the two

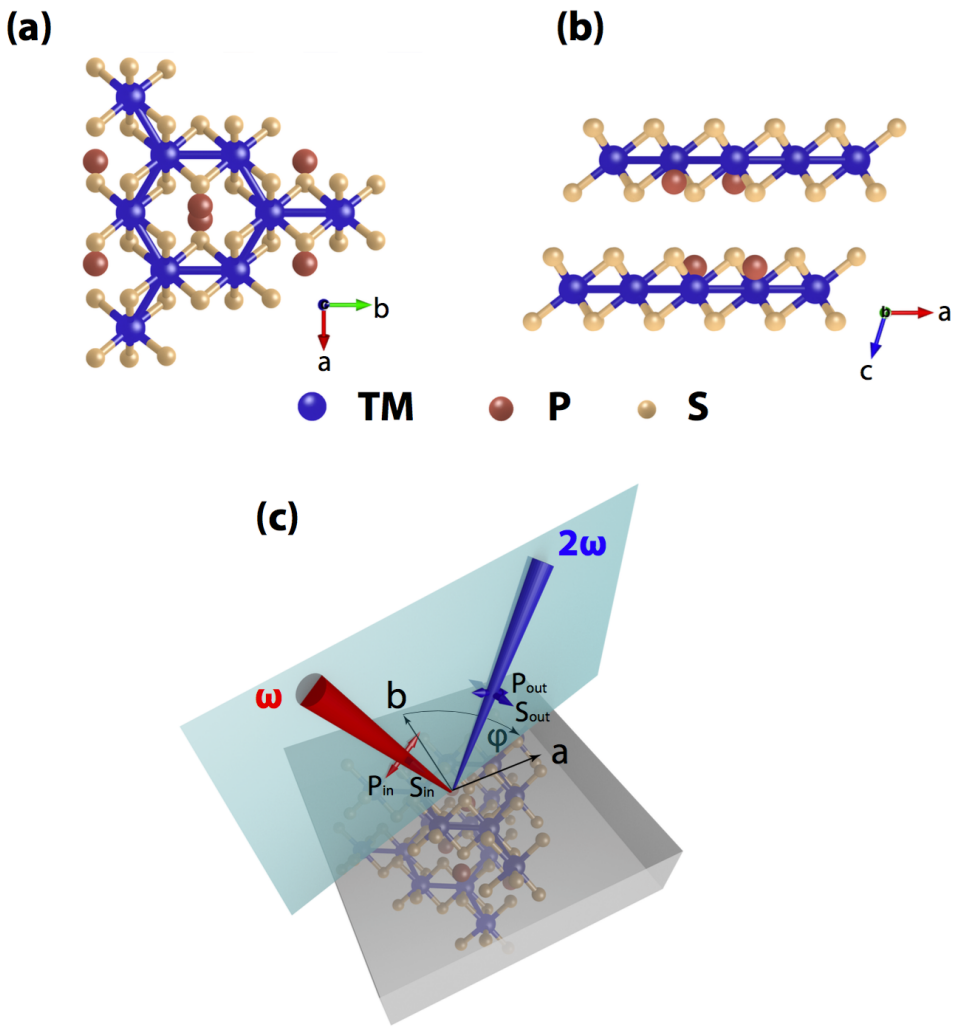

Figure 8.1: **Lattice structure of MPX_3 and SHG-RA experimental geometry.** Lattice structure of monoclinic MPX_3 looking down along **(a)** c-axis and **(b)** b-axis. The magnetic M = Mn, Fe, Ni ions are arranged in a 2D hexagonal lattice in the ab plane. Each unit cell consists of two layers of MPX_3 displaced along the a-axis. **(c)** Geometry of the SHG-RA experiment. The scattering plane is defined normal to the ab plane of MPX_3.

sublattices of a honeycomb structure, the Néel order in $MnPS_3$ necessarily breaks inversion symmetry. Second harmonic generation (SHG), which is extremely sensitive to inversion-breaking [4], and which can be easily adapted to microscopy, is therefore the perfect tool for studying the Néel order in $MnPS_3$. We apply this this technique to $MnPS_3$, $FePS_3$, and $NiPS_3$, and demonstrate that SHG very well distinguishes between the Néel order and the antiferromagnetic stripe order in these compounds. A microscopic model is offered at the end to explain how the SHG process couples to Néel order parameter but not the antiferromagnetic stripe order

parameter.

8.2 Experiment and results

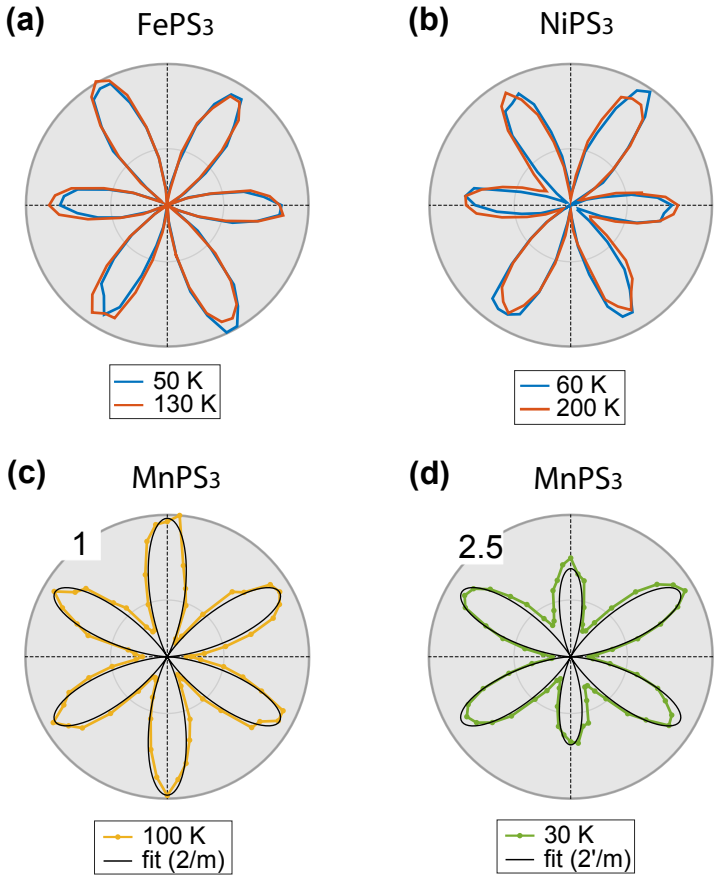

Figure 8.2: **SHG-RA patterns for MPX_3 above and below T_{AF}.** The S_{in}-S_{out} data from **(a)** $FePS_3$ **(b)** $NiPS_3$ above and below their respective T_{AF} show negligible change across T_{AF}. In contrast, in $MnPS_3$ the intensity of SHG **(d)** below T_N is much stronger compared to **(c)** above T_N. Moreover, the symmetry of the S_{in}-S_{out} pattern also changes across T_N. In (c)(d) the solid lines are best fit to the bulk electric quadrupole radiation from 2/m point group and bulk electric dipole radiation from 2′/m magnetic point group respectively. The data in (c) is normalized to the maximum intensity in (d).

The crystalline point group of MPX_3 is 2/m [124], which consists of a 2-fold rotation along the crystalline b-axis and a mirror plane perpendicular to it. Figure 8.1(a)(b) shows the crystal structure of MPX_3. The transition metal M are arranged on the vertices of a hexagon, with chalcogens on top and below forming two oppositely pointed equilateral triangles related by inversion. Different layers of MPX_3 are displaced along the crystalline a-axis. However, coupling between

the layers is weak and the structure can thought of as quasi-2D. In particular, this 2D character is manifested in second harmonic generation rotational anisotropy (SHG-RA) patterns. Figure 8.2 shows the SHG-RA patterns from $MnPS_3$, $FePS_3$ and $NiPS_3$ from the S_{in}-S_{out} polarization channel, which all exhibit close to six-fold rotational symmetry in intensity above T_{AF}. Since 2/m is centrosymmetric, bulk electric dipole contribution to SHG is forbidden by symmetry. Instead, the S_{in}-S_{out} patterns can be explained in terms of either surface electric dipole (ED) contribution $P_i(2\omega) = \chi^{ED}_{ijk} E_j(\omega) E_k(\omega)$ or bulk electric quadrupole (QD) contribution $P_i(2\omega) = \chi^{QD}_{ijkl} E_j(\omega) \nabla_k E_l(\omega)$. In both cases, the sign of $P_i(2\omega)$ alternates between adjacent peaks. Hence the S_{in}-S_{out} intensity data, which is proportional to $|P_i(2\omega)|^2$, in fact implies three-fold rotational symmetry. This is the correct rotational symmetry of a single MPX_3 plane.

The magnetic interactions in MPX_3 are frustrated by competing first, second and third nearest neighbor exchange interactions $\{J_1, J_2, J_3\}$. The magnetic ground state of MPX_3 ranges from in-plane ferromagnetic to Néel, and to antiferromagnetic stripe order, with ferro- or antiferromagnetic inter-plane couplings. Due to the high level of frustration, it was proposed that both mechanical stress and carrier doping can switch the magnetic order from one to another [125, 126]. Figure 8.3 shows the magnetic structures of the three materials in our study. $MnPS_3$ undergoes an in-plane Néel transition at 78 K. $FePS_3$ exhibits an in-plane antiferromagnetic stripe order that is antiferromagnetically coupled between the planes below 123 K. $NiPS_3$ also an exhibits in-plane antiferromagnetic stripe order which is however ferromagnetically coupled between the planes below 155 K. While the in-plane Néel order breaks inversion in $MnPS_3$, both forms of stripe order in $FePS_3$ and $NiPS_3$ preserve inversion: inversion plus a translation by lattice constants reproduces the same stripe order [Fig. 8.3]. Since bulk ED radiation, the strongest contribution to SHG, is only allowed in non-centrosymmetric media, we expect SHG to be greatly enhanced below T_N in $MnPS_3$.

Figure 8.2 shows that while the change in the SHG-RA patterns for $FePS_3$ and $NiPS_3$ across T_{AF} is small, in $MnPS_3$ there is indeed a dramatic increase in SHG intensity below T_N, signifying bulk ED contribution. In addition, the three-fold rotational symmetry inferred from the S_{in}-S_{out} pattern above T_N is reduced to one-fold below T_N. A recent neutron polarimetry study on $MnPS_3$ found that in the Néel phase, the magnetic moments are oriented at a finite angle $\sim 8^\circ$ from the c^* axis ($\hat{c}^* \equiv \hat{a} \times \hat{b}$) [124]. This projects a finite moment in the ab plane, which breaks

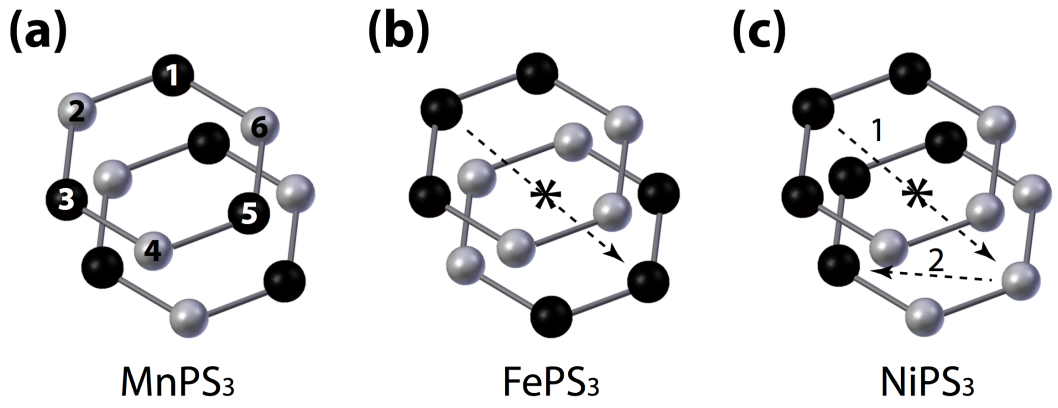

Figure 8.3: **Magnetic structures of MPX_3. (a)** Below 78 K, $MnPS_3$ develops in-plane Néel order which breaks inversion symmetry due to the inequivalence of the two sublattices of a honeycomb lattice. **(b)** Below 123 K, $FePS_3$ develops in-plane antiferromagnetic stripe order. Between the planes the coupling is antiferromagnetic. Dashed arrow denotes the symmetry operation (inversion through the center *) which maps the magnetic structure onto itself. **(c)** Below 155 K, $NiPS_3$ also develops in-plane antiferromagnetic stripe order, with ferromagnetic coupling across the planes. Inversion (1) plus lattice translation (2) maps the magnetic structure onto itself.

the three-fold rotational symmetry of the paramagnetic phase and gives rise to the observed one-fold rotational symmetry. The low temperature SHG-RA pattern can be fitted to the bulk ED contribution from the $2'/m$ magnetic point group, to which the antiferromagnetic structure of $MnPS_3$ belongs to.

To investigate the Néel order in $MnPS_3$ more systematically, we measure the intensity of peaks in the S_{in}-S_{out} pattern as a function of temperature. Figure 8.4(a) shows the temperature dependence of the SHG peak intensity. In $MnPS_3$, the SHG intensity has a power dependence on temperature from which we can extract $\chi(T) \propto (T_N - T)^{\beta}$ with $\beta = 0.2$ because SHG intensity is proportional to $|\chi|^2$. In contrast, in $FePS_3$, χ shows negligible temperature dependence. While a macroscopic consideration based on symmetry alone can explain the change in SHG intensity, below we propose a microscopic theory based on a model developed for Cr_2O_3 [127] to explain why SHG couples to the Néel order parameter in $MnPS_3$ but not the antiferromagnetic stripe order parameter in $FePS_3$.

SHG involves a two-photon absorption process and a single-photon emission process. Based on optical absorption studies on $MnPS_3$, the two-photon absorption process in our SHG experiment using 1.5 eV incoming light corresponds to the $^6A_{1g}(^6S) \rightarrow {}^4T_{2g}(^4D)$ intra-ionic d-d transition in Mn^{2+} [128, 129]. Although the

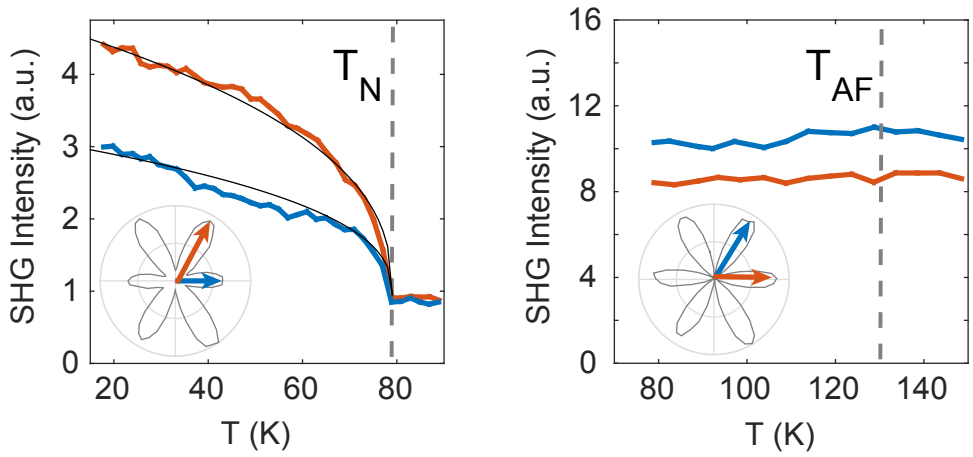

Figure 8.4: **Temperature dependence of SHG intensity for $MnPS_3$ and $FePS_3$.** The temperature dependence of SHG intensity for **(a)** $MnPS_3$ and **(b)** $FePS_3$ across their respective T_{AF} = 78 K and 127 K. The orange and blue curves correspond to the temperature dependence of different peaks marked in the insets. The solid lines in **(a)** are best simultaneous fit of the two sets of data to $I(T) = A(T_N - T)^{2\beta}$ plus a constant offset, with $\beta = 0.2$.

absorption edge in $MnPS_3$, which corresponds to P^{4+}, $S^{2-} \rightarrow Mn^{2+}$ charge transfer, is also close to 3 eV, it moves to higher energy at lower temperature [128, 130]. As such, any two-photon absorption due to this transition is suppressed at low temperature, impeding the SHG process. In contrast, the $^6A_{1g}(^6S) \rightarrow {}^4T_{2g}(^4D)$ transition is insensitive to temperature change, and hence more likely to account for the absorption process of SHG. In addition to this assumption, we assume moderate spin-orbit coupling as well as a small local polar distortion of the Mn^{2+} ionic potential, which has recently been suggested to occur in $MnPS_3$ [131] to explain its magnetoelectric effect [124].

First of all, spin-orbit coupling, which is weak although finite in $3d$ transtion metal, mixes the t_{2g} and e_g states of Mn. For the toy model, we consider its effect on the d_{xy} and $d_{x^2-y^2}$ states:

$$\left\langle d_{xy}, m_s \middle| \mathbf{L} \cdot \mathbf{S} \middle| d_{x^2-y^2}, m_s \right\rangle = 2\mathrm{i} \langle S_z \rangle$$

where $\langle S_z \rangle \equiv \langle m_s | S_z | m_s \rangle$. On the other hand, the inversion symmetry of the Mn^{2+} ionic potential is broken by its nearest Mn^{2+} neigbhours as well as a trigonal distortion of the sulphur octahedron around it. This mixes the $3d$ and $4p$ states [132] of Mn^{2+}. Treating both spin-orbit interaction and local polar distortion as small

perturbations, the new ionic eigenstates for Mn^{2+} can be written as

$$\left|\tilde{d}_{xy}\right\rangle = \left|d_{xy}, m_s\right\rangle + \lambda \langle S_z\rangle \left|d_{x^2-y^2}, m_s\right\rangle + \eta \left|p, m_s\right\rangle$$
$$\left|\tilde{d}_{x^2-y^2}\right\rangle = \left|d_{x^2-y^2}, m_s\right\rangle - \lambda \langle S_z\rangle \left|d_{xy}, m_s\right\rangle + \eta' \left|p', m_s\right\rangle$$

where λ denotes the spin-orbit coupling strength, η, η' are proportional to the local parity-breaking molecular field, and $|p, m_s\rangle$, $|p', m_s\rangle$ are Mn $4p$ orbitals.

Assuming $\left|d_{xy}\right\rangle$ and $\left|d_{x^2-y^2}\right\rangle$ are the initial and final states of the two-photon absorption process, the SHG process in the ED channel can be written as

$$\sum_{\alpha} \left\langle \tilde{d}_{xy}\middle|\mathbf{r}\middle|\tilde{d}_{x^2-y^2}\right\rangle \left\langle \tilde{d}_{x^2-y^2}\middle|\mathbf{r}\middle|\alpha\right\rangle \left\langle \alpha\middle|\mathbf{r}\middle|\tilde{d}_{xy}\right\rangle$$

where $|\alpha\rangle$ denotes intermediate state. The leading contribution in the expansion is proportional to $\lambda^0\eta^0$. It comprises terms involving only the unperturbed $3d$ states: $\left\langle d_{xy}\middle|\mathbf{r}\middle|d_{x^2-y^2}\right\rangle \left\langle d_{x^2-y^2}\middle|\mathbf{r}\middle|\alpha\right\rangle \left\langle \alpha\middle|\mathbf{r}\middle|d_{xy}\right\rangle$. However, since d orbitals are parity-even, the integrand is odd and the integral vanishes. The next leading contribution is proportional to either $\lambda^1\eta^0$ or $\lambda^0\eta^1$. The contribution proportional to $\lambda^1\eta^0$ vanishes too because it comprises terms similar to those in $\lambda^0\eta^0$, except for a coefficient of $\lambda\langle S_z\rangle$ in front. The contribution proportional to $\lambda^0\eta^1$ also vanishes when summing over the unit cell because neighbouring Mn are related by inversion and hence the local polar distortion η switches sign between them [Fig. 8.3]. The leading contribution to the ED radiation is then proportional to $\lambda^1\eta^1$. In other words, it is proportional to

$$\sum_i \lambda\eta_i \langle S_z\rangle_i = \lambda\eta\Big(\langle S_z\rangle_1 - \langle S_z\rangle_2 + \langle S_z\rangle_3 - \langle S_z\rangle_4 + \langle S_z\rangle_5 - \langle S_z\rangle_6 \Big)$$

where the term in parenthesis defines the order parameter of the Néel order in $MnPS_3$. Since the antiferromagnetic stripe order parameter is $\big(\langle S_z\rangle_1 + \langle S_z\rangle_2 + \langle S_z\rangle_3 - \langle S_z\rangle_4 - \langle S_z\rangle_5 - \langle S_z\rangle_6 \big)$, it does not couple to the ED process of SHG.

In conclusion, we have demonstrated that second harmonic generation is a sensitive probe for the Néel type antiferromagnetic order in $MnPS_3$ and distinguishes it from the antiferromagnetic stripe order in $FePS_3$ and $NiPS_3$. In addition, we offered a microscopic theory to explain why SHG couples to the Néel order parameter but not the antiferromagnetic stripe order parameter in MPX_3. Our experiment paves the way towards verifying 2D long range antiferromagnetic order in $MnPS_3$. More importantly, SHG can be used in combination with other optical tools, such as magneto-optical Kerr effect, circular dichroism, to probe ultrafast magnetic phase transitions which might be realized under the Floquet picture. We now have a more complete repertoire for pursuing the future directions of 2D functional materials.

Bibliography

1. Hussey, N. Isolating the gap. *Nat. Phys.* **12,** 290–291 (2016).
2. Comin, R. & Damascelli, A. Resonant X-Ray Scattering Studies of Charge Order in Cuprates. *Annu. Rev. Condens. Matter Phys.* **7,** 369–405 (2016).
3. Torchinsky, D. H., Mahmood, F., Bollinger, A. T., Bozovic, I. & Gedik, N. Fluctuating charge-density waves in a cuprate superconductor. *Nat. Mater.* **12,** 387–391 (2013).
4. Fiebig, M. *et al.* Second-harmonic generation as a tool for studying electronic and magnetic structures of crystals: review. *J. Opt Soc. Am. B* **22** (2005).
5. Fiebig, M. *et al.* Second harmonic generation in the centrosymmetric antiferromagnet NiO. *Phys. Rev. Lett.* **87,** 13720 (2001).
6. Pavlov, V. V. *et al.* Optical harmonic generation in magnetic garnet epitaxial films near the fundamental absorption edge. *Phys. Solid State* **45,** 662–669 (2003).
7. Ogawa, Y. *et al.* Magnetization-induced second harmonic generation in a polar ferromagnet. *Phys. Rev, Lett.* **92,** 047401 (2004).
8. Torchinsky, D. *et al.* A low temperature nonlinear optical rotational anisotropy spectrometer for the determination of crystallographic and electronic symmetries. *Phys. Rev. Sci. Instr.* **85,** 083102 (2014).
9. Cavalleri, A. *et al.* Evidence for a structurally-driven insulator-to-metal transition in VO_2: A view from the ultrafast timescale. *Phys. Rev. B* **70,** 161102(R) (2004).
10. Beaud, P. *et al.* Ultrafast structural phase transition driven by photoinduced melting of charge and orbital order. *Phys. Rev. Lett.* **103,** 155702 (2009).
11. Mitrano, M. *et al.* Possible light-induced superconductivity in K_3C_{60} at high temperature. *Nature* **530,** 461–464 (2016).
12. Hu, W. *et al.* Optically enhanced coherent transport in $YBa_2Cu_3O_{6.5}$ by ultrafast redistribution of interlayer coupling. *Nature Materials* **13,** 705–711 (2014).
13. Friedt, O. *et al.* Structural and magnetic aspects of the metal-insulator transition in $Ca_{2-x}Sr_xRuO_4$. *Phys. Rev. B* **63,** 174432 (2001).
14. Mizokawa, T. *et al.* Spin-orbit coupling in the Mott insulator Ca_2RuO_4. *Phys. Rev. Lett.* **87,** 077202 (2001).
15. Lee, J. S. *et al.* Electron and crbital correlations in $Ca_{2-x}Sr_xRuO_4$ probed by optical spectroscopy. *Phys. Rev. Lett.* **89,** 257402 (2002).

16. Jung, J. H. *et al.* Change of electronic structure in Ca_2RuO_4 induced by orbital ordering. *Phys. Rev. Lett.* **91,** 056403 (2003).

17. Mizokawa, T. *et al.* Orbital state and metal-insulator transition in $Ca_{2-x}Sr_xRuO_4$ (x=0.0 and 0.09) studied by x-ray absorption spectroscopy. *Phys. Rev. B* **69,** 132410 (2004).

18. Kubota, M. *et al.* Ferro-type orbital state in the Mott transition system $Ca_{2-x}Sr_xRuO_4$ studied by the resonant x-ray scattering interference technique. *Phys. Rev. Lett.* **95,** 026401 (2005).

19. Zegkinoglou, I. *et al.* Orbital ordering transition in Ca_2RuO_4 observed with resonant x-ray diffraction. *Phys. Rev. Lett.* **95,** 136401 (2005).

20. Anisimov, V. I. *et al.* Orbital-selective Mott-insulator transition in $Ca_{2-x}Sr_xRuO_4$. *Eur. Phys. J. B* **25,** 191 (2002).

21. Fang, Z., Nagaosa, N. & Terakura, K. Orbital-dependent phase control in $Ca_{2-x}Sr_xRuO_4$ ($0<\sim x<\sim 0.5$). *Phys. Rev. B* **69,** 045116 (2004).

22. Liebsch, A. & Ishida, H. Subband Filling and Mott Transition in $Ca_{2-x}Sr_xRuO_4$. *Phys. Rev. Lett.* **98,** 216403 (2007).

23. Gorelov, E. *et al.* Nature of the Mott Transition in Ca_2RuO_4. *Phys. Rev. Lett.* **104,** 226401 (2010).

24. Liu, G.-Q. Spin-orbit coupling induced Mott transition in $Ca_{2-x}Sr_xRuO_4$ ($0\leq x\leq 0.2$). *Phys. Rev. B* **84,** 235136 (2011).

25. Alexander, C. S. *et al.* Destruction of the Mott insulating ground state of Ca_2RuO_4 by a structural transition. *Phys. Rev. B* **60,** R8422 (1999).

26. Nakatsuji, S. & Maeno, Y. Quasi-two-dimensional Mott transition system $Ca_{2-x}Sr_xRuO_4$. *Phys. Rev. Lett.* **84,** 2666 (2000).

27. Cao, G. *et al.* Ground-state instability of the Mott insulator Ca_2RuO_4: Impact of slight La doping on the metal-insulator transition and magnetic ordering. *Phys. Rev. B* **61,** R5053(R) (2000).

28. Fukazawa, H. & Maeno, Y. Filling Control of the Mott Insulator Ca_2RuO_4. *J. Phys. Soc. Jpn.* **70,** 460 (2001).

29. Qi, T. F. *et al.* Negative Volume Thermal Expansion Via Orbital and Magnetic Orders in $Ca_2Ru_{1-x}Cr_xO_4$($0<x<0.13$). *Phys. Rev. Lett.* **105,** 177203 (2010).

30. Nakamura, F. *et al.* Electric-field-induced metal maintained by current of the Mott insulator Ca_2RuO_4. *Sci. Rep.* **3,** 2536 (2013).

31. Okazaki, R. *et al.* Current-induced gap suppression in the Mott insulator Ca_2RuO_4. *J. Phys. Soc. Jpn.* **82** (2013).

32. Nakamura, F. *et al.* From Mott insulator to ferromagnetic metal: A pressure study of Ca_2RuO_4. *Phys. Rev. B* **65,** 220402(R) (2002).

33. Steffens, P. *et al.* High-pressure diffraction studies on Ca_2RuO_4. *Phys. Rev. B* **72,** 094104 (2005).

34. Alireza, P. L. *et al.* Evidence of superconductivity on the border of quasi-2D ferromagnetism in Ca_2RuO_4 at high pressure. *J. Phys.: Condens Matter* **22,** 052202 (2010).

35. Hilton, D. J. *et al.* Enhanced photosusceptibility near Tc for the light-induced insulator-to-metal phase transition in vanadium dioxide. *Phys. Rev. Lett.* **99,** 226401 (2007).

36. Pashkin, A. *et al.* Ultrafast insulator-metal phase transition in VO_2 studied by multiterahertz spectroscopy. *Phys. Rev. B* **83,** 195120 (2011).

37. Morrison, V. R. *et al.* A photoinduced metal-like phase of monoclinic VO_2 revealed by ultrafast electron diffraction. *Science* **346,** 445 (2014).

38. Miyano, K. *et al.* Photoinduced insulator-to-metal transition in a perovskite manganite. *Phys. Rev. Lett.* **78,** 4257 (1997).

39. Rini, M. *et al.* Control of the electronic phase of a manganite by mode-selective vibrational excitation. *Nature* **449,** 72 (2007).

40. Caviglia, A. D. *et al.* Ultrafast strain engineering in complex oxide heterostructures. *Phys. Rev. Lett.* **108,** 136801 (2012).

41. Qi, T. F. *et al.* Magnetic and orbital orders coupled to negative thermal expansion in Mott insulators $Ca_2Ru_{1-x}\ M_xO_4$ (M = Mn and Fe). *Phys. Rev. B* **85,** 165143 (2012).

42. Rho, H. *et al.* Lattice dynamics and the electron-phonon interaction in Ca_2RuO_4. *Phys. Rev. B* **71,** 245121 (2005).

43. Thomsen, C *et al.* Surface generation and detection of phonons by picosecond light pulses. *Phys. Rev. B* **34,** 4129 (1986).

44. Hodak, J. H. *et al.* Spectroscopy and dynamics of nanometer-sized noble metal particles. *J. Phys. Chem. B* **102,** 6958–6967 (1998).

45. Hodak, J. *et al.* Ultrafast study of electron-phonon coupling in colloidal gold particles. *Chemical Physics Letters* **284,** 135–141 (1998).

46. Gedik, N. *et al.* Single-quasiparticle stability and quasiparticle-pair decay in $YBa_2Cu_3O_{6.5}$. *Phys. Rev. B* **70,** 014504 (2004).

47. Qazilbash, M. M. *et al.* Mott Transition in VO_2 Revealed by Infrared Spectroscopy and Nano-Imaging. *Science* **318,** 1750 (2007).

48. Nag, J. *et al.* Non-congruence of thermally driven structural and electronic transitions in VO_2. *J. Appl. Phys.* **112,** 103532 (2012).

49. Kimber, S. A. J. *et al.* Metal-insulator transition and orbital order in $PbRuO_3$. *Phys. Rev. Lett.* **102,** 046409 (2009).

50. Kim, B. J. *et al.* Novel $J_{\text{eff}} = 1/2$ Mott state induced by relativistic spin-orbit coupling in Sr_2IrO_4. *Phys. Rev. Lett.* **101,** 076402 (2008).

51. Kim, Y. K. *et al.* Fermi arcs in a doped pseudospin-1/2 Heisenberg antiferromagnet. *Science* **345,** 187–190 (2014).

52. Kim, Y. K., Sung, N. H., Denlinger, J. D. & Kim, B. J. Observation of a d-wave gap in electron-doped Sr_2IrO_4. *Nat. Phys.* **12** (2015).

53. de la Torre, A. *et al.* Collapse of the Mott Gap and Emergence of a Nodal Liquid in Lightly Doped Sr_2IrO_4. *Phys. Rev. Lett.* **115,** 176402 (2015).

54. Brouet, V. *et al.* Transfer of spectral weight across the gap of Sr_2IrO_4 induced by La doping. *Phys. Rev. B* **92,** 081117(R) (2015).

55. Arita, R. *et al.* Ab initio Studies on the Interplay between Spin-Orbit Interaction and Coulomb Correlation in Sr_2IrO_4 and Ba_2IrO_4. *Phys. Rev. Lett.* **108,** 086403 (2012).

56. Hsieh, D. *et al.* Observation of a metal-to-insulator transition with both Mott-Hubbard and Slater characteristics in Sr_2IrO_4 from time-resolved photocarrier dynamics. *Phys. Rev. B* **86,** 035128 (2012).

57. Carter, J.-M. & Kee, H.-Y. Microscopic theory of magnetism in $Sr_3Ir_2O_7$. *Phys. Rev. B* **87,** 014433 (2013).

58. Lee, J. S. *et al.* Insulator-metal transition driven by change of doping and spin-orbit interaction in Sr2IrO4. *Phys. Rev. B* **85,** 035101 (2012).

59. Clancy, J. P. *et al.* Dilute magnetism and spin-orbital percolation effects in $Sr_2Ir_{1-x}Rh_xO_4$. *Phys. Rev. B* **89,** 054409 (2014).

60. Cao, Y. *et al.* Hallmarks of the Mott-metal crossover in the hole-doped pseudospin-1/2 Mott insulator Sr_2IrO_4. *Nat. Comm.* **7,** 11367 (2016).

61. Moon, S. J. *et al.* Temperature dependence of the electronic structure of the $J_{\text{eff}} = 1$ Mott insulator Sr_2IrO_4 studied by optical spectroscopy. *Phys. Rev. B* **80,** 195110 (2009).

62. Kabanov, V. V., Demsar, J., Podobnik, B. & Mihailovic, D. Quasiparticle relaxation dynamics in superconductors with different gap structures: theory and experiments on $YBa_2Cu_3O_{7-\delta}$. *Phys. Rev. B* **59,** 1497–1506 (1999).

63. Rothwarf, A. & Taylor, B. N. Measurement of recombination lifetimes in superconductors. *Phys. Rev. Lett* **19,** 27–30 (1967).

64. Kim, B. J. *et al.* Phase-sensitive observation of a spin-orbital Mott state in Sr_2IrO_4. *Science* **323,** 1329–1332 (2009).

65. Crawford, M. K. *et al.* Structural and magnetic studies of Sr_2Ir_O. *Phys. Rev. B* **49,** 9198 (1994).

66. Huang, Q. *et al.* Neutron powder diffraction study of the crystal structures of Sr_2RuO_4 and Sr_2IrO_4 at room temperature and at 10 K. *J. Solid State Chem* **112,** 335 (1994).

67. Jackeli, G. & Khaliullin, G. Mott insulators in the strong spin-orbit coupling limit: from Heisenberg to a quantum compass and Kitaev models. *Phys. Rev. Lett.* **102,** 017205 (2009).

68. Perkins, N. B., Sizyuk, Y. & Wolfle, P. Interplay of many-body and single-particle interactions in iridates and rhodates. *Phys. Rev. B* **89,** 035143 (2014).

69. Jin, H., Jeong, H., Ozaki, T. & Yu, J. Anisotropic exchange interactions of spin-orbit-integrated states in Sr_2IrO_4. *Phys. Rev. B* **80,** 075112 (2009).

70. Zhang, H., Haule, K. & Vanderbilt, D. Effective J = 1/2 insulating state in Ruddlesden-Popper iridates: an LDA + DMFT study. *Phys. Rev. Lett.* **111,** 246402 (2013).

71. Ye, F. *et al.* Magnetic and crystal structures of Sr_2IrO_4 : A neutron diffraction study. *Phys. Rev. B* **87,** 140406 (2013).

72. Boseggia, S. *et al.* Locking of iridium magnetic moments to the correlated rotation of oxygen octahedra in Sr_2IrO_4 revealed by X-ray resonant scattering. *J. Phys. Condens. Matter* **25,** 422202 (2013).

73. Torchinsky, D. H. *et al.* Structural Distortion-Induced Magnetoelastic Locking in Sr_2IrO_4 Revealed through Nonlinear Optical Harmonic Generation. *Phys. Rev. Lett.* **114,** 096404 (2015).

74. Dhital, C. *et al.* Neutron scattering study of correlated phase behavior in Sr_2IrO_4. *Phys. Rev. B* **87,** 144405 (2013).

75. Chikara, S. *et al.* Giant magnetoelectric effect in the J_{eff} = 1/2 Mott insulator Sr_2IrO_4. *Phys. Rev. B* **80,** 140407 (2009).

76. Ganguly, S., Granas, O., Nordstrom & L. Non-trivial order parameter in Sr_2IrO_4. *Phys. Rev. B* **91,** 020404(R) (2015).

77. Lovesey, S. W., Khalyavin & D., D. Strange magnetic multipoles and neutron diffraction by an iridate perovskite Sr_2IrO_4. *J. Phys. Condens. Matter* **26,** 322201 (2014).

78. Varma, C. M. Non-Fermi-liquid states and and pairing instability of a general model of copper oxide metals. *Phys. Rev. B* **55,** 14554–14580 (1997).

79. Yakovenko, V. M. Tilted loop currents in cuprate superconductors. *Physica B* **460,** 159–164 (2015).

80. Simon, M. E., Varma & M., C. Symmetry considerations for the detection of second-harmonic generation in cuprates in the pseudogap phase. *Phys. Rev. B* **67,** 054511 (2003).

81. Fischer, M. H., Kim & E.-A. Mean-field analysis of intra-unit-cell order in the Emery model of the CuO_2 plane. *Phys. Rev. B* **84,** 144502 (2011).

82. Scagnoli, V. *et al.* Observation of orbital currents in CuO. *Science* **332,** 696–698 (2011).

83. S., D. M. & Norman, M. R. Orbital currents, anapoles, and magnetic quadrupoles in CuO. *Phys. Rev. B* **85,** 235143 (2012).

84. Qi, T. F. *et al.* Spin-orbit tuned metal-insulator transitions in single-crystal $Sr_2Ir_{1-x}Rh_xO_4$ (0<x<1). *Phys. Rev. B* **86,** 125105 (2012).

85. Wang, F. & Senthil, T. Twisted Hubbard model for Sr_2IrO_4: Magnetism and possible high temperature superconductivity. *Phys. Rev. Lett.* **106,** 136402 (2011).

86. Watanabe, H., Shirakawa, T. & Yunoki, S. Monte Carlo study of an unconventional superconducting phase in iridium oxide $J_{\mathrm{eff}} = 1/2$ Mott insulators induced by carrier doping. *Phys. Rev. Lett.* **110,** 027002 (2013).

87. Meng, Z. Y., Kim, Y. B. & Kee, H.-Y. Odd-parity triplet superconducting phase in multiorbital materials with a strong spin-orbit coupling: Application to doped Sr_2IrO_4. *Phys. Rev. Lett.* **113,** 177003 (2014).

88. Orenstein, J. Optical nonreciprocity in magnetic structures related to high-Tc superconductors. *Phys. Rev. Lett.* **107,** 067002 (2011).

89. Park, H. J. *et al.* Phonon-assisted optical excitation in the narrow bandgap Mott insulator $Sr_3Ir_2O_7$. *Phys. Rev. B* **89,** 155115 (2014).

90. Okada, Y. *et al.* Imaging the evolution of metallic states in a correlated iridate. *Nat. Mater.* **12,** 707–713 (2013).

91. Wang, Q. *et al.* Dimensionality-controlled Mott transition and correlation effects in single-layer and bilayer perovskite iridates. *Phys. Rev. B* **87,** 245109 (2013).

92. Fujiyama, S. *et al.* Weak antiferromagnetism of $J_{\mathrm{eff}} = 1/2$ band in bilayer iridate $Sr_3Ir_2O_7$. *Phys. Rev. B* **86,** 174414 (2012).

93. King, P. D. C. *et al.* Spectroscopic indications of polaronic behavior of the strong spin-orbit insulator $Sr_3Ir_2O_7$. *Phys. Rev. B* **87,** 241106 (2013).

94. Kim, J. *et al.* Large spin wave energy gap in the bilayer iridate $Sr_3Ir_2O_7$: evidence for enhanced dipolar interactions near the Mott metal-insulator transition. *Phys. Rev. Lett.* **109,** 157402 (2012).

95. Moretti Sala, M. e. a. Evidence of quantum dimer excitations in $Sr_3Ir_2O_7$. *Phys. Rev. B* **92,** 024405 (2015).

96. Hogan, T. *et al.* First-order melting of a weak spin-orbit Mott insulator into a correlated metal. *Phys. Rev. Lett.* **114,** 257203 (2015).

97. Lee, P. A., Nagaosa, N. & Wen, X.-G. Doping a Mott insulator: physics of high-temperature superconductivity. *Rev. Mod. Phys.* **78,** 17–85 (2006).

98. de la Torre, A. *et al.* Coherent quasiparticles with a small Fermi surface in lightly doped $Sr_3Ir_2O_7$. *Phys. Rev. Lett.* **113,** 256402 (2014).

99. He, J. *et al.* Spectroscopic evidence for negative electronic compressibility in a quasi-three-dimensional spin-orbit correlated metal. *Nat. Mater* **14,** 577–582 (2015).

100. Li, L. *et al.* Tuning the Jeff =1/2 insulating state via electron doping and pressure in the double-layered iridate $Sr_3Ir_2O_7$. *Phys. Rev. B* **87,** 235127 (2013).

101. Wall, S. *et al.* Tracking the evolution of electronic and structural properties of VO_2 during the ultrafast photoinduced insulator-metal transition. *Phys. Rev. B* **87,** 115126 (2013).

102. Gretarsson, H. *et al.* Two-magnon Raman scattering and pseudospin lattice interactions in Sr_2IrO_4 and$Sr_3Ir_2O_7$. *Phys. Rev. Lett.* **116,** 136401 (2016).

103. Demsar, J., Biljakovic, K. & Mihailovic, D. Single particle and collective excitations in the one-dimensional charge density wave solid $K_{0.3}MoO_3$ probed in real time by femtosecond spectroscopy. *Phys. Rev. Lett.* **83,** 800–803 (1999).

104. Hinton, J. P. *et al.* New collective mode in $YBa_2Cu_3O_{6+x}$ observed by time-domain reflectometry. *Phys. Rev. B* **88,** 060508 (2013).

105. Hogan, T. *et al.* Disordered dimer state in electron-doped $Sr_3Ir_2O_7$. *Phys. Rev. B* **94,** 100401(R) (2016).

106. Novoselov, K. S. *et al.* Electric field effect in atomically thin carbon films. *Science* **306,** 666–669 (2004).

107. Novoselov, K. S. *et al.* Two-dimensional atomic crystals. *Proc. Natl Acad. Sci. USA* **102,** 10451–10453 (2005).

108. Cao, T. *et al.* Valley-selective circular dichroism of monolayer molybdenum disulphide. *Nat. Comm.* **3,** 887 (2012).

109. Mak, K. F. *et al.* Control of valley polarization in monolayer MoS_2 by optical helicity. *Nat. Nanotech.* **7,** 494–498 (2012).

110. Lu, J. M. *et al.* Evidence for two-dimensional Ising superconductivity in gated MoS_2. *Science* **350,** 1353–1357 (2015).

111. Xi, X. *et al.* Ising pairing in superconducting $NbSe_2$ atomic layers. *Nat. Phys.* **12,** 139–143 (2016).

112. Xi, X. *et al.* Strongly enhanced charge-density-wave order in monolayer $NbSe_2$. *Nat. Nanotech.* **10,** 765–769 (2015).

113. Mermin, N. D. & Wagner, H. Absence of ferromagnetism or antiferromagnetism in one- or two- dimensional isotropic Heisenberg models. *Phys. Rev. Lett.* **17,** 1133–1136 (1966).

114. Huang, B. *et al.* Layer-dependent ferromagnetism in a van der Waals crystal down to the monolayer limit, https://arxiv.org/abs/1703.05892.

115. Gong, C. *et al.* Discovery of intrinsic ferromagnetism in 2D van der Waals crystals, https://arxiv.org/abs/1703.05753.

116. Lee, J.-U. *et al.* Ising-type magnetic ordering in atomically thin $FePS_3$. *Nano Lett.* **16,** 7433–7438 (2016).

117. Balkanski, M. *et al.* Magnetic ordering induced Raman scatering in $FePS_3$ and $NiPS_3$ layered compounds. *Pure & Appl. Chem.* **59,** 1247–1252 (1987).

118. Kurosawa, K. *et al.* Neutron diffraction study on $MnPS_3$ and $FePS_3$. *J. Phys. Soc. Jpn.* **52,** 3919–3926 (1983).

119. Wildes, A. R. *et al.* Magnetic structure of the quasi-two-dimensional antiferromagnet $NiPS_3$. *Phys. Rev. B* **92,** 224408 (2015).

120. Joy, P. A. *et al.* Magnetism in the layered transition-metal thiophosphates MPS_3 (M = Mn, Fe, and Ni). *Phys. Rev. B* **46,** 5425 (1992).

121. Jeevanandam, P. *et al.* Magnetism in $MnPSe_3$: a layered 3d5 antiferromagnet with unusually large XY anisotropy. *J. Phys.: Condens. Matter* **11,** 3563–3570 (1999).

122. Rule, K. C. *et al.* Single-crystal and powder neutron diffraction experiments on $FePS_3$: Search for the magnetic structure. *Phys. Rev. B* **76,** 134402 (2007).

123. Li, X. *et al.* Coupling the valley degree of freedom to antiferromagnetic order. *Proc. Natl Acad. Sci. USA* **110,** 3738–3742 (2013).

124. Ressouche, E. *et al.* Magnetoelectric $MnPS_3$ as a candidate for ferrotoroidicity. *Phys. Rev. B* **82,** 100408(R) (2010).

125. Sivadas, N. *et al.* Magnetic ground state of semiconducting transition-metal trichalcogenide monolayers. *Phys. Rev. B* **91,** 235425 (2015).

126. Chittari, B. L. *et al.* Electronic and magnetic properties of single-layer MPX_3 metal phosphorous trichalcogenides. *Phys. Rev. B* **94,** 184428 (2016).

127. Muthukumar, V. N. *et al.* Microscopic model of nonreciprocal optical effects in Cr_2O_3. *Phys. Rev. Lett.* **75,** 2766 (1995).

128. Piryatinskaya, V. G. *et al.* Temperature behavior of the fundamental optical absorption band in quasi-two-dimensional crystalline $MnPS_3$. *Low Temperature Physics* **38,** 1097–1101 (2012).

129. Joy, P. A. *et al.* Optical-absorption spectra of the layered transition-metal thiophosphates MPS_3 (M=Mn, Fe, and Ni). *Phys. Rev. B* **46,** 5134 (1992).

130. Grasso, V. *et al.* Optical-absorption spectra of crystal-field transitions in $MnPS_3$ at low temperatures. *Phys. Rev. B* **44,** 11060 (1991).

131. Sakhnenko, V. P. *et al.* The magnetoelectric effect due to local noncentrosymmetry. *Journal of Physics Condensed Matter* **24,** 266002 (2012).

132. Tanabe, Y. Theory of the optical spectra with particular reference to the effects of spin-orbit interaction. *Prog. Theor. Phys. Suppl.* **14,** 17 (1963).

Index

F

figures, 7–10, 13–15, 17–19, 21–23, 25, 26, 28, 31, 33, 34, 36, 38, 39, 41–46, 50, 51, 53, 54, 57, 58, 60, 61